

Controlled Intermixing Superlattices of Thermoelectric Half-Heusler Materials

Dissertation
zur Erlangung des Grades
"Doktor der Naturwissenschaften"
am Fachbereich Physik, Mathematik und Informatik
der Johannes Gutenberg-Universität
in Mainz

Sven Heinz
geboren in Simmern (Hunsrück)

JOHANNES GUTENBERG
UNIVERSITÄT MAINZ



Mainz, August 2020

Erster Berichterstatter: Prof. Dr. Gerhard Jakob

Zweiter Berichterstatter: (Aus Datenschutzgründen entfernt)

Datum der Prüfung: 25.11.20

Eidesstattliche Erklärung

Hiermit erkläre ich an Eides statt, dass ich meine Dissertation selbständig und ohne fremde Hilfe verfasst habe. Ich habe nur Quellen und Hilfsmittel verwendet, die von mir in der Bibliographie angegeben sind. Die Doktorarbeit ist weder abschnittsweise, noch in der vorliegenden Form bei einer anderen Prüfungsbehörde zur Erlangung eines Doktorgrades eingereicht worden.

I declare under penalty of perjury, that I wrote this dissertation independently, without assistance and use of sources other than those indicated my bibliography. The thesis, in whole or in part, has never been submitted to any other examination committee that is able to admit a doctoral degree.

Mainz, den

.....
Sven Heinz

Contents

Abbreviations	v
List of Figures	viii
List of Tables	ix
Zusammenfassung	xi
Abstract	xiii
1 Thermoelectric Energy Conversion	1
1.1 Thermoelectric effects	1
1.2 Thermoelectric Generators	3
1.2.1 Thermoelectric Conversion Efficiency	4
1.2.2 Conversion Efficiency Optimization	7
1.3 Half-Heusler Materials	8
1.3.1 Self-Doping Effects	10
1.3.2 Spontaneous Phase Separation	12
2 Thermal Transport	13
2.1 Phonon Dispersion Relation	13
2.2 Lattice Thermal Conductivity	16
2.3 Phonon Scattering Mechanisms	17
2.4 Interface Scattering in Multilayer Systems	20
2.4.1 Diffusive Mismatch Model	24
2.4.2 Acoustic Mismatch Model	26
2.4.3 Thermal Boundary Resistance of Non-Ideal Interfaces	27
3 Electronic Transport	29
3.1 The Drude Model	29
3.1.1 Electronic Transport in a Magnetic Field	30
3.1.2 The Wiedemann-Frantz-Law	32
3.1.3 The Limits of the Drude-model	33
3.2 Hopping Conduction	34
4 Experimental Techniques	37
4.1 Magnetron Sputter Deposition	37
4.2 Thermal Conductivity Measurements of Thin Films	41
4.3 Energy Dispersive X-ray Spectroscopy	46

Contents

4.4	X-Ray Diffraction	48
5	P-type thin film $\text{Hf}_{0.5}\text{Zr}_{0.5}\text{CoSb}_{1-x}\text{Sn}_x$	51
5.1	Introduction	51
5.2	Sample Preparation	52
5.2.1	Optimization of Growth Conditions	53
5.2.2	Composition Variation	54
5.3	Electronic Characterization	58
5.3.1	Experimental Setup	59
5.3.2	Results and Discussion	63
5.3.3	Models of Electronic Transport	66
5.4	Conclusion	75
6	Controlled Intermixing Superlattices	77
6.1	Introduction	77
6.2	Theoretical Model of Thermal Conductivity in TiNiSn Superlattices	78
6.2.1	Separating Layer and Interface Contribution	78
6.2.2	Estimating the Finite Size Term and Thermal Boundary Resistance for TiNiSn and HfNiSn Superlattices	80
6.3	Sample Preparation	86
6.3.1	Target Fabrication	86
6.3.2	Thin films	87
6.4	Structural Characterization	88
6.4.1	Crystalline Quality by X-ray diffraction	88
6.4.2	Transmission Electron Microscopy	91
6.4.3	Surface Morphology	92
6.4.4	AlO_x -layer Optimization	98
6.5	Experimental Results	100
6.5.1	The 3ω -Signal of Superlattices	100
6.5.2	Thermal Resistivity Measurements	101
6.6	Summary	104
	Conclusion	107
	List of (co-)authored Publications	123

Abbreviations

<i>AFM</i>	Atomic force microscopy
<i>AMM</i>	Acoustic mismatch model
<i>CADEM</i>	Calculate X-ray diffraction of epitaxial multilayers
<i>DFT</i>	Density functional theory
<i>DMM</i>	Diffusive mismatch model
<i>EDX</i>	Energy-dispersive X-ray spectroscopy
<i>NNH</i>	Next nearest neighbor hopping
<i>PVD</i>	Physical vapor deposition
<i>PXD</i>	Powder X-ray diffraction
<i>SEM</i>	Scanning electron microscopy
<i>SPS</i>	Spark plasma sintering
<i>TBR</i>	Thermal boundary resistance
<i>TEM</i>	Tunneling electron microscopy
<i>VRH</i>	Variable range hopping
<i>XRD</i>	X-ray diffraction

List of Figures

1.1	Model circuit of a thermocouple.	2
1.2	Typical design for a TE-element.	4
1.3	Conversion efficiencies of thermoelectric devices and conventional processes.	4
1.4	ZT and related physical quantities in dependence of the charge carrier density.	6
1.5	Selection of temperature dependent ZT-curves of current materials.	6
1.6	Typical density of states of a high efficiency thermoelectric material.	8
1.7	Basic composition of half-Heusler materials.	9
1.8	Summary of doping trends in half-Heusler semiconducting compounds.	11
1.9	Spontaneous phase separation in $\text{Ti}_x(\text{Zr}_{0.5}\text{Hf}_{0.5})_{1-x}\text{NiSn}$	12
2.1	Illustration of a longitudinal elastic wave.	14
2.2	Exemplary phonon dispersion relation.	15
2.3	Phonon spectra of (Hf, Zr, Ti)NiSn	17
2.4	Thermal conductivity in dependence of different scattering mechanisms.	18
2.5	Mean free path limitation in nanowires of different diameters.	19
2.6	Illustration of the effect of phonon interference.	20
2.7	Interplay between boundary roughness and phonon wavelength.	21
2.8	Thermal transport regimes in superlattices.	23
2.9	Phonon density of states of HfNiSn and TiNiSn and their overlap.	25
2.10	Illustration of scattering in the acoustic mismatch model.	26
2.11	Simulated transmissivity coefficient in dependence of specularity.	27
3.1	Illustration of the Hall effect in a conducting solid.	31
3.2	Common distribution functions used in the description of electronic transport.	33
3.3	Exemplary energy diagram dominated by potential wells.	34
4.1	Schematic drawing of a DC sputter chamber.	37
4.2	Impact of working gas ions on a sputter target surface.	38
4.3	Three zone model of magnetron sputter deposition.	39
4.4	The sputter rate depending on deposition parameters.	40
4.5	Sketch of a typical 3ω -measurement structure.	41
4.6	Exemplary heating current, temperature response and 3ω -voltage signal.	42
4.7	Heat dissipating from a narrow heater into a homogenous medium.	43
4.8	Heat spread in an homogeneous sample and with an additional thin film.	45
4.9	Basic process underlying energy dispersive X-ray spectroscopy (EDX).	46
4.10	Illustration of electron energy absorption and resulting X-ray spectrum.	47
4.11	Illustration of the Bragg-Brentano X-ray diffraction geometry.	49

List of Figures

5.1 Exemplary depiction of phase separation	51
5.2 Target composition in dependence on the target depth.	52
5.3 Crystalline qualities of $(\text{Zr}_{0.5}\text{Hf}_{0.5})\text{Co}(\text{Sb}_{1-x}\text{Sn}_x)$ thin film samples.	53
5.4 Excess Sb target composition and geometry.	54
5.5 Compositional maps of thin films and bulk samples	56
5.6 X-ray diffraction data of thin films samples from the Sb-excess target.	57
5.7 Topographic AFM scan of samples with different XRD-properties.	58
5.8 Measurement structures for Hall-effect measurements.	59
5.9 Effect of sample space geometry on temperature measurement.	60
5.10 Temperature dependent resistivity of thin films and bulk samples.	63
5.11 Hall voltage raw data for thin film and bulk samples.	65
5.12 Temperature dependent Hall constant data of thin films and bulk samples.	66
5.13 Resistivity and Hall constant assuming dominant thermal excitation.	68
5.14 Resistivity and Hall constant in the localization model.	72
6.1 Illustration of superlattice design with varying degrees of intermixing.	78
6.2 Mean transition function of a TiNiSn/HfNiSn interface.	82
6.3 Finite size term in dependence of period length.	83
6.4 Contributions to effective interface resistance.	85
6.5 Composition homogeneity of the sputter targets.	86
6.6 Basic sample design	87
6.7 Characterization of superlattice samples by X-ray diffraction.	89
6.8 TEM measurements of pristine and artificial intermixing superlattices.	90
6.9 Electrical field in an insulating barrier with spike-like features.	91
6.10 Surface topography as a function of growth temperature.	92
6.11 Exemplary SEM-image of a sample surface.	93
6.12 Compositional analysis of an exemplary sample surface.	94
6.13 Position in the TiNiSn phase diagram of the investigated samples.	95
6.14 Typical Ni_3Sn_4 growth characteristics.	95
6.15 SEM image and composition maps of a wedge-cut sample.	96
6.16 Position of the thin film samples in the TiNiSn phase diagram.	97
6.17 SEM image and compositional maps of a faulty AlO_x -barrier.	98
6.18 Raw signals associated with the 3ω -technique for two exemplary samples.	100
6.19 Thermal resistivities in dependence of the period length.	101
6.20 Thermal resistivity data and fit.	103
6.21 Effective interface thermal resistivity depending on specularity.	104
6.22 Phonon bridge effect in superlattices.	105

List of Tables

1.1	Common technologically used thermocouple material combinations.	3
3.1	Values for the Lorenz-number of common metals.	32
4.1	Approximations relevant for the differential 3ω -method and related errors.	44
5.1	Composition of manufactured samples and targets.	55
5.2	Overview over estimated error related to temperature drift.	61
5.3	Resistivity and Hall constant assuming dominant hole localization.	69
5.4	Parameters used in the model of thermally excited electronic holes.	74
6.1	Literature values used to calculate the interface thermal resistance.	81
6.2	Material equivalents for different interface designs.	103

Zusammenfassung

Die vorliegende Untersuchung beschäftigt sich mit der Weiterentwicklung dünn-schicht-basierter thermoelektrischer Generatoren auf Grundlage von halb-Heusler Materialien. Für diesen Zweck werden zwei unterschiedliche Wege verfolgt: Einerseits die Überführung hocheffizienter (Hf,Zr)Co(Sb,Sn) Volumenmaterialien in Dünnschichten als p-Typ Analogon zu etablierten n-Typ (Hf,Ti)NiSn und andererseits die thermische Optimierung bestehender Dünnschichtsysteme im Rahmen des Übergitter-Ansatzes.

Ein p-Typ Analogon ist eine Voraussetzung für den Übergang von einem ein- zu einem vorteilhaften zweikomponentigen Generatorkonzept. In dieser Studie wird die Wachstumsdynamik des p-Typ Materials untersucht und es wird mit den entsprechenden Volumenmaterialien verglichen. Für bestimmte Sputterbedingungen zeigen die resultierenden Dünnschichten negative statt positive Seebeckkoeffizienten, was auf eine Ausfällung des als Akzeptor wirkenden Zinns in nanometergroße Ausscheidungen zurückgeführt wird. Allerdings können durch eine Erhöhung der Sputterleistung reproduzierbar lochleitende Dünnschichten hergestellt werden. Für alle Proben zeigt sich eine Überlagerung von Loch- und Elektronenleitung, die ebenfalls im Volumenmaterial, in abgeschwächter Form, vorgefunden wird. Dieses Verhalten manifestiert sich in einem charakteristischen Vorzeichenwechsel im Hall-Koeffizienten bei tiefen Temperaturen. Zur Erklärung dieses Verhaltens und der elektronischen Eigenschaften werden ausgehend von theoretischen Vorhersagen mehrere Modelle diskutiert. In der Schlussfolgerung werden Hopping-Mechanismen in einem Akzeptorband als wichtiger Bestandteil der Ladungsträgercharakteristik in (Hf,Zr)Co(Sb,Sn) identifiziert, insbesondere in Dünnschichten.

In der Untersuchung von Übergittern wird die Dominanz von Grenzschichtphänomenen in den thermischen Eigenschaften bei geringen Periodenlängen bestätigt. Darüber hinaus wird ein enger Zusammenhang zwischen Grenzschichtqualität und Wärmewiderstand belegt. Durch die gezielte Präparation von Übergittern mit unterschiedlicher Vermischungsschichtdicke, wird ein Unterschied von bis zu 50% im Grenzschichtbezogenen Wärmewiderstand erzielt. Zur Interpretation der Ergebnisse wird ein analytisches Modell herangezogen, das an das TiNiSn/ HfNiSn-System angepasst wird. Es sagt eine fast 95% Übergangswahrscheinlichkeit von wärmetransportierenden Phononen an perfekten Grenzschichten voraus. Dieser Wert liegt deutlich höher als der von anderen Modellsystemen wie Si/Ge und AlAs/GaAs, was auf den relativ niedrigen akustischen Kontrast zwischen TiNiSn und HfNiSn zurückgeht. Andererseits sagt das Modell mit der Aufweitung des Grenzschichtbereichs eine starke Verminderung der Übergangswahrscheinlichkeit auf ~25% voraus, was mit einem stark erhöhten Wärmewiderstand einhergeht. Allerdings bestätigen die experimentellen Daten diese Vorhersage nur zum Teil. Während der Grenzflächenwiderstand durch eine Verbreiterung der Durchmis-

List of Tables

chungsschicht zunächst steigt, sinkt er letztendlich unter sein Ausgangsniveau ab. In der Folge ergibt sich, dass eine moderate Grenzschichtdurchmischung den Wärmewiderstand maximiert. Unter Berücksichtigung von weitergreifenden theoretischen Modellen wird dieses Verhalten mit dem Einfluss der Grenzschicht als akustische Pufferschicht erklärt. Durch die vermittelnden akustischen Eigenschaften der Mischschicht wird ein Grenzschichtübergang wärmetransportierender Phononen begünstigt. Die Ergebnisse liefern Hinweise für die thermische Optimierung thermoelektrischer Dünnschichten im Speziellen und Strukturen im Größenbereich weniger Nanometer im Allgemeinen.

Abstract

This study investigates the further development of thermoelectric generators on the basis of half-Heusler materials. For this purpose two different routes are pursued: On the one hand the transfer of high-efficiency bulk (Hf,Zr)Co(Sb,Sn) materials to thin films as a p-type analogue to established n-type (Hf,Ti)NiSn and on the other hand the thermal optimization of established thin film systems in the framework of the superlattice-approach.

A p-type analogue is a prerequisite for the transition from a one-legged to a advantageous two-legged generator design. In this study different growth-regimes of the p-type material are investigated and compared with corresponding bulk-materials. For certain sputter-conditions, they exhibit a negative instead of a positive Seebeck-coefficient, which is explained with the precipitation of acceptor-like Sn in nanometer-sized inclusions. However, by increasing the sputter power, hole-conducting thin films can be deposited reproducibly. All samples exhibit a bipolar behavior, that is also present in bulk, albeit to a lesser degree. This bipolar behavior manifests itself in a characteristic sign change of the Hall-coefficient at low temperatures. To explain this behavior, the electronic properties are discussed in the framework of different models. As a conclusion, hopping mechanisms in an acceptor-band are identified as a crucial part of the charge carrier dynamics in (Hf,Zr)Co(Sb,Sn), especially in thin films.

In the investigation of superlattices, the dominance of interface-phenomena in the thermal properties for short period lengths are confirmed. Additionally, a close relationship between the interface quality and the thermal resistance is recorded. Through the controlled preparation of superlattices with different intermixing layers, a difference of 50% in the interface-related thermal resistance is achieved. To interpret the experimental results an analytical model is adapted to the HfNiSn/TiNiSn-system. It predicts a 95% transition probability of heat-carrying phonons for perfect interfaces. This value is significantly larger compared to other model systems like Si/Ge and AlAs/GaAs, which is caused by the relatively low acoustic contrast between TiNiSn and HfNiSn. At the same time the model predicts a strong decrease of transition probability down to ~25% with the broadening of the boundary layer, which is accompanied by a significant uptake in thermal resistance. However, the experimental data confirms the predictions only partly. While the thermal resistance initially increases with a broadening of the intermixing layer, it ultimately decreases again below its initial value. As a consequence, an intermediate degree of interface intermixing maximizes thermal resistance. By reviewing a more extensive model, this behavior is explained with the function of the intermixing layer as an acoustic buffer. Because of the mediating acoustic properties of the mixed layer, the transition of heat-carrying phonons is promoted. The results are relevant for the thermal optimization of thermoelectric thin film systems specifically and nanoscale structures in general.

1 Thermoelectric Energy Conversion

Supplying a growing population with affordable, reliable electrical energy without furthering global warming is one of the central challenges of the 21st century. The CO₂-emissions of the current, fossil-fuel based energy sector have been identified as a major contributing factor to the increase of the global mean temperature of $\sim 1^\circ\text{C}$ during the last 170 years [1]. Nevertheless, the transition to renewable primary energy sources is limited by the available technology and subsequently the pace of technology development. In the mean time, a significant reservoir of energy is unused: Waste heat

During the conversion of fossil fuels to electrical power, around 60% of energy is lost in unwanted heating of the environment [2]. Low scale, reliable energy converters can potentially harvest part of this energy and therefore improve the efficiency of the overall process. Thermoelectric generators are the perfect candidate for this application: Specialized materials convert a thermal gradient directly into an electrical current. However, their development relies on the balancing of partly conflicting requirements and therefore demands the understanding of the underlying physical effects. The next chapter illuminates the phenomena that thermoelectric energy conversion is based on and presents common optimization routes.

1.1 Thermoelectric effects

Thermoelectric phenomena represent a category of effects, which rely on the link of electronic and thermal transport. In most cases, a thermal current is driven by a temperature gradient, while an electrical current is generated by a gradient in the electrical potential. However, both phenomena are interlinked: A temperature gradient leads to an additional electrical current and an electronic potential gradient to a heat flux. Using the Boltzmann transport equation in the relaxation time approximation, this relationship can be derived and expressed in the following set of equations [3]:

$$\vec{j} = L^{11}\vec{E} + L^{12}(-\nabla T) \quad (1.1)$$

$$\vec{j}_q = L^{21}\vec{E} + L^{22}(-\nabla T) \quad (1.2)$$

With the electrical field \vec{E} , the temperature gradient ∇T , the electrical current density \vec{j} , the heat current density \vec{j}_q and the tensor L^{mn} .

These equations can easily be applied to the model circuit drawn in Figure 1.1. Two different conductors 1 and 2 are joined at two points to form an incomplete loop. Because the circuit is open at position 0, the net charge current is zero, so equation 1.1 yields:

1 Thermoelectric Energy Conversion

$$E_s = (L^{11})^{-1} L^{12} \frac{\partial T}{\partial s} = S_{1,2} \frac{\partial T}{\partial s} \quad (1.3)$$

With the electric field E_s and temperature gradient $\frac{\partial T}{\partial s}$, both along the wire, and the abbreviation $S_{1,2}$ as the material specific Seebeck coefficient. From this equation we get the voltage drop across the loop for a finite temperature gradient:

$$U = \int_0^A E_s ds + \int_A^B E_s ds + \int_B^0 E_s ds \quad (1.4)$$

$$= \int_B^A S_2 \frac{\partial T}{\partial s} ds + \int_A^B S_1 \frac{\partial T}{\partial s} ds \quad (1.5)$$

$$= \int_A^B (S_2 - S_1) dT = S_{21} (T_B - T_A) \quad (1.6)$$

A temperature difference between two material junctions leads to a proportional voltage U the magnitude of which depends on the differential Seebeck coefficient $S_{21} = S_2 - S_1$. Similarly, the reverse effect can be derived for the same circuit at a constant temperature with an external applied voltage. Equations 1.1 and 1.2 then become:

$$\vec{j} = L^{11} \vec{E} \quad (1.7)$$

$$\vec{j}_q = L^{21} \vec{E} \quad (1.8)$$

from which the relation

$$j_q = L^{21} (L^{11})^{-1} j = \pi_\alpha j \quad (1.9)$$

follows, with the material specific Peltier coefficient π_1 or π_2 . This means that with an external applied current j , heat proportional to $(\pi_1 - \pi_2)j$ is absorbed at junction A and the equal amount emitted at junction B.

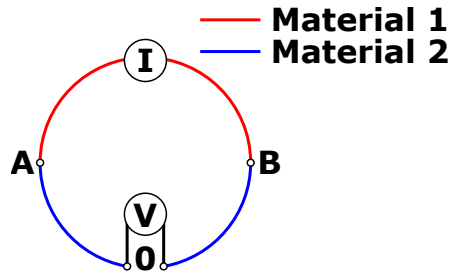


Figure 1.1: Model circuit of a thermocouple. The circuit is open at position 0 and the points A and B mark the material junctions

1.2 Thermoelectric Generators

The most widespread technological application of thermoelectric effects comes in the form of metal and metal alloys being joined in thermocouples for small scale temperature probes. For different temperature ranges, standard material combinations have been established, an excerpt of which are shown in table 1.1. They exhibit a relatively constant Seebeck coefficient in their respective temperature windows, making their output voltage proportional to the difference between their junction temperatures. However, attainable voltage differences are in the range of tens of $\mu\text{V/K}$. Specialized semiconductor materials have Seebeck coefficients which can be up to one order of magnitude larger, enabling their rational use in energy conversion. In a typical device design, shown in figure 1.2, many thermocouple structures are connected in series, with specialized materials for both legs. Typically one of the legs is an n-type semiconductor, while the other one is p-type, to ensure a high differential Seebeck-coefficient. They can serve to directly convert an electrical current into a heat current and vice versa, without the need for moving parts, making them maintenance economical.

Nevertheless, in most cases heat engines are used for heat conversion, introducing mechanical energy as an intermediate between heat and electrical currents. This is because the wide availability of cheap primary energy favored the use of well established techniques. During the last century, with increasing resource scarcity and an increasing awareness of environmental deterioration the research efforts into this technological problem were intensified. However, optimizing thermoelectric conversion efficiency proved to be an elusive goal, because of the intertwined nature of the underlying physical properties.

Type	Thermo-elements	Base composition (mass-%)	Temperature window ($^{\circ}\text{C}$)	Seebeck coefficient ($\mu\text{V/K}$)
J	JP JN	Fe 44Ni-55Cu	0-800	56.8 \pm 5.1
K	KP KN	90Ni-9Cr 94Ni-6(Al, Mn, Fe, Si, Co)	0-1200	40.1 \pm 2.1
N	NP NN	84Ni-14Cr-1.4Si 95Ni-4.4Si-0.15Mg	200-1200	32.6 \pm 2.9
E	EP EN	90Ni-9Cr 44Ni-55Cu	400-800	79.8 \pm 1.3

Table 1.1: Example of different technologically used thermocouple material combinations. The last two columns give the mean Seebeck coefficient and its standard deviation over the corresponding temperature window, respectively. [4]

1 Thermoelectric Energy Conversion

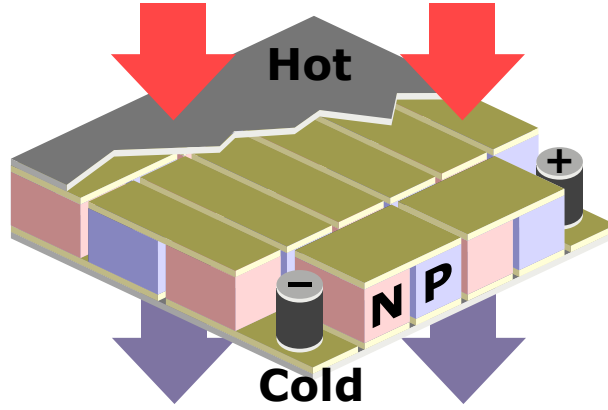


Figure 1.2: Typical design for a TE-element. The n-type leg is colored in red, while the p-type has a blue color.

The following section elucidates the connection between thermoelectric conversion efficiency and basic material properties, focusing on the most common ways of optimization.

1.2.1 Thermoelectric Conversion Efficiency

Three material properties primarily determine the suitability of a material for thermoelectric energy conversion: The Seebeck coefficient S , the electrical conductivity σ and the thermal conductivity κ [6]. The Seebeck coefficient quantifies the voltage that is generated by a given temperature difference and thus directly limits the power that can be supplied by a TE-element. However, from equation 1.6 it becomes apparent that the output voltage is also limited by a materials ability to attain a high temperature gradient ∇T from a given heat flux q . The thermal conductivity expresses this quality, as it acts as the

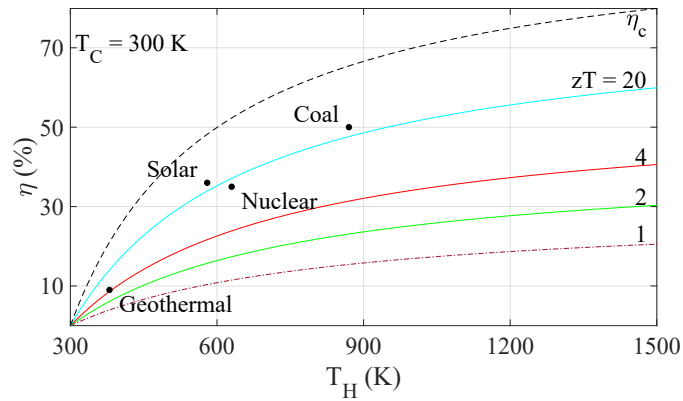


Figure 1.3: Comparison between conversion efficiencies of thermoelectric devices with given ZT and conventional processes. Adapted from [5].

proportionality constant between the heat gradient and a heat current [7]:

$$\nabla T = -\frac{1}{\kappa} \vec{q} \quad (1.10)$$

An effective thermoelectric material has a low thermal conductivity, therefore giving rise to high thermal gradients.

Lastly, a thermoelectric material has to be able to conduct an electric current reasonably well. Therefore the electrical conductivity has to be high, as ohmic losses otherwise dissipate energy and thus limit the conversion efficiency.

These three quantities, S , σ and κ can be expressed in the thermoelectric figure of merit, which acts as a useful proxy for the application utility of a material [8]:

$$ZT = \frac{S^2 \sigma}{\kappa} T \quad (1.11)$$

With the mean temperature T .

The figure of merit weighs the different quantities against each other, creating a way to concisely express the thermoelectric conversion efficiency [9]:

$$\eta = \frac{T_H - T_C}{T_H} \frac{\sqrt{1 + ZT} - 1}{\sqrt{1 + ZT} + T_C/T_H} \quad (1.12)$$

Here, T_C and T_H express the hot end and cold end temperature of a TE generator.

Thermoelectric devices are compared with conventional energy conversion processes in Figure 1.3, to put the attainable efficiencies into context and illustrate the current state of the art. While conventional conversion methods correspond to hypothetical thermoelectric materials with $ZT = 20$, maximum ZT s of currently researched materials vary between 2 and 3 [10]. The most advanced operational modules still exhibit a figure of merit of less than one, with a conversion efficiency of around 8% [10].

These state of the art materials are the results of a long history of thermoelectric research, beginning in the 50s of the past century. While initial research was promising, overcoming the threshold of a ZT of 1 proved to be difficult, and could only be achieved after a resurgence of the research topic at the end of the 20s century.

The Link Between Electrical Conductivity and Seebeck Coefficient

When a system exhibits a thermal gradient, high energy charge carriers are over-represented at the hot end relative to the cold end. They diffuse consequently from hot to cold with a flow of low energy electrons in the opposite direction. For a flat density of states these currents cancel out. Consequently, there is no charge build-up and thus no voltage gradient, which means the Seebeck coefficient is zero. A high Seebeck-coefficient material, on the other hand, exhibits a high differential conductivity close to the Fermi-level: States above it conduct electricity better than the ones below, or vice

1 Thermoelectric Energy Conversion

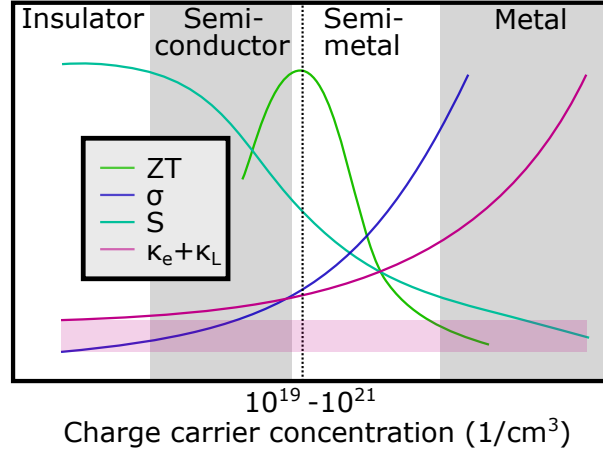


Figure 1.4: ZT and underlying physical quantities in dependence of the charge carrier density. The optimum charge carrier density varies between 10^{19} and 10^{21} $1/\text{cm}^3$, depending on the material system [11].

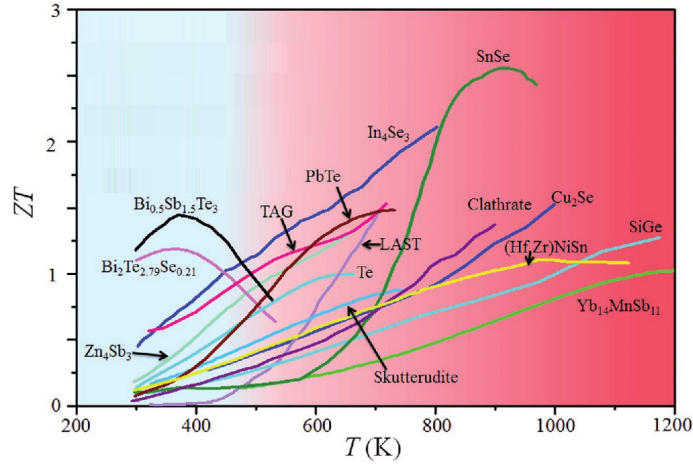


Figure 1.5: Selection of temperature dependent ZT-curves of current materials. Adapted from [10]

versa. Thus a net current and a consequent charge build up emerges. For a degenerate semiconductor in a single-band approximation, this relationship can be expressed in the Mott-formula[12]:

$$S = \frac{\pi^2 k_B}{3e} k_B T \left[\frac{1}{D(E)} \frac{dD(E)}{dE} + \frac{1}{\mu(E)} \frac{d\mu(E)}{dE} \right]_{E=E_F} \quad (1.13)$$

With the Boltzmann constant k_B , the electron charge e , the density of states $D(E)$ and the charge carrier mobility μ .

A high Seebeck coefficient is therefore caused by either a change in charge carrier density or mobility close to the Fermi-level. For a semiconductor, where the bands can be approximated as parabolas, the density of states flattens for higher energy states and thus with higher occupation. This leads to an overall inverse dependency of the Seebeck coefficient on the occupation, i.e. the charge carrier density n [11]:

$$S = \frac{8\pi^2 k_B^2}{3eh^2} m^* T \left(\frac{\pi}{3n} \right)^{2/3} \quad (1.14)$$

With the charge carrier concentration n , the Boltzmann constant k_B , the electron charge e , the Planck-constant h , the effective mass m^* and the temperature T . While this equation is only true for metals or highly doped semiconductors with an energy-independent scattering approximation, it expresses a more general trend: The Seebeck coefficient is inversely proportional to the charge carrier density. Thus, insulators tend to show the highest Seebeck coefficient. However, these materials are unsuitable for the use in an electronic device, as the electrical conductivity relies on a high charge carrier density [13]:

$$\sigma = ne\mu \quad (1.15)$$

with the charge carrier mobility μ . Consequently, there is an ideal charge carrier concentration that optimizes σS^2 , which typically lies between 10^{19} and 10^{21} $1/\text{cm}^3$ [11]. The overall dependence of ZT on n , as depicted in Figure 1.4, is similar in most materials, although the position of the ZT maximum varies.

1.2.2 Conversion Efficiency Optimization

Additionally the ZT -Maximum is strongly temperature dependent, limiting the rational use of materials to characteristic temperature ranges. Figure 1.5 shows a depiction of the ZT temperature dependence of current materials of interest, with the temperature spread clearly visible. Many current commercially used materials are Bi and Te based, with peak efficiencies around room temperature [14]. Consequently they are predominantly employed in cooling applications, where their small size, reliability, and controllability are crucial. On the high-temperature end, SiGe has been successfully employed in space exploration [15], with the accessibility of high heat fluxes in radioisotope generators. However, most current research is focused on the intermediate temperature region, where most of current technical applications are situated. Here, a host of materials has been considered following a better understanding of the microscopic processes and nanostructuring techniques.

This research mostly goes either in the direction of electronic property optimization or the decrease of thermal conductivity. A typical band structure of a high efficiency thermoelectric material is illustrated in Figure 1.6, where a sharp maximum of the density of states $\delta(E)$ is located close to the Fermi energy. The large $\frac{\partial \delta}{\partial E}$ leads to a high Seebeck coefficient [12], thus increasing thermoelectric conversion efficiency. This band structure

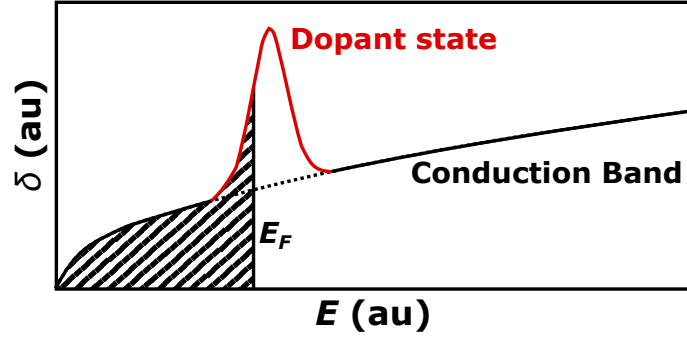


Figure 1.6: Typical density of states of a high efficiency thermoelectric material. A dopant state is depicted in red and the host band is outlined in black. Adapted from [16]

is commonly found when a band overlaps with another band or dopant states, which are close to the Fermi-energy. The overlapping band or dopant states supply a sharp local maximum in $\delta(E)$, while the host band provides a base charge carrier density and thus a reasonable electrical conductivity. The resulting material maximizes the numerator of equation 1.11, $S^2\sigma$.

However, an increased electrical conductivity invariably leads to a simultaneous increase in thermal conductivity, partly compensating efficiency increases. The reason is that charge carriers also carry heat. Thus an electronic contribution to the thermal conductivity is proportional to the electrical conductivity. This property is expressed in the Wiedemann-Frantz-Law [13]:

$$L = \frac{\kappa_e}{\sigma T} = \text{const.} \quad (1.16)$$

with the Lorenz-constant L and κ_e as the portion of heat carried by charge carriers.

For metals and highly doped semiconductors, heat transport is dominated by the charge carriers and thus the electrical and thermal conductivities are strongly linked. However, depending on the material, a significant portion of heat is carried by lattice vibrations. This contribution is commonly referred to as the lattice part of thermal conductivity and it has the advantage of being widely independent of both S and σ . Thus, several optimization approaches focus on this part, mainly by different routes of nanostructuring [8].

1.3 Half-Heusler Materials

Semiconducting or semimetallic Half-Heusler compounds constitute a promising candidate for thermoelectric energy conversion, because of their high Seebeck coefficient and reasonable electrical conductivity [17]. These properties lead to a ZT of around 1 for (Ti,Zr,Hf)NiSn at temperatures between 700-1200 K [18]. Additionally, they potentially

Half-Heusler																		XYZ					
1 H Hydrogen 1.00794																			2 He Helium 4.003				
3 Li Lithium 6.941	4 Be Beryllium 9.012182																	5 B Boron 10.811	6 C Carbon 12.0107	7 N Nitrogen 14.00674	8 O Oxygen 15.9994	9 F Fluorine 18.9984032	10 Ne Neon 20.1797
11 Na Sodium 22.989770	12 Mg Magnesium 24.3050																	13 Al Aluminum 26.981538	14 Si Silicon 28.0855	15 P Phosphorus 30.973761	16 S Sulfur 32.066	17 Cl Chlorine 35.4527	18 Ar Argon 39.948
19 K Potassium 39.0983	20 Ca Calcium 40.078	21 Sc Scandium 44.955910	22 Ti Titanium 47.867	23 V Vanadium 50.9415	24 Cr Chromium 51.9961	25 Mn Manganese 54.938049	26 Fe Iron 55.845	27 Co Cobalt 58.933200	28 Ni Nickel 58.6934	29 Cu Copper 63.546	30 Zn Zinc 65.39	31 Ga Gallium 69.723	32 Ge Germanium 72.61	33 As Arsenic 74.92160	34 Se Selenium 78.96	35 Br Bromine 79.904	36 Kr Krypton 83.80						
37 Rb Rubidium 85.4678	38 Sr Strontium 87.62	39 Y Yttrium 88.90585	40 Zr Zirconium 91.224	41 Nb Niobium 92.90638	42 Mo Molybdenum 95.94	43 Tc Technetium (98)	44 Ru Ruthenium 101.07	45 Rh Rhodium 102.90550	46 Pd Palladium 106.42	47 Ag Silver 107.8682	48 Cd Cadmium 112.411	49 In Indium 114.818	50 Sn Tin 118.710	51 Sb Antimony 121.760	52 Te Tellurium 127.60	53 I Iodine 126.90447	54 Xe Xenon 131.29						
55 Cs Cesium 132.90545	56 Ba Barium 137.327	57 La Lanthanum 138.9055	58 Ce Cerium 140.116	59 Pr Praseodymium 140.90765	60 Nd Neodymium 144.24	61 Pm Promethium (145)	62 Sm Samarium 150.36	63 Eu Europium 151.964	64 Gd Gadolinium 157.25	65 Tb Terbium 158.92534	66 Dy Dysprosium 162.50	67 Ho Holmium 164.93032	68 Er Erbium 167.26	69 Tm Thulium 168.93421	70 Yb Ytterbium 173.04	71 Lu Lutetium 174.967							
87 Fr Francium (223)	88 Ra Radium (226)	89 Ac Actinium (227)	90 Th Thorium 232.0381	91 Pa Protactinium 231.03588	92 U Uranium 238.0289	93 Np Neptunium (237)	94 Pu Plutonium (244)	95 Am Americium (243)	96 Cm Curium (247)	97 Bk Berkelium (247)	98 Cf Californium (251)	99 Es Einsteinium (252)	100 Fm Fermium (257)	101 Md Mendelevium (258)	102 No Nobelium (259)	103 Lr Lawrencium (262)							

Figure 1.7: Basic composition of half-Heusler materials with possible constituents on the characteristic lattice sites X , Y and Z .

enable the use of non-toxic, earth abundant materials in thermoelectrics and are compatible with large-scale production [9].

Half-Heusler materials are ternary compounds of metals with the general formula XYZ , where the X, Y, Z -atoms form fcc lattices, which are shifted along the $[1,1,1]$ -direction. The resulting crystal structure belongs to the space group 216, $F\bar{4}3m$, $C1b$ [19], with the Wyckoff positions 4a (0,0,0) for X , 4b (1/2, 1/2, 1/2) for Y and 4c (1/4, 1/4, 1/4) for Z , with a void at (3/4, 3/4, 3/4). The individual positions can be filled with a wide variety of elements, an overview of which is given in Figure 1.7. The X and Z elements form a strongly covalent bond, while the bond between X and Y has a distinct ionic character [19]. This relationship between the constituent elements forms the basis for a wide range of electronic properties. Half-Heusler materials can behave as semiconductors [20], topological insulators [20], Weyl-semimetal [21] and ferromagnetic [22] materials, depending on their composition. Among the different element combinations, those with a total number of 18 valence electrons stand out, as they form especially stable semiconductors. This can be explained in a simplified picture, with charge being transferred from the X to the Y and Z -position, which attain a filled d^{10} and a filled s^2p^6 -shell configuration, respectively. By choice of composition, their band gap can effectively be tuned within a range of 0-4 eV.

1.3.1 Self-Doping Effects

Predicting the exact value of half-Heusler bandgaps from theoretical calculations remains a challenge. This is because their crystal structure is prone to disorder phenomena which can interfere with the intrinsic band-structure. In ZrNiSn, for example, the theoretical bandgap of 0.5 eV [23] stands in contrast to experimental values of 0.13 [24] to 0.18 eV [25]. This effect is most commonly explained by population of the void by Y-species atoms, either from migration from their original position [26] or over-stoichiometry [23]. This defect forms an impurity band within the bandgap and simultaneously lowers the edge of the conduction band [27]. By this mechanism, the bandgap vanishes for a prevalence of 25% of Y-atoms in the voids, leading to metallic or semi-metallic behavior. Alternatively, an X-Z site-antisite switching of 15% was predicted to close the bandgap in ZrNiSn [28], causing a similar effect.

These two causes of self-doping effects, which can act either donor or acceptor-like, can explain the overall transport properties of most semiconducting half-Heusler compounds. An overview of the most common processes in individual compounds is given in Figure 1.8. When developing applications from these materials, special care must be taken to account for this disorder phenomena in addition to the intrinsic band structure.

	Donor		Acceptor	
ZrNiSn	Ni(i) Low ΔH V. shallow	V(Sn) High ΔH shallow	V(Zr) High ΔH V. shallow	Sn-on-Zr Low ΔH V. deep
ZrCoSb	Co(i) Low ΔH V. shallow	V(Co) Low ΔH deep	V(Zr) Low ΔH deep	Sn-on-Sb Low ΔH deep
ZrPtSn	Pt(i) High ΔH V. deep	Zr(i) High ΔH shallow	Sn-on-Zr Low ΔH deep	V(Zr) High ΔH shallow
ZrIrSb	Sb-on-Zr Low ΔH deep	Ir(i) High ΔH shallow	Sb-on-Zr Low ΔH deep	V(Zr) High ΔH shallow
TaIrGe	Ir(i) High ΔH shallow	Ge(i) High ΔH shallow	Ge-on-Ta Low ΔH shallow	V(Ta) High ΔH deep

Figure 1.8: Summary of doping trends in a selection of half-Heusler semiconducting compounds. For each system typical donors (red) and acceptors (blue) are shown, with the dominant species in bold face. X(i) denotes interstitials of the species X, V(X) voids on X-atom position and Y-on-X extrinsic doping of Y-atoms on the X-position. Additionally, the defects are categorized by their formation energy ΔH and as deep, very deep, shallow and very shallow dopants, depending on their respective ionization energies.

Reprinted figure with permission from Yonggang G. Yu, Xiuwen Zhang, and Alex Zunger, Physical Review B, Volume 95, pages 1–25, copyright 2017 by the American Physical Society [29].

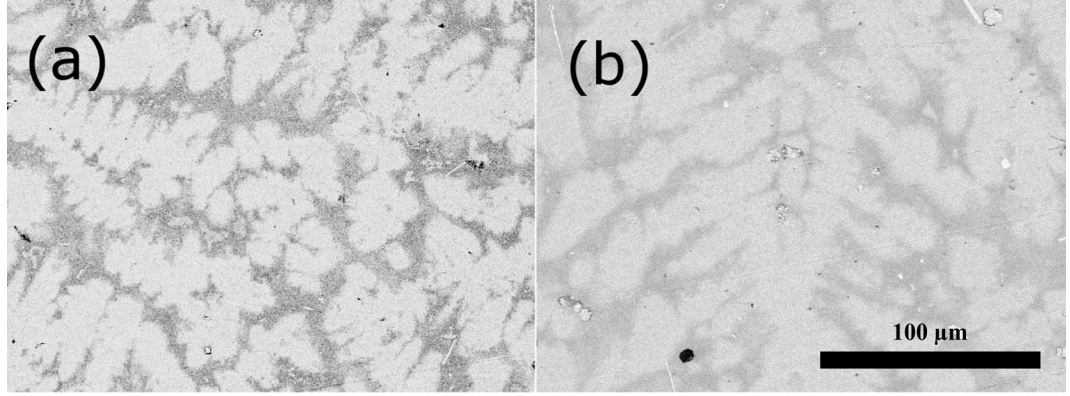


Figure 1.9: Spontaneous phase separation in $\text{Ti}_x(\text{Zr}_{0.5}\text{Hf}_{0.5})_{1-x}\text{NiSn}$ with

a) $x = 0.5$, as cast and

b) $x = 0.34$, annealed.

Reprinted from Geng, Huiyuan, and Hao Zhang. 2014. “Effects of Phase Separation on the Thermoelectric Properties of (Ti, Zr, Hf)NiSn Half-Heusler Alloys.” *Journal of Applied Physics* 116 (3): 33708, with the permission of AIP Publishing [30].

1.3.2 Spontaneous Phase Separation

While the electronic properties of many half-Heusler materials facilitate highly efficient thermoelectric conversion, the thermal properties limit their use. Their thermal conductivity is on the order of 10 W/mK [31] and therefore roughly 5 times higher than currently used BiTe at around 2 W/mK [32]. While most thermal conductivity reduction methods are well established, like complex alloying [33] and microstructuring [34], the unique phase diagram of this material family enables material specific approaches. By choice of composition, an intrinsic phase instability can be provoked, which leads to the spontaneous formation of dendritic structures on a microscale. This property has been employed both in n-type $(\text{Hf}_a\text{Zr}_b\text{Ti}_c)\text{NiSn}$ [30], Figure 1.9, and p-type $(\text{Hf}_a\text{Zr}_b\text{Ti}_c)\text{CoSb}_{0.85}\text{Sn}_{0.15}$ [35], where it mainly leads to a variation on the a , b , c -positions. As a consequence, Rausch et al find a reduction of 40% in the thermal conductivity from $\text{TiCoSb}_{0.85}\text{Sn}_{0.15}$ to $(\text{Hf}_{0.5}\text{Ti}_{0.5})\text{CoSb}_{0.85}\text{Sn}_{0.15}$.

2 Thermal Transport

2.1 Phonon Dispersion Relation

In a dielectric medium heat is transported by phonons, i.e. sets of atomic displacements that correspond to a quantum of lattice vibrational energy. They result from an interplay of attractive and repulsive forces in a crystal. While the potential resulting from the interaction of atoms can take a complex form, it can be approximated as a harmonic potential

$$U = -\frac{1}{2}C(d - d_0)^2, \quad (2.1)$$

where d is the distance between two atoms, d_0 is the equilibrium spacing and C is the force constant which expresses the strength of their interaction. This potential results in a force that is linear to the deviation of the atomic position from equilibrium. For an atom α in a unit cell n , the force exerted from all other atoms in the crystal combine to a total force [36]

$$F_i = - \sum_{m,\beta,j} C_{nai}^{m\beta j} u_{m\beta j} \quad (2.2)$$

where i, j indicate the spatial coordinates, α and β the atomic species within a unit cell, n and m the unit cells, $C_{nai}^{m\beta j}$ the force constant, $u_{m\beta j}$ the deviation of the atom $m\beta$ from equilibrium.

From this sum of external forces, a set of equations of motion results

$$M_\alpha \frac{\partial^2 u_{nai}}{\partial^2 t} + \sum_{m,\beta,j} C_{nai}^{m\beta j} u_{m\beta j} = 0, \quad (2.3)$$

with the mass of an individual atom M_α .

However, expression 2.3 corresponds to $3N$ coupled differential equations, where N corresponds to the total number of atoms in the crystal. The set of equations can be decoupled with the ansatz [36]

$$u_{nai} = \frac{1}{\sqrt{M_\alpha}} A_{ai}(\vec{q}) e^{i(\vec{q} \cdot \vec{R}_n - \omega t)}, \quad (2.4)$$

2 Thermal Transport

with the wavevector \vec{q} and the unit cell position \vec{R}_n . Inserted back into expression 2.3 this leads to

$$\begin{aligned} -\omega^2 A_{\alpha i}(\vec{q}) + \sum_{\beta, j} \sum_m \frac{1}{\sqrt{M_\alpha M_\beta}} C_{n\alpha i}^{m\beta j} e^{i\vec{q} \cdot (\vec{R}_m - \vec{R}_n)} A_{\beta j}(\vec{q}) &= 0 \\ -\omega^2 A_{\alpha i}(\vec{q}) + \sum_{\beta, j} D_{\alpha i}^{\beta j}(\vec{q}) A_{\beta j}(\vec{q}) &= 0 \end{aligned} \quad (2.5)$$

with the dynamical matrix

$$D_{\alpha i}^{\beta j}(\vec{q}) = \sum_m \frac{1}{\sqrt{M_\alpha M_\beta}} C_{n\alpha i}^{m\beta j} e^{i\vec{q} \cdot (\vec{R}_m - \vec{R}_n)}. \quad (2.6)$$

The dynamical matrix does not depend on n and m , because it contains only the difference in unit cell positions $\vec{R}_m - \vec{R}_n$ and because it sums over all unit cells, so the choice of the unit cell \vec{R}_n is arbitrary. This is why equation 2.5 corresponds only to a system of $3r$ coupled differential equations instead of $3N$, where r is the number of atoms in a unit cell. The solutions $\omega(\vec{q})$ of this system express the dispersion relation of lattice vibrations in the system with $3r$ branches.

Because of the translational symmetry of a crystal, solutions for each of these branches can be derived from a one-dimensional problem. This is illustrated in Figure 2.1 for a mono-atomic crystal, with the atomic displacements perpendicular to the crystal planes in x-direction. An elastic wave in x-direction propagates and the forces both in y- and z-direction cancel out. Therefore, only atoms along one axis have to be considered and together with the approximation of only nearest neighbor interaction the sum of forces on an atom at position n becomes

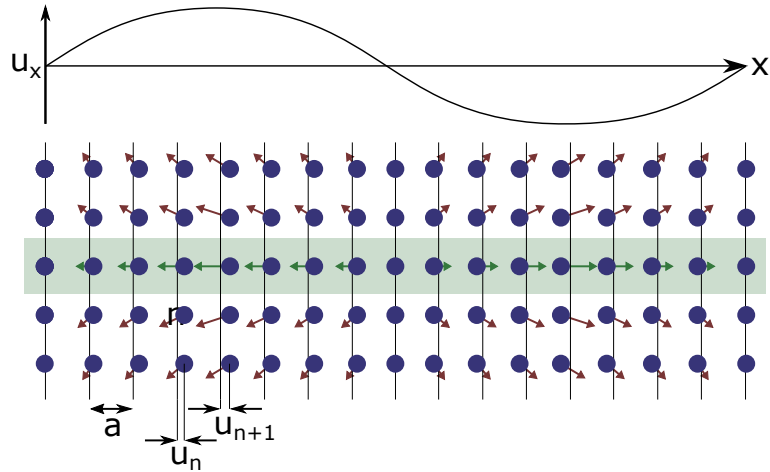


Figure 2.1: Illustration of a longitudinal wave in a one-atomic lattice. The arrows express the force exerted by the atoms in the green box. Because of the symmetry of the system, the force components perpendicular to the x-direction compensate each other. The graph in the upper part of the figure displays the displacement in x-direction in dependence of the position x . (Red colored vectors are displayed exaggerated relative to green vectors.)

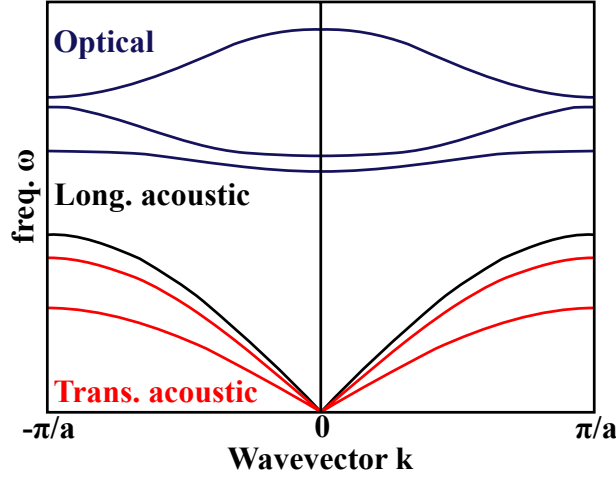


Figure 2.2: Typical phonon dispersion relation $\omega(k)$ with the longitudinal acoustic branch in black, the transversal acoustical branches in red and the optical branches in blue.

$$F = F_{n \leftrightarrow n+1} + F_{n \leftrightarrow n-1} \quad (2.7)$$

$$= C(u_{n+1} - u_n) + C(u_{n-1} - u_n), \quad (2.8)$$

with the spring constant C that expresses the rigidity of the lattice, the interatomic distance d and an equilibrium distance d_0 .

Thus, two forces enter into the equations of motion of a mass point, one from each neighbor:

$$M \frac{\partial^2 u_n}{\partial t^2} = C(u_{n+1} + u_{n-1} - 2u_n), \quad (2.9)$$

with the abbreviations illustrated in Figure 2.1, u_n as the deviation of a mass-point from its rest position and M as its mass.

The ansatz $u_0 = \exp(i\omega t)$ solves the differential equation and expresses the displacements along the chain following a sinusoidal-like wave [37]:

$$-M\omega + 2C = C \left[e^{i(\phi_{n+1} - \phi_n)} + e^{i(\phi_{n-1} - \phi_n)} \right] \quad (2.10)$$

Assuming the wave is continuous, the phase shift between neighboring mass points is constant, and thus can be abbreviated with $\phi_n - \phi_{n-1} = \phi_{n+1} - \phi_n = -qa$:

$$M\omega^2 = 2C(1 - \cos(qa)) = 4C \sin^2(qa/2) \quad (2.11)$$

2 Thermal Transport

From equation 2.11 the dispersion relation follows, which expresses the relation of frequency and wavevector:

$$\omega = 2\sqrt{\frac{C}{M}} \left| \sin\left(\frac{qa}{2}\right) \right|. \quad (2.12)$$

This result is shown with the black line in Figure 2.2 for an interval between $q = 0$ and $q = \pm \frac{\pi}{a}$, corresponding to the first Brillouin zone.

This solution is valid for elastic waves in crystal, in which the displacements are confined to the propagation direction of the wave, so called longitudinal waves. In general the atoms can also be displaced perpendicular to the wavevector, in which case the same analysis can be applied, with differing spring constants C . This leads to two additional, so called transversal branches of the dispersion relation, which can be degenerate, depending on the symmetry of the crystal [37].

For lattices with different atoms in their unit cell, the dispersion relation exhibits additional branches, which correspond to neighboring atoms having opposite phases. These branches are called optical branches, as in ionic compounds they couple to electromagnetic radiation [38]. In this case the opposite displacement leads to an oscillating dipole-moment, which can absorb or emit radiation that is typically in the infrared range. The optical branches are separated from the acoustical branches by a gap and become flat towards small wave-vectors. For a unit cell with r atoms, the dispersion relation consequently contains $3r$ branches, of which $3r - 3$ branches correspond to optical branches [13].

2.2 Lattice Thermal Conductivity

This dispersion relation is an important key for understanding the lattice thermal conductivity, as it expresses characteristic features of the phonons responsible for transporting heat. Figure 2.3a and b shows the dispersion relation of HfNiSn and TiNiSn, with the accumulated thermal conductivity at room temperature shown in Figure 2.3c. The dispersion relation and thermal conductivity were simulated by Eliassen et al. using the phonon-transport Boltzmann equation within the relaxation time approximation for an ideal crystal structure [39]. The boxes in Figure 2.3c mark the areas that dominate thermal transport, with 80% of heat being transported by phonons in this region. With a maximum energy of around 16 meV it becomes clear that the acoustic branches contribute to the heat transport almost exclusively. This is because they have a higher phonon propagation velocity than other branches and are lower in energy, making them more likely to be occupied. The propagation velocity is measured by the group velocity $v = \frac{\partial\omega}{\partial k}$, which quantifies the traveling speed of a wave packet in a material. From this definition it becomes clear that optical branches can contribute much less to thermal conductivity, as they are significantly flatter. The group velocity is one of three major contributing factors, which enter into the definition of the lattice thermal conductivity [7]:

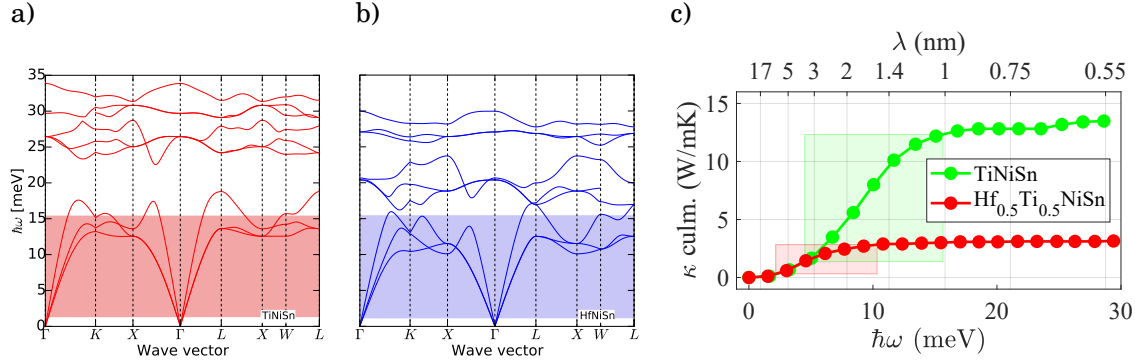


Figure 2.3: Phonon spectra of different members of the (Hf, Zr, Ti)NiSn material family.

a) Dispersion relation of TiNiSn, calculated via the Boltzmann equation within the relaxation time approximation, by [39]. The area, which is responsible for 80% of thermal transport is shaded in red.

b) Dispersion relation of HfNiSn from the same study.

c) Cumulative thermal conductivity in dependence of phonon energy, adapted from [39]. The shaded areas account for 80% of thermal transport. The wavelength scale in the second x-axis assumes an averaged group velocity for the acoustical branches of TiNiSn[40].

$$\kappa = \frac{1}{3} \sum_j \int_0^{\omega_{max}} c_j(\omega) v_j(\omega) l_j(\omega) d\omega \quad (2.13)$$

with the spectral heat capacity c_j , the group velocity v and the mean free path l , each of which is dependent on the branch j and the frequency ω . The spectral heat capacity expresses the amount of heat that is carried by phonons of a specific frequency and thus is mainly given by the density of states derived from the phononic band structure. The mean free path quantifies the amount of scattering, by giving the distance a phonon will travel on average before exhibiting a scattering event.

2.3 Phonon Scattering Mechanisms

In thermoelectric material research, the quantities expressed in equation 2.13 are specifically manipulated to engineer effective thermal barriers and thus increase their conversion efficiency. The most common strategy is aimed at the mean free path, which is decreased in a targeted way, while leaving the remaining properties widely intact. According to Matthiessen's rule, the contributions can be separated and analyzed separately [42]:

$$l_{eff}^{-1} = l_{umkl}^{-1} + l_{imp}^{-1} + l_{intf}^{-1} + l_{bdry}^{-1} \quad (2.14)$$

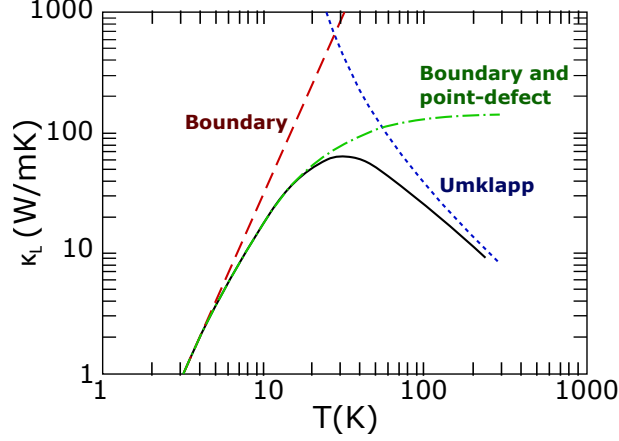


Figure 2.4: Thermal conductivity of CoSb_3 for temperature from 1 K to room temperature. The estimated thermal conductivity only considering boundary scattering is marked in red, while for the green curve also point-defect scattering is included. The umklapp-scattering contribution is marked in blue. The figure is adapted from [41].

l_{umkl} is the most prevalent phonon-phonon scattering mechanism that violates the quasi-momentum conservation and therefore effectively randomizes the phonon propagation direction. It becomes dominant passing a characteristic energy threshold and is therefore most apparent at intermediate and high temperatures [13]. A CoSb_3 thermal conductivity curve is shown in Figure 2.4, which follows this typical behavior, in which the umklapp-scattering [43] sets in at some tens of K.

Impurity scattering, expressed by l_{imp} , is also most significant at higher temperatures, as it exhibits a characteristic $l_{imp}^{-1} \propto \omega^4$ -dependence [44], leading to an effective filtering of high-frequency and therefore high-energy phonons. It is caused by the scattering of phonons on defects in the lattice, as foreign atoms or structural imperfections [45]. Consequently, in disordered solids the dominant phonon range is shifted towards lower frequencies, corresponding to longer wavelengths [46]. This can be observed comparing $\text{Ti}_{0.5}\text{Hf}_{0.5}\text{NiSn}$ and TiNiSn in Figure 2.3c, where low frequency phonons are significantly less affected by the increased mass fluctuation in the mixed compound. However, this simulated thermal conductivity corresponds to an idealized crystal, while actual measurements on TiNiSn typically yield values between the TiNiSn and $\text{Ti}_{0.5}\text{Hf}_{0.5}\text{NiSn}$ curves, indicating scattering by naturally occurring defects [39]. As impurity scattering serves to inhibit heat transport significantly, it is a common, straight forward strategy to substitute isoelectronic atoms in a host material, for example in the (Ti, Zr, Hf)NiSn material family. As Ti, Zr and Hf have the same number of valence electrons, they are likely to create a similar electronic background, while the atomic masses are different enough to create significant acoustic contrast [47]. While this scattering mechanism is effective and easy to implement, its use is limited to the high-frequency end of the phonon spectrum.

In contrast, external boundary scattering specifically scatters phonons with larger

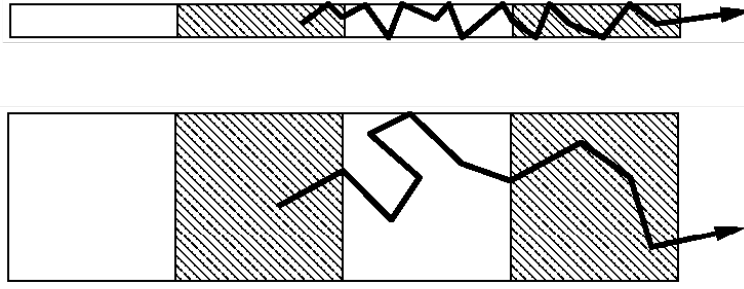


Figure 2.5: Illustration of the mean free path limitation in nanowires of different diameters. Adapted from [58]

wavelengths [48]. It occurs when the intrinsic phonon mean free path exceeds the system size in one or more dimensions. In this case the phonon is scattered at the surface, confining it inside the sample volume. This effect of a naturally limited mean free path can be observed in low-dimensional systems like 2D-materials [49], thin films [50] and nanowires [51]. Figure 2.5 shows an illustration of this approach, where the thermal conductivity is manipulated using the nanowire diameter. By this method, a 4 to 8-fold reduction in the thermal conductivity can be registered [52]. Additionally, this approach can be combined with mass fluctuation scattering, leading to the distortion of a broad spectrum of lattice vibrations with long and short wavelengths. [53].

However, using external boundary scattering is only useful in systems, where constraining the dimensions is feasible and practicable, limiting it to niche applications. Much more prevalent in a variety of bulk and nanostructured systems is scattering on internal boundaries with sufficient acoustic contrast. It is caused by abrupt changes of lattice properties by grain boundaries, composition changes in multi-phase materials, or large scale defects. As opposed to external boundary scattering, only a part of the phonons is scattered, their portion depending on the material and interface quality. Naturally, materials with a high number of internal boundaries, like multi-crystalline materials, exhibit a relatively low thermal conductivity. This is why in the recent years, internal interfaces have been purposefully integrated into common materials by composite inclusion [54], by provoking intrinsic phase-separation [55] and thin film multilayer generation [56]. Most of these processes correspond to fundamentally random processes, where the number and properties of individual interfaces can only be controlled indirectly. In contrast to this, superlattices consist of a well defined periodic layer sequence. Being conceptually a bottom-up approach, this method gives freedom to manipulate the interface density and, to some degree, the interface quality [57]. Given the unique properties and the system-specific phenomena arising from them, the following section will be dedicated to exploring superlattices in detail.

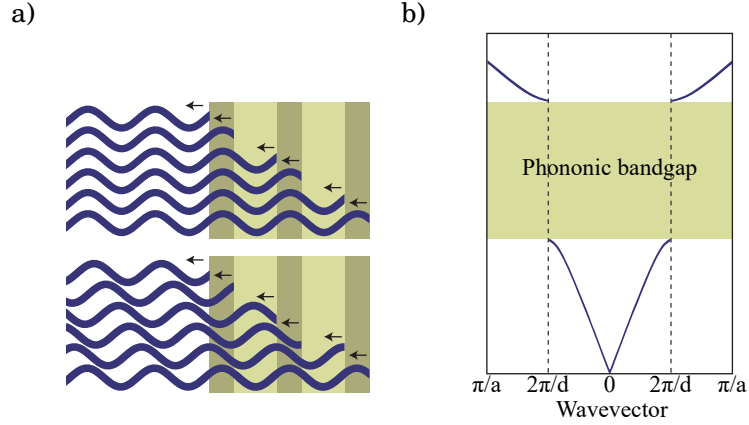


Figure 2.6: Illustration of phonon interference that leads to the opening of a band-gap in the dispersion relation. With the Brillouin-zone boundary π/a and the period length d

- a) When the constructive interference criterion $k = 2\pi/d$ is met (top), 100% of the incoming wave is reflected, and phonons can't propagate into the system. Other wavelengths are partly transmitted and partly reflected.
- b) Sketch of the resulting dispersion relation. The band-gap corresponds to the area, where the interference condition is met. Adapted from [59].

2.4 Interface Scattering in Multilayer Systems

Superlattices are systems which are characterized by a coherent crystal structure and a layer sequence, which is superimposed on it. The individual layers can be composed of similar materials, like in AlAs-GaAs systems [60] or distinct compounds, e.g. in the case of inorganic organic superlattices [61]. They tend to be heavily dominated by the interfaces in the cross-plane direction, while their influence along the planes is more subtle. This makes them strongly anisotropic, with the thermal conductivity being drastically different between the main directions [62]. Classically, superlattice properties have been modeled as the sum of its constituent's contributions [63]. However, at characteristic sizes in the nm-range, it becomes clear that complex interactions between parts of the system have to be considered [64]. Specifically the phonon dispersion relation can be widely altered by the additional layer structure, giving a new avenue for thermal barrier optimization [65]. While mass fluctuation, external boundary and interface scattering all serve to increase overall scattering, altering the phonon dispersion relation can impact the group velocity and spectral heat capacity. Thus, it represents an interesting alternative in many material systems, where scattering-based approaches are not viable or effective [66].

Because of the periodic arrangement of interfaces, phonons scattered at different boundaries can interfere either constructively or destructively with each other, depending on their wavelength. These interference effects lead to band-gaps within the phonon

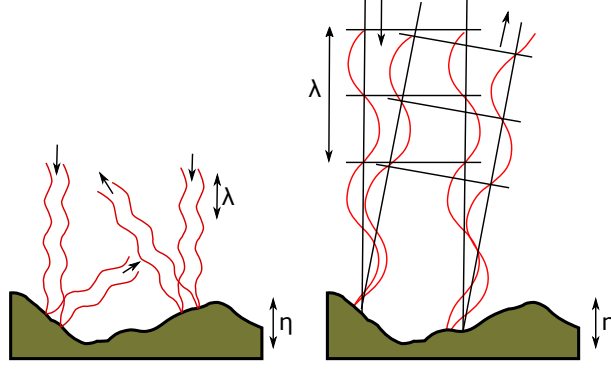


Figure 2.7: Interplay between boundary roughness and phonon wavelength. The left side shows phonons scattering on a surface with a higher roughness than their wavelength, effectively randomizing their propagation direction. On the right side scattering with longer wavelength phonons is illustrated, in which case their phase relationship is conserved. [72]

dispersion relation and to characteristic band-bending in the vicinity of the gap [59]. Because of the band-bending, branches of the phonon dispersion become significantly flatter, leading to a reduced group velocity. Figure 2.6 illustrates both elastic waves reflected without significant interference and constructively interfering elastic waves and the resulting band-gap. Phonons reflected at the individual interfaces are reflected to 100% if they overlap constructively, i.e. when their wavelength coincides with the interference condition

$$d = \lambda = \frac{2\pi}{k} \quad (2.15)$$

with the period length d , the wavelength λ and the wavevector k . Multiple phononic bandgaps can be present [67]. Thus the effect of phonon interference gets weaker, towards smaller structure sizes [68]. However, while the dispersion-relation manipulation has been demonstrated to be effective in a variety of materials [69, 70, 58], it is intrinsically limited by the material and interface properties.

Most scattering events effectively randomize the phonon propagation direction. Therefore, the phonon mean free path must be long compared to the characteristic structure size, so that phonons reflected at different interfaces have a fixed phase relation towards each other [71]. This requires low structure sizes, as phonon-phonon scattering limits the mean free path intrinsically, and sufficient interface quality, to inhibit interface scattering.

Depending on the amount of scattering at the interfaces and within the layer, different thermal transport regimes in a superlattice can be identified. The specific regime depends on the bulk mean free path of the constituent materials, the superlattice period, the total superlattice thickness and the amount of diffusive interface scattering. In Figure

2 Thermal Transport

2.8, 5 cases are differentiated based on these parameters, displaying their characteristic thermal transport behavior [67]:

- a) The bulk mean free path of the constituent materials is larger than the overall system size and the interfaces are smooth enough, to suppress diffusive scattering. In this case the thermal conductance G is dominated by the contact resistance of the outer boundary, and is thus independent of system size L . The thermal conductivity $\kappa = GL$ therefore increases with L , as the phonons traverse the superlattice ballistically. The thermal conductivity is lowered by phonon interference, the impact of which diminishes with shorter periods [68]. Therefore the thermal conductivity increases with decreasing period length.
- b) The bulk mean free path exceeds the system size. However, diffusive scattering at the interface limits the mean free path and suppresses interference effects. Thus, the thermal conductivity increases with a larger period length, corresponding to a lower interface density. The system size does not impact the thermal conductivity, as the diffusive interface scattering prevents ballistic transport.
- c) The bulk mean free path is smaller than the system size, but exceeds the period length. The thermal conductivity is governed by both phonon-phonon scattering and interference effects. The interfaces are sufficiently smooth so that diffusive scattering can be neglected. Therefore, the thermal properties correspond to the bulk properties with a dispersion relation modified by interference effects. Consequently, a similar dependence on the period length as in case a) emerges.
- d) Interface scattering dominates, while bulk-like phonon-phonon scattering still plays a significant role. The main limiting factor therefore is the interface density and thus the thermal conductivity decreases towards smaller periods.
- e) Thermal transport is completely dominated by inner-layer scattering. The superlattice and mean bulk thermal conductivity coincide and therefore any dependence on system size or period length vanishes.

Diffusive interface scattering destroys phonon coherence and can thus suppress the influence of interference effects [73]. However, in the absence of diffuse mechanisms, a phonon is not necessarily transmitted to 100%, as it can be subject to so called specular interaction with the boundary layer [62]. The interface topography dictates the nature of phonon interface scattering [74], and thus can break or preserve coherence, which is illustrated in Figure 2.7. For smooth surfaces, the incident angle coincides with the angle of reflection, representing specular scattering, similar to light waves being reflected of a dielectric boundary. For a higher roughness, the scattering process of a phonon tends to be affected by irregular interface features and thus they are scattered diffusely. Because of the random nature of the underlying processes, a quantitative analysis is complex and depends on the exact definition of the roughness parameter η . It can be expressed by the root-mean-squared of the deviation of the interface mean plane or by the characteristic feature size. Similarly, the scattering mechanism can be characterized differently, with

2.4 Interface Scattering in Multilayer Systems

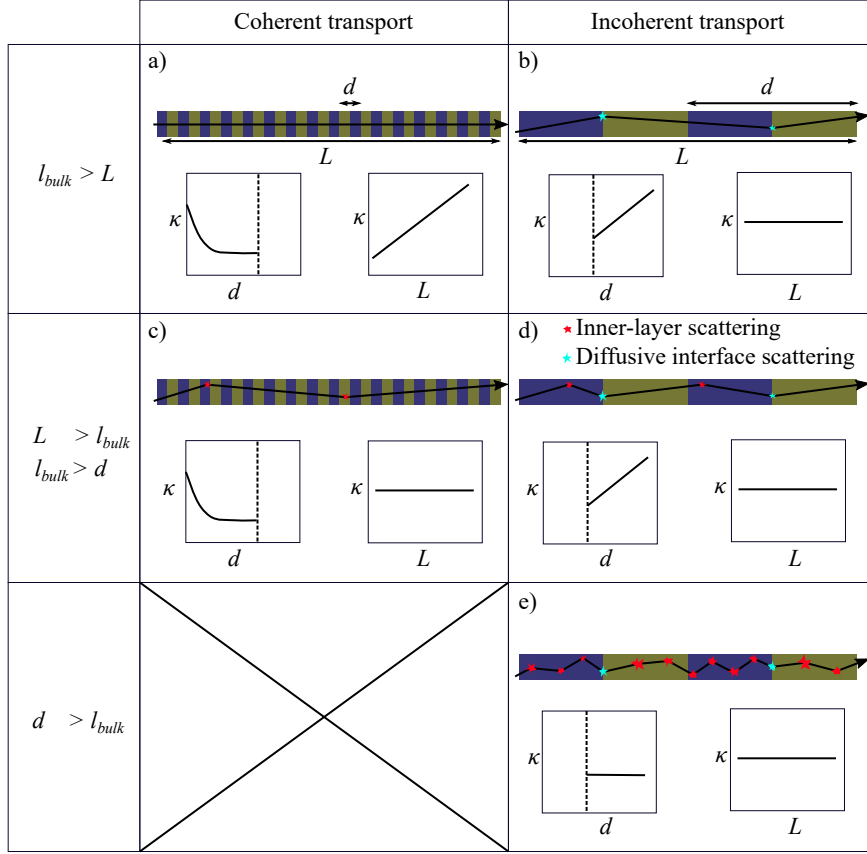


Figure 2.8: Thermal transport regimes in superlattices. The left side corresponds to the coherent regime, with comparatively short period length, little intrinsic scattering and smooth interfaces (a and c). Phonons traverse multiple periods before being scattered diffusely.

On the right side diffusive scattering dominates, in form of interface scattering (b and d) or bulk-like scattering (e).

For each case an exemplary phonon trajectory is traced, with marked diffuse interface and inner-layer scattering. The inset depicts the typical thermal conductivity in dependence of the period length and total superlattice thickness, respectively. Adapted from [67]

2 Thermal Transport

fully diffusive and fully specular scattering representing extreme cases of a spectrum. This spectrum can be quantified with the specularity parameter p , where $p = 1$ corresponds to specular scattering and $p = 0$ diffusive scattering. With definitions above, the relationship between roughness and scattering type can be estimated as [74]:

$$p = \exp\left(\frac{-16\pi^2\eta^2}{\lambda^2}\right) \quad (2.16)$$

While estimations of the specularity criterion vary [59], the relation between wavelength and roughness is crucial, with a long enough wavelength and high enough interface quality being prerequisites for specular scattering [75]. This sets high demands to interface preparation, with, for example in TiNiSn, 80% of the heat being carried in a wavelength range of 1-3.5 nm at room temperature (see Figure 2.3c). However, it also presents mass fluctuation scattering as an avenue to influence the interface scattering regime, with short wavelength phonons being effectively filtered [76]. This effect can be observed in Hf_{0.5}Ti_{0.5}NiSn, where the dominant frequency band is shifted towards higher wavelengths compared to both HfNiSn and TiNiSn.

When predicting the thermal boundary resistance for a given set of materials, the introduced interface specularity plays a crucial role. For the extreme cases of a very low and high interface qualities, corresponding to $p=0$ and $p=1$, respectively, concise treatments are possible. These are given by the diffusive mismatch model and the acoustical mismatch model, respectively. While in practice a combination of both has to be considered in most cases, the two models are illustrative of the underlying scattering processes at the interface.

2.4.1 Diffusive Mismatch Model

The diffusive mismatch model assumes that all phonons encountering the interface are scattered diffusely. Diffuse scattering leads to a randomization of the propagation direction after the scattering event, i.e. the resulting direction is independent of the initial direction. In the case of low and intermediate temperatures, the phonon energy can be assumed as conserved [75]:

$$\hbar\omega_{incident} = \hbar\omega_{transmitted} \quad (2.17)$$

Consequently, the propagation direction, resulting from forward or back-scattering, depends only on the number of available states on either side and their associated group velocity. The transmission coefficient, specifying the ratio of phonons that are being transmitted by a specific interface, is therefore given by [75]

$$T(\omega) = \frac{\sum_j v_j^B(\omega) \delta_j^B(\omega)}{\sum_j v_j^A(\omega) \delta_j^A(\omega) + \sum_j v_j^B(\omega) \delta_j^B(\omega)} \quad (2.18)$$

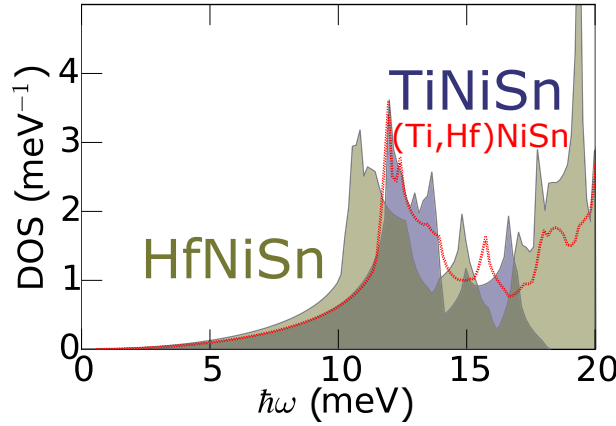


Figure 2.9: Phonon density of states of HfNiSn and TiNiSn and their overlap. The red line corresponds to the 50-50 mixture of both materials, $\text{Ti}_{0.5}\text{Hf}_{0.5}\text{NiSn}$. The phonon energies 0-20 meV encompass the range that dominates heat transport, and is mainly represented by the acoustic band. Density of state calculation from [39].

Where v is the group velocity and δ is the density of states, both of which are phonon branch, i, j , and material specific, A, B .

Consequently, the thermal resistance of an interface is mainly determined by the overlap of the density of states of the materials on either side of the boundary. The density of states of both TiNiSn and HfNiSn is shown in Figure 2.9, with the overlapping part being marked. HfNiSn, exhibiting a higher atomic mass, has a higher share of low frequency phonons, as is to be expected from equation 2.12. Therefore the maxima in the density of states, corresponding to the band edge of the acoustic band, of TiNiSn and HfNiSn do not overlap. However, depending on the interface quality, there is a more or less thick boundary, where TiNiSn and HfNiSn are intermixed, forming an effective third layer of $(\text{Ti}, \text{Hf})\text{NiSn}$. This layer has intermediate acoustic properties and effectively increases the overlap between both materials. This effect is called phonon bridge effect [77], and can be employed purposefully, when an acoustic buffer is applied between two materials to locally lower acoustic contrast and mediate thermal transport. Model calculations have shown that this effect could lower the thermal resistance of interfaces by a factor of 2 [78]. However, as an additional layer also alters interface properties the effect of an acoustic buffer is highly non-trivial.

While diffuse scattering is the dominant scattering mechanism in most systems at room temperature, specular scattering often has a non-negligible contribution [79]. In specific experimental conditions it can become the main scattering mechanism, in which case the acoustic mismatch model is the more appropriate theoretical framework [80].

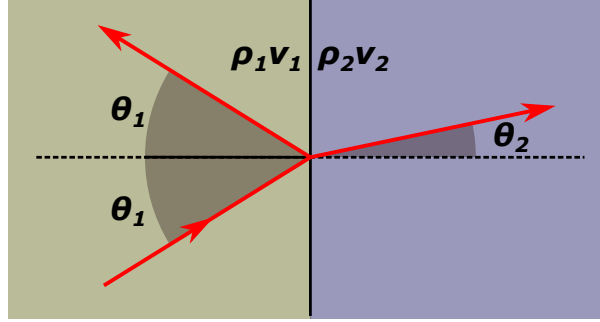


Figure 2.10: Illustration of scattering on a model interface according to the acoustic mismatch model. The interface is a perfect plane and the involved materials are completely characterized by their acoustic impedance, the product of mass density and sound velocity $Z = \rho v$.

2.4.2 Acoustic Mismatch Model

In the acoustic mismatch model an interface is idealized as a perfect plane and both materials as continuous media, disregarding the fundamentally quantized nature of the lattice. In this case the interface interaction can be described by classical wave dynamics, analogous to a light wave encountering a dielectric boundary layer. Consequently, Snell's law applies [81]:

$$\frac{\sin \theta_2}{\sin \theta_1} = \frac{v_2}{v_1}, \quad (2.19)$$

with, corresponding to the sketch in Figure 2.10, the incident and transmitted wave angles θ_1 and θ_2 , respectively, and the material propagation velocities v_1 and v_2 . It relates the change of propagation direction of a wave across an interface with the group velocities of the materials joined at the boundary. To derive the energy transmission across the interface, the mass density ρ has to be considered additionally, making the acoustic impedance $Z = \rho v$ the defining quantity of a material. Following the classical acoustic wave theory, the rate of energy transfer across an interface for a given incident angle is given by [75]

$$T_{1 \rightarrow 2}(\theta_1) = T_{2 \rightarrow 1}(\theta_2) = \frac{\frac{4Z_2}{Z_1} \cdot \frac{\cos(\theta_2)}{\cos(\theta_1)}}{\left(\frac{Z_2}{Z_1} + \frac{\cos(\theta_2)}{\cos(\theta_1)} \right)^2} \quad (2.20)$$

and for phonons with normal incidence [75]:

$$T_{1 \rightarrow 2, \perp} = T_{2 \rightarrow 1, \perp} = \frac{4Z_2 Z_1}{(Z_1 + Z_2)^2} \quad (2.21)$$

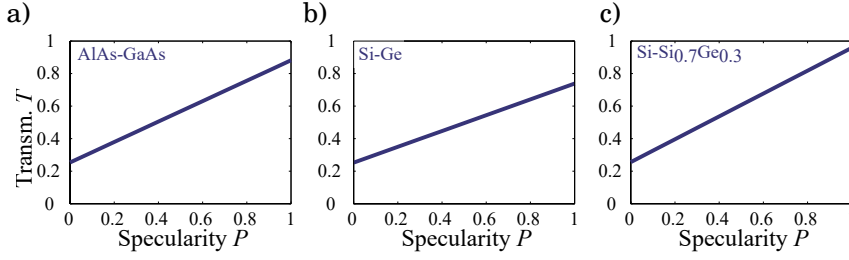


Figure 2.11: Simulated transmissivity coefficient of a given interface in dependence of the specularity parameter P

a) For a AlAs-GaAs interface.

b) For a Si-Ge interface.

c) For an Si-Si_{0.7}Ge_{0.3} interface.

Adapted from [83].

which means that the thermal boundary resistance depends on the acoustic contrast given by the ratio of the acoustic impedances Z_1 and Z_2 at the interface.

However, the assumption of an ideal, planar interface requires the ratio λ/η to approach infinity. Experimentally, this can only be emulated adequately by in-situ prepared interfaces in low-temperature measurements, where most of the heat is transported by long-wavelength phonons. Realistic surfaces at room temperature tend towards low specularity parameters [82], with their thermal boundary resistance deviating significantly from predictions from AMM. Nevertheless, specular scattering often cannot be neglected outright, making a more sophisticated picture necessary, which combines both DMM and AMM.

2.4.3 Thermal Boundary Resistance of Non-Ideal Interfaces

Figure 2.11 shows the transmission coefficient of model interfaces considering a combination of AMM and DMM. The model permits different weights for either model, from fully specular AMM, $p = 1$, to fully diffusive DMM, $p = 0$ [83]. All three systems show a general trend of the diffuse scattering being significantly more effective. In fact, several non-equilibrium molecular dynamics studies show a strongly increased thermal resistance for lower interface specularity with the introduction of additional roughness [84, 85, 73]. However, the relation between interface quality and thermal resistance is non-trivial, with nano-scale roughness leading simultaneously to a decrease in acoustic contrast. Consequently, several studies found the opposite effect for broad boundary layers, with the phonon bridge effect counteracting decreased specularity [86, 77]. The relation between both effects depends on the details of the system, like the constituent materials, the exact interface topography and boundary layer width.

3 Electronic Transport

3.1 The Drude Model

Charge transport in a conducting solid is a complex many-body problem in which mobile charge carriers interact between each other and stationary ions. However, many aspects of these systems can be captured by much more basic models, which involve seemingly crude approximations. One important example is the Drude model, which treats the collection of charge carriers as an ideal gas with a static background of ions. It is based on the following fundamental assumptions [87]:

- A. The interaction between electrons is negligible.
- B. Upon acceleration in an external field, the charge carriers frequently collide with stationary ions, leading to an effective drift velocity v_d .
- C. The mean time between collisions τ is constant and the same for all charge carriers.

This set of prerequisites leads to an equation of motion in which the coulomb force caused by the external field F_c is counteracted by an effective dissipative force caused by collisions between electrons and ions, F_τ [7]

$$\begin{aligned} m \frac{d\vec{v}}{dt} &= F_c + F_\tau \\ &= -e\vec{E} - m \frac{\vec{v}_d}{\tau}. \end{aligned} \quad (3.1)$$

Due to the influence of frequent collisions with stationary ions, quantified by the mean time between two collision τ , electrons eventually reach the terminal velocity v_d .

To understand the physical meaning of the drift velocity, it is illustrative to consider the stationary case $\vec{v}=0$, in which

$$0 = -e\vec{E} - m \frac{\vec{v}_d}{\tau} \quad (3.2)$$

$$\vec{v}_d = -\frac{e\tau}{m} \vec{E} \quad (3.3)$$

This equation reveals that the drift velocity is proportional to the external electrical field with the electron mobility as the proportionality constant $\mu = -\frac{e\tau}{m}$.

Within the Drude approximation, all electrons exhibit the same mobility and therefore the same drift velocity. This drift velocity therefore is the mean velocity at which in a

3 Electronic Transport

given material charge is transported. With the material specific electron density n , the charge current density therefore becomes

$$\vec{j} = -n \frac{e^2 \tau}{m} \vec{E}. \quad (3.4)$$

While equation 3.4 reproduces the proportionality between a driving voltage and the current that is expressed in Ohm's law, it inherently neglects any influence of the band structure.

However, details of the band structure are crucial for determining the electronic transport properties for many materials. Flat conduction bands are less effective for transporting current than conduction bands with a strong curvature. This difference can be accounted for by using an effective mass m^* , which expresses the effect of band curvature

$$\frac{1}{m^*} = \frac{1}{\hbar^2} \frac{d^2 K}{dk^2} \quad (3.5)$$

Where $K(k)$ is the kinetic energy of the corresponding band.

Multiple bands with different values of the effective mass can contribute to charge transport, some of which with charge carriers with an apparent positive charge. In this case the charge is carried by electronic holes, which correspond to the absence of an electron in an otherwise filled band. Considering electronic holes and the contribution of multiple bands, the current density in a semiconductor becomes

$$\vec{j} = \left[-\sum_i n_i \frac{\tau_i}{m_i^*} + \sum_j p_j \frac{\tau_j}{m_j^*} \right] e^2 \vec{E} \quad (3.6)$$

with the band-specific hole density p_j and electron density n_i , respectively.

3.1.1 Electronic Transport in a Magnetic Field

In an external magnetic field, equation 3.1 has to be adapted to account for an additional Lorentz-force F_B [7]:

$$\begin{aligned} m \frac{d\vec{v}}{dt} &= \vec{F}_c + \vec{F}_B + \vec{F}_\tau \\ &= -e\vec{E} - e\vec{v}_d \times \vec{B} - m \frac{\vec{v}_d}{\tau}. \end{aligned} \quad (3.7)$$

In this case the Lorentz-force deflects the electrons perpendicular to the current direction and the magnetic field. For a geometry as depicted in Figure 3.1 with a magnetic field in z and the external current in x -direction, this leads to a charge build-up along the y -axis.

Analogous to the magnetic field-free case, the drift velocity can be inferred from the stationary case:

$$v_{d,x} = -\frac{e\tau}{m} [E_x + v_{d,y} B] \quad (3.8)$$

$$v_{d,y} = -\frac{e\tau}{m} [E_y - v_{d,x} B] \quad (3.9)$$

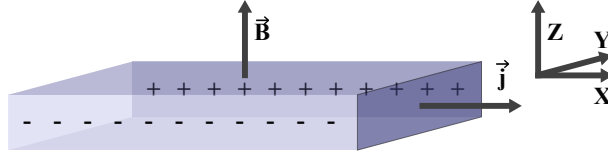


Figure 3.1: Illustration of the Hall effect in a conducting solid. The magnetic field in the Z-direction is perpendicular to an electrical current applied by an external electrical field. The Lorentz-force leads to an electrical field in y-direction and, as a consequence, to a charge build-up.

From which, with the relationship $\vec{j} = ne\vec{v}$, the current density results

$$\begin{aligned} \begin{pmatrix} j_x \\ j_y \end{pmatrix} &= \frac{\sigma_0}{1 + \frac{e^2 \tau^2}{m^2} B^2} \begin{pmatrix} 1 & -\frac{e\tau}{m} B \\ \frac{e\tau}{m} B & 1 \end{pmatrix} \begin{pmatrix} E_x \\ E_y \end{pmatrix} \\ &= \frac{\sigma_0}{1 + \omega_c^2 \tau^2} \begin{pmatrix} 1 & -\omega_c \tau \\ \omega_c \tau & 1 \end{pmatrix} \begin{pmatrix} E_x \\ E_y \end{pmatrix}, \end{aligned} \quad (3.10)$$

where $\sigma_0 = ne^2\tau/m$ is the magnetic field free electrical conductivity and $\omega_c = \frac{e\tau}{m}$ is the cyclotron frequency.

As the external current is applied along the x-direction, in equilibrium j_y is zero. In this case the Coloumb force from the charge build-up cancels the Lorentz-force and the y-component of equation 3.10 reveals a proportionality between E_x and E_y

$$\begin{aligned} 0 &= \frac{\sigma_0}{1 + \omega_c^2 \tau^2} [\omega_c \tau E_x + E_y] \\ \Rightarrow E_y &= -\frac{e\tau^2}{m} E_x. \end{aligned} \quad (3.11)$$

Here, E_x is the same as in the field free case. Therefore equation 3.4 can be used to determine it in dependence of the applied current density

$$E_x = -\frac{m}{ne^2\tau} j_x \quad (3.12)$$

with which equation 3.11 becomes

$$E_y = -\frac{1}{ne} B j_x = R_H B j_x \quad (3.13)$$

where the Hall constant is given by

$$R_H = -\frac{1}{ne}. \quad (3.14)$$

3 Electronic Transport

The Hall constant quantifies the magnitude of the Hall-voltage that is caused by a given electrical current in a magnetic field. It can be used to estimate an effective charge carrier density of a material. This effective charge carrier density can be accurate when only a single band contributes significantly to charge transport.

However, the interpretation of the Hall constant can be significantly more complex when multiple bands play a role. In this case different types of charge carriers have to be considered and a similar analysis as detailed above yields [7]

$$R_H = \frac{\sum_j p_j \mu_{p,j}^2 - \sum_i n_i \mu_{n,i}^2}{e (\sum_j p_j \mu_{p,j} + \sum_i n_i \mu_{n,i})^2} \quad (3.15)$$

where j sums over the hole-carrying bands and i over the electron-carrying bands that have to be considered in charge transport.

3.1.2 The Wiedemann-Frantz-Law

Despite of the crude approximation of the microscopic processes, the Wiedemann-Frantz-law can be derived from the Drude model, approximating the electrons as an ideal gas. The Wiedemann-Frantz-law says that the ratio of electrical and thermal conductivity in a metal for a given temperature is close to a constant value, which is given by the Lorenz-number LT . An excerpt of Lorenz-numbers for common metals at 273 K is given in table 3.1, most of which lay between 2.2 and $2.9 \cdot 10^{-8} \text{ W}\Omega/\text{K}$. To calculate this constant in the Drude-model, the thermal conductivity of an ideal gas $\frac{1}{2}v^2\tau k_B n$ is combined with the Drude conductivity from equation 3.4 [89]

$$\frac{\kappa}{\sigma} = \frac{\frac{1}{2}v^2\tau k_B n}{ne^2\tau/m} = \frac{1}{2}mv^2 \frac{k_B}{e^2} \quad (3.16)$$

Element	LT ($\cdot 10^{-8} \text{ W}\Omega/\text{K}^2$)	Element	LT ($\cdot 10^{-8} \text{ W}\Omega/\text{K}^2$)	Element	LT ($\cdot 10^{-8} \text{ W}\Omega/\text{K}^2$)
Li	2.22	Be	2.36	In	2.58
Na	2.12	Mg	2.14	Ti	2.75
K	2.23	Nb	2.90	Sn	2.48
Rb	2.42	Fe	2.61	Pb	2.64
Cu	2.20	Zn	2.28	Bi	3.53
Ag	2.31	Cd	2.49	Sb	2.57
Au	2.32	Al	2.14		

Table 3.1: Values for the Lorenz-number of common metals at a temperature of 273 K [88].

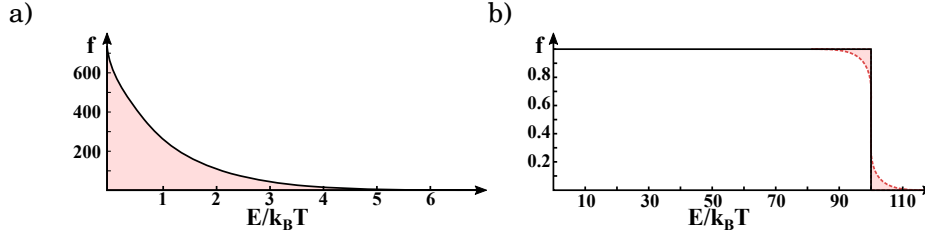


Figure 3.2: Common distribution functions used in the description of electronic transport. The shaded area marks states, that significantly contribute to charge transport.

a) The Boltzmann distribution at a finite temperature T .

b) The Fermi-Dirac distribution at 0 K (black solid line) and at a finite T (red, dotted line) with $E_F = 100k_B T$.

with the Boltzmann constant k_B . Using the mean kinetic energy in an ideal gas

$$\frac{1}{2}mv^2 = \frac{3}{2}k_B T \quad (3.17)$$

this expression simplifies to:

$$\frac{\kappa}{\sigma} = LT = \frac{3}{2} \left(\frac{k_B}{e} \right)^2 T \quad (3.18)$$

With the theoretical Lorenz-number

$$LT = 2.5 \cdot 10^{-8} \frac{W\Omega}{K} \quad (3.19)$$

3.1.3 The Limits of the Drude-model

The Drude model assumes that all electrons contribute to electronic transport, with their kinetic energy W distribution following the Boltzmann-statistics:

$$f_B(W) = n \left(\frac{m}{2\pi k_B T} \right)^{3/2} e^{-W/k_B T} \quad (3.20)$$

with the Boltzmann constant k_B .

However, experiments on the specific heat of metals suggest that only a fraction of about 1/100 of electrons contribute to electronic transport. The discrepancy can be explained by the Fermi-exclusion principle. Because electrons are fermions, any unique state can only be occupied by a single particle. Consequently charge carriers in a solid follow the Fermi-Dirac-distribution

$$f(W) = \frac{1}{e^{(W-\mu)/k_B T} + 1} \quad (3.21)$$

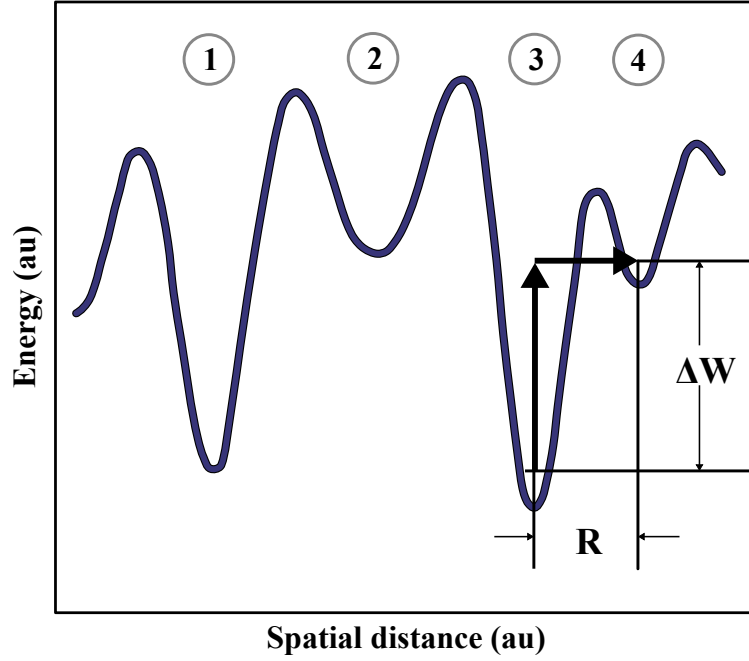


Figure 3.3: Exemplary energy diagram with potential wells at positions 1-4. R and ΔW mark the spatial and energy separation between states 3 and 4. Adapted from [7].

With the chemical potential μ . A comparison between both distribution functions is given in Figure 3.2.

While the Fermi-principle severely limits the number of states that contribute to charge transport, it prevents an accumulation of charge carriers in low-energy states. Therefore, while the charge carrier number is significantly limited, the mean velocity of charge transport is elevated compared to the classical picture. In the description of the electrical conductivity both effects cancel out, which is why the Drude-model yields a reasonably accurate result.

3.2 Hopping Conduction

Section 3.1 describes the electrical transport in metals and crystalline semiconductors, i.e. in a perfect periodic potential landscape. Here, charge carriers can be described as free particles, the mobility of which is limited by scattering. The prerequisite for this conduction mechanism is an abundance of accessible, suitable states. However, if the available states exhibit a sufficiently broad distribution in energy and are separated spatially, the charge carriers are partially localized. They move by hopping between potential wells in a complex energy landscape, an example of which is given in Figure 3.3. Consequently, the main limiting factor of the electrical conductivity is the transition probability p between individual states. When direct excitation over the barrier can be neglected, it is given by

3.2 Hopping Conduction

a combination of the tunneling probability between potential wells and a Boltzmann term dependent on the energy separation between the two states [3]

$$\sigma \propto p \propto e^{-\alpha r_{ij}} e^{-(W_j - W_i)/k_B T} \quad (3.22)$$

where α expresses the localization of the wave-function, r_{ij} is the separation between the two states, k_B is the Boltzmann constant and W_i and W_j are the energies of the initial and resulting state, respectively.

At intermediate temperatures, charge carriers are less constraint by the energy requirement, such that the first term dominates and the transition typically occurs between neighboring atoms. In this case the hopping distance can be assumed to coincide with the nearest neighbor distance R_{NN} . Therefore, the hopping probability becomes constant and the temperature dependence is given by the Boltzmann-term [90]

$$\sigma \propto e^{-\alpha R_{NN}} e^{-(W_j - W_i)/k_B T} \quad (3.23)$$

$$\propto c \cdot e^{-(W_j - W_i)/k_B T} \quad (3.24)$$

This regime is called the nearest neighbor hopping (NNH) regime and causes a characteristic Arrhenius-like electrical conductivity.

However, at lower temperatures the energy separation becomes a significantly limiting factor and the transition probability results from a trade-off between spatial and energy separation. In the exemplary energy landscape in Figure 3.3, this could result in a transition from the energetically close states 3 to 1 rather than to neighboring states. In this so called variable range hopping regime the hopping distance is not constant but depends on the available thermal energy and the energy distribution of states. Here, an important measure is the number of available states for a given hopping distance R and hopping energy $W_j - W_i$ [7]

$$N(R, W_j - W_i) = \frac{4}{3} \pi R^3 D(W_F) (W_j - W_i) \quad (3.25)$$

with the density of states at the Fermi-level $D(W_F)$.

Because there has to be at least one free state available, this sets a minimum energy for the energy window $W_j - W_i$

$$\Rightarrow \begin{aligned} W_j - W_i &> \frac{3}{4\pi R^3 D(W_F)} \\ W_i &< W_{max} = W_j - \frac{3}{4\pi R^3 D(W_F)} \end{aligned} \quad (3.26)$$

Which means for the electrical conductivity as a whole

$$\sigma \propto e^{-\alpha R} \int_{-\infty}^{W_{max}} e^{-(W_j - W)/k_B T} dW \quad (3.27)$$

$$\propto e^{-\alpha R} e^{-3/(4R^3 D(W_F) k_B T)} \quad (3.28)$$

3 Electronic Transport

From this equation the characteristic hopping distance can be inferred by determining the distance R that maximizes the transition probability

$$\begin{aligned} 0 &= \frac{d}{dR} \left[\alpha R + \frac{3}{r\pi R^3 D(W_F) k_B T} \right] \\ \Rightarrow R_m &= \left[\frac{9}{4\pi\alpha D(W_F) k_B T} \right]^{1/4}. \end{aligned} \quad (3.29)$$

Inserted back into equation 3.28 this dominating hopping distance yields the overall electrical conductivity [91, 92]

$$\sigma \propto e^{-\left(\frac{T_0}{T}\right)^{1/4}} \quad (3.30)$$

with

$$T_0 = \frac{(4\alpha)^3}{9\pi D(W_F) k_B}. \quad (3.31)$$

Equation 3.30 reveals the $\log(\sigma) \propto T^{-1/4}$ behavior that is typical for the variable range hopping mechanism.

4 Experimental Techniques

4.1 Magnetron Sputter Deposition

Magnetron sputter deposition is a physical vapor deposition technique (PVD), which relies on the vaporization of a material via collision with charged particles. It is used to grow stoichiometric thin films, mainly from metals or alloys of metals. Compared to other PVD-techniques, magnetron sputtering exhibits relatively high deposition rates and uniform deposition characteristics [93]. To vaporize a material in a magnetron sputter process, ions are accelerated from a plasma to collide with a target material's surface, eroding it in the process. The eroded material is effectively atomized, ejected from the target and can be used for controlled crystal growth, on an appropriate substrate. Figure 4.1 shows a typical DC magnetron sputter setup, where a DC current is used to sustain a plasma and accelerate ions. A vessel is held at a specific pressure by introducing a working medium, usually argon or another noble gas. An electric field is applied, with the vessel acting as the anode and a target disc as the cathode. The target consists of the deposition material, which is cleaned and polished in preparation. Electrons and working gas ions are accelerated in the electric field and, surpassing a critical field threshold, form a self-sustaining

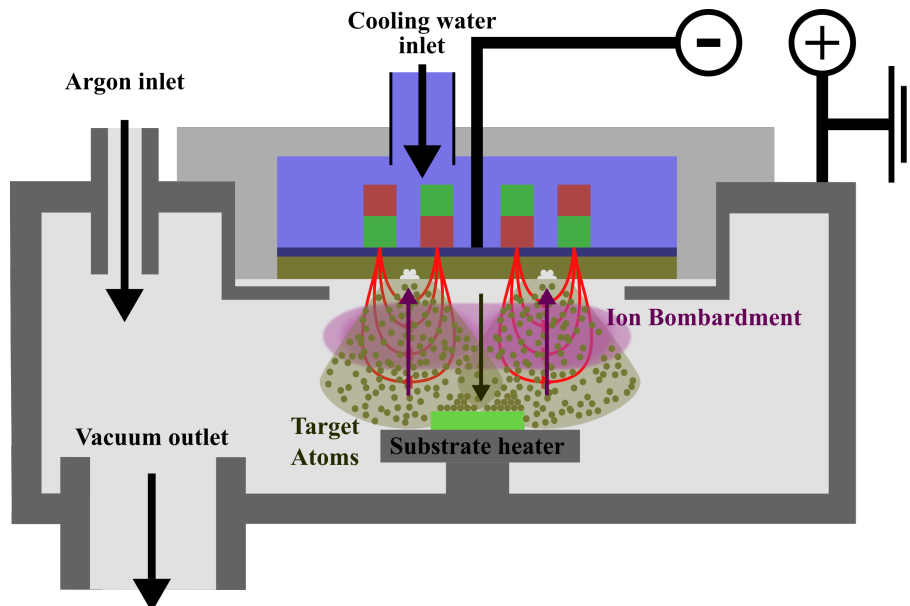


Figure 4.1: Schematic drawing of a DC sputter chamber with argon as the working gas.

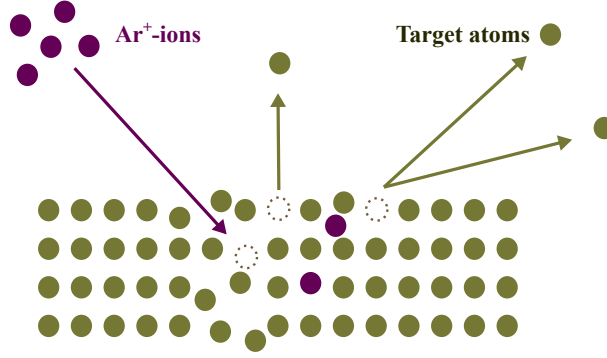


Figure 4.2: Illustration of the impact of working gas ions on the target surface. Adapted from [95]

glow-discharge via collision cascades. The necessary electrical field is lowered by a magnetic field close to the target surface, bending electron trajectories on a circular path, effectively increasing travel time and therefore collision probability. From the plasma, a constant flow of working medium ions is accelerated, bombarding the target surface. As illustrated in Figure 4.1b, each impacting ion leads to a series of collisions, ultimately ejecting atoms from the target. The ejected atoms spread through the vessel volume in a characteristic plume geometry, which can be described as [94]

$$f(\theta) = \cos^n(\theta) \quad (4.1)$$

with $1 \leq n \leq 2$, or in other cases [94]

$$f(\theta) = A \cos^n(\theta) - B \cos^m(\theta) \quad (4.2)$$

where θ is the sputter angle relative to the surface normal and A , B , n and m depend on the material and target preparation. Each atom in the plume is subject to more or less frequent scattering with atoms of the working medium, depending on the process pressure. These scattering events influence the energy of the sputtered atoms and their angular spread. The substrate located opposite of the target exhibits a flow of target atoms reaching its surface. The mobility of the adatoms that adsorb onto the surface, depend on their initial kinetic energy and the energy of the host lattice, quantified by the substrate temperature. The substrate temperature can be used to tune atom mobility and to navigate different morphological thin film regimes. Figure 4.3 shows examples of different growth modes, categorized by their growth temperature according to the 3-zone model [96]. In this framework, three cases are distinguished, with an additional transition state between case 1 and 2 [97].

Zone 1: This regime corresponds to a substrate temperature that is typically 30% or less of the target material melting point. This zone is characterized by low diffusion and low mobility of atoms adsorbing at the surface. The film morphology is porous, as mainly small, elongated grains

4.1 Magnetron Sputter Deposition

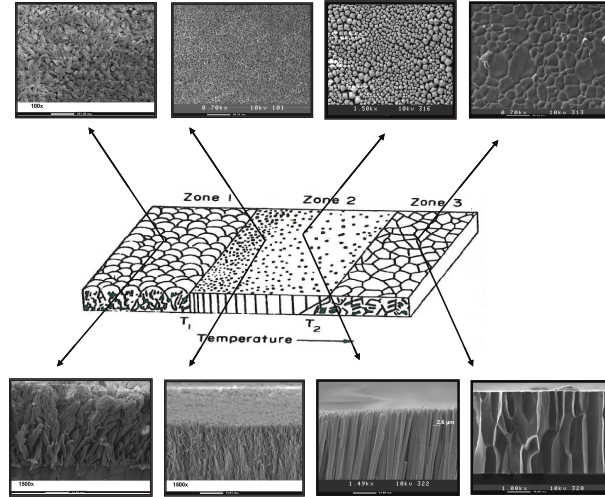


Figure 4.3: Illustration of different growth modes according to the three zone model, with an additional transitional state between zone 1 and 2. The sketch in the center is augmented by 4 top-view electron microscope images (top) and four cross sectional electron microscopy images.

Reprinted from Physics Procedia, 37, Hamid Sabet, Harish B. Bhandari, Haris Kudrolli, Vivek V. Nagarkar, *Fabrication of X-ray/Gamma-ray Detector by Growth of Microcolumnar CSI:Tl onto Silicon Photomultipliers*, 1523-1530, 2012, with permission from Elsevier.

form. These grains are weakly interconnected because of the low mobility and shadowing effects, which inhibit deposition in the gaps between grains. The surface is relatively rough, as it is formed by tips of columnar grains. The film volume as a whole is porous and exhibits a lower density than corresponding bulk materials. Due to the lack of bulk-diffusion and limited surface diffusion, the crystalline structure is mostly amorphous.

Transit. Zone: The transitional zone is also dominated by amorphous columnar grains, which increasingly grow laterally. As individual grains merge, the film gets denser and the surface gets more smooth. However, surface and bulk-like diffusion are still suppressed, leading to low crystallinity.

Zone 2: At temperatures of approximately 50-70% of the melting temperature, surface diffusion begins to significantly increase crystallinity. As a result, grains are highly oriented along the crystallographic orientations dictated by the substrate and growth conditions. The film properties converge with the bulk properties, mainly due to increased density compared to low temperature regimes.

Zone 3: Bulk-like and surface diffusion dominate the film growth process

4 Experimental Techniques

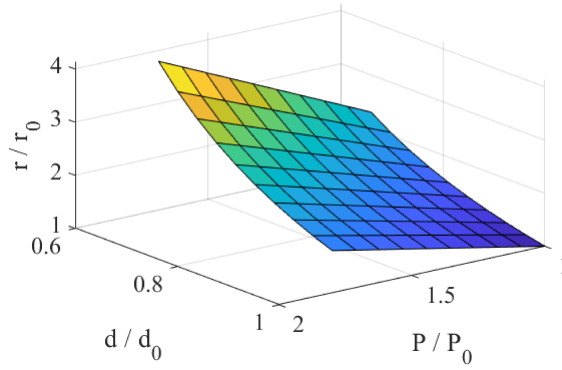


Figure 4.4: Dependence of the sputter rate on the substrate-target distance and the sputter power.

widely. As a result, highly crystalline internal structures form and the misalignment of individual grains further diminishes.

While the 3-zone model captures common trends in thin film growth, it omits important process parameters. Especially the pressure during deposition becomes important in the transition between zone 1 and zone 2. A high sputter pressure leads to more working gas atoms being adsorbed onto the substrate surface, particularly at low temperatures [98]. These adsorbed gas atoms interfere with film growth as they limit surface mobility of sputtered atoms. Additionally, a high pressure promotes collision of sputtered atoms on their trajectory to the substrate, dissipating their energy partly and thus limiting their mobility.

In contrast to the clear relationships presented above, practical applications of real materials can pose conflicting requirements that have to be addressed individually. While, for example, high crystalline quality usually requires elevated deposition temperatures, optimum surface smoothness is commonly reached in the transition region between zone 1 and zone 2. Also, materials frequently exhibit different growth modes, in which different crystal orientations and morphologies are favored, depending on deposition conditions.

Among additional important parameters, the target-substrate distance d and sputter power P determine the deposition rate r . The sputter power is the electrical power that is supplied to sustain the glow discharge. It controls the intensity of the ion bombardment, with a high power resulting in more ion collision per unit time. Thus it controls the flow of sputtered atoms, leading to a linear relationship with the sputter rate, $r \propto P$ [95]. The distance of substrate and target determines the area this flow of atoms is distributed on, which is proportional to the half-sphere area A around the target, $A \propto d^2$ [95]. Relative to a reference value, r_0 , with known sputter power and pressure the sputter rate is thus approximately given by

$$\frac{r}{r_0} = P/P_0 \frac{1}{(d/d_0)^2}, \quad (4.3)$$

which is illustrated in Figure 4.4.

Especially for the fabrication of nanostructures, this sputter rate is fine-tuned to control structure sizes.

4.2 Thermal Conductivity Measurements of Thin Films

The thermal properties of superlattice systems are especially interesting in the cross-plane direction, which is highly interface dominated. However, as superlattice systems are thin film based, they rarely exceed $1\ \mu\text{m}$ in total thickness. When measuring the thermal conductivity of a film of this size, the absolute temperature differences are challengingly small. Following the Fourier law

$$\vec{j}_q = -\kappa \Delta T, \quad (4.4)$$

assuming a high thermal flux of $1\ \text{W}/\text{mm}^2$ the temperature difference for amorphous SiO_2 is only $1\ \text{K}$ across a $1\ \mu\text{m}$ thick film. In HfNiSn and TiNiSn , with a significantly higher thermal conductivity, the temperature drop would amount only to a fraction of $1\ \text{K}$.

Therefore techniques have been developed, which rely on the rate of heat dissipation of small-scale structures on thin films. A high thermal conductivity material transports an applied heating power more efficiently away from a heat source, which leads to a smaller temperature response. In the transient heat wire method [99], for example, an extended wire in contact with a medium is heated by a step current and the thermal conductivity is inferred from the temperature response. In thin films, a modification of this technique is most commonly used, in which an alternating current replaces the step current. Because the thermal conductivity is determined from analyzing higher harmonics with a frequency three times the source frequency ω , this method is called the 3ω -technique [100, 101].

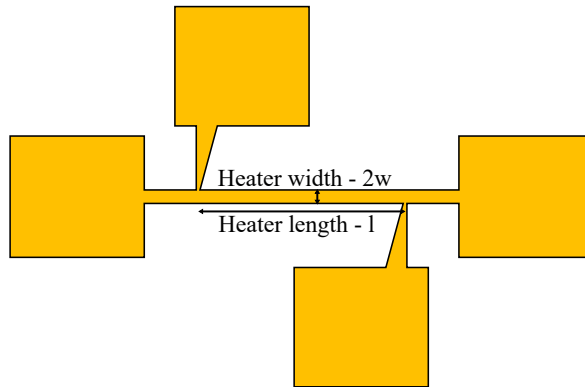


Figure 4.5: Sketch of a typical 3ω -measurement structure.

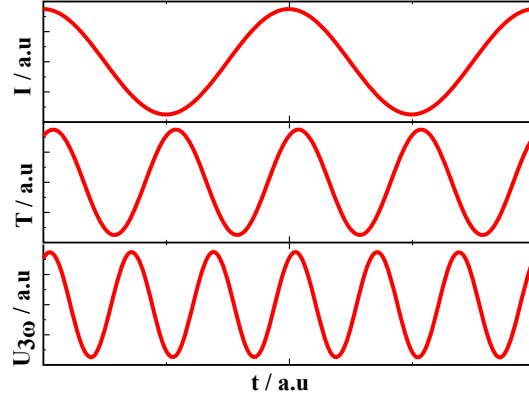


Figure 4.6: Illustration of the heating current, the heater temperature and component of the heater voltage drop with an 3ω -characteristic.

The 3ω -technique

In the 3ω technique, a wire on a thin film sample acts both as a heater and a temperature sensor. For this purpose, a geometry similar to the one illustrated in Figure 4.5 is used, making the temperature dependent heater resistance accessible by a 4-point resistance measurement. Subsequently, knowing the temperature characteristics of the wire, $\alpha = dR/dT$, makes the local temperature accessible at every point in time. At the same time, a current applied to the heater leads to heating of the wire and the sample volume underneath it. For an alternating current with an amplitude I_0 and a frequency ω

$$I(t) = I_0 \sin(\omega t) \quad (4.5)$$

this current exerts a heating power with double the source frequency

$$P(t) = I(t)^2 \cdot R = \frac{1}{2} I_0^2 R [1 - \sin(2\omega t)]. \quad (4.6)$$

The oscillating heating power leads to a temperature fluctuation \hat{T} with a characteristic phase shift ϕ , as depicted in Figure 4.6. Because the resistance depends on the temperature via a material specific temperature coefficient $\alpha = \frac{dR}{dT}$, the resistance follows the temperature oscillation:

$$R(t) = R_0 [1 + \alpha \hat{T} \cos(2\omega t + \phi)]. \quad (4.7)$$

When this oscillating resistance is combined with the source current, equation 4.5, an additional 3ω contribution results:

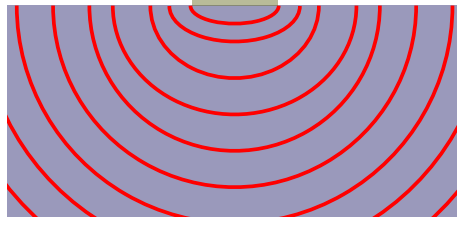


Figure 4.7: Heat dissipating from a narrow heater into a homogeneous medium. The temperature profile becomes increasingly radially symmetrical with distance from the heat source, as the finite heater width plays an increasingly smaller role.

$$V(t) = R(t) \cdot I(t) \quad (4.8)$$

$$= R_0 I_0 [1 + \alpha \hat{T} \cos(2\omega t + \phi)] \sin(\omega t) \quad (4.9)$$

$$= V_0 \sin(\omega t) + \frac{1}{2} V_0 \alpha \hat{T} [\sin(3\omega t + \phi) - \sin(\omega t - \phi)] \quad (4.10)$$

with $V_0 = R_0 \cdot I_0$ and $\sin(x)\cos(y) = \frac{1}{2}(\sin(x+y) + \sin(x-y))$.

Assuming $\frac{1}{2}\alpha\hat{T} \ll 1$ and consequently neglecting the 1ω -contribution of the second term, the comparison of the harmonics of the voltage drop yields

$$\frac{2V_{3\omega}}{\alpha V_0} \approx \frac{2V_{3\omega}}{\alpha V_0} = \hat{T} \quad (4.11)$$

These temperature fluctuations are the basis to calculate the thermal conductivity using a system-specific model of thermal transport. While the temperature oscillations cannot easily be linked to the thermal conductivity in a general case, if the prerequisites given in Table 4.1 are fulfilled, it can be described by a simplified model. In this case the heat flow is approximately radially symmetrical, as depicted in Figure 4.7. Carslaw and Jaeger [106] give a solution of the heat diffusion equation for this case,

$$\hat{T} = \frac{P}{\pi l \kappa} \left[-\frac{1}{2} \ln(2\omega) + \frac{1}{2} \ln\left(\frac{D}{r^2}\right) + \text{Const.} \right], \quad (4.12)$$

in a distance r from the line-source, with the thermal diffusivity D , the applied electrical power per unit length P/l and a complex constant.

For a heater with a finite width $2w$ this becomes [106]

$$\hat{T} = \frac{P}{\pi l \kappa} \left[-\frac{1}{2} \ln(2\omega) + \frac{1}{2} \ln\left(\frac{\kappa}{Cw^2}\right) + \text{Const.}' \right], \quad (4.13)$$

with the heat capacity C .

4 Experimental Techniques

Approximation	Criterion	Error	This study	References
Substrate is isothermal ($\kappa_S \rightarrow \infty$)	$(\kappa/\kappa_S)^2 < 10^{-2}$	$\approx 1\%$	$(\kappa/\kappa_S)^2 = 3.6 \cdot 10^{-3} - 4 \cdot 10^{-4}$	[102]
Film heat flow is quasi-static ($C \rightarrow 0$)	$\lambda/d > 5.7$	$< 1\%$	$\lambda_{TiNiSn}/d \approx 42.4,$ $\lambda_{HfNiSn}/d \approx 31.6$	[103]
Substrate is semi-infinite ($d_S \rightarrow \infty$)	$d_S/\lambda_S > 2$	-	$d_S/\lambda_S = 3.73$	[104]
Heat flow is 1D in the thin film	$d/w \ll 1$	-	$d/w = 0.1$	[105]
Heater acts as line source ($w \rightarrow 0$)	$\lambda_S/w > 5$	$< 1\%$	$\lambda_S/w = 13.4$	[102]
Heater is infinitely long ($l \rightarrow \infty$)	$l/\lambda_S > 4.7$	$< 1\%$	$l/\lambda_S = 7.5$	[104]
Heater is massless ($C_H d_H \rightarrow 0$)	$d_H/d \ll 1$	-	$d_H/d \approx 0.1$	[104, 103]

Table 4.1: Approximations relevant for the differential 3ω -method and related errors. Where no explicit error is stated, the criteria correspond to best practices. κ and κ_S are the film thermal conductivity and substrate thermal conductivity, respectively. d and d_s are film and substrate thicknesses, respectively. The heater geometry is given by w , the heater half-width, and l , the heater length. C and C_H are the heat capacity of film and heater, respectively, where the film heat capacity is calculated by the Dulong-Petit law. $\lambda = \sqrt{D/\omega}$ and $\lambda_S = \sqrt{D_S/\omega}$ are the thermal penetration depths evaluated at an exemplary source frequency of 1000 Hz with the thermal diffusivity D of the film and substrate, respectively. Based on [105].

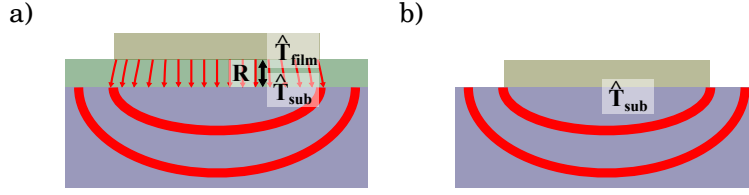


Figure 4.8: Illustration of the heat spread in homogeneous sample and a sample with an additional thin film.

a) The heat moves quasi 1-dimensionally through the thin film, and spreads through the homogeneous substrate radially. The temperature fluctuations on top of the substrate \hat{T}_{sub} correspond to \hat{T}_{film} attenuated by the additional film thermal resistance R .

b) A reference sample of a bare substrate.

This means that the the thermal conductivity can be inferred from the slope of $\Delta T(\ln \omega)$ by

$$\kappa = -\frac{1}{2} \frac{P}{\pi l} \left[\frac{d\hat{T}}{d \ln(2\omega)} \right]^{-1} \quad (4.14)$$

and thus with equation 4.11:

$$\kappa \approx -\frac{1}{2} \frac{P}{\pi l} \left[\frac{d}{d \ln \omega} \left(\frac{2V_{3\omega}}{\alpha V_{\omega}} \right) \right]^{-1} \quad (4.15)$$

This approach is appropriate for any sample that is larger than the effective penetration depth of the temperature oscillations. However, in thin films this prerequisite is not easily fulfilled. The heat flow is more likely to resemble the illustration in Figure 4.8a, passing through the thin film quasi 1-dimensionally and spreading radially in the substrate [107]. In this case, the analysis above can be applied with the thin film giving a constant thermal resistance contribution. Using the differential 3-omega method, this additional thermal resistance can be inferred by comparing a thin film sample on a substrate and the signal of a blank substrate. As depicted in Figure 4.8, the temperature fluctuations on the film surface \hat{T}_{film} differ from the fluctuations on the substrate surface \hat{T}_{sub} , because the bottom side fluctuations are attenuated by the thermal film resistance. The measurement of the first sample reveals \hat{T}_{film} , while the measurement on the reference bare substrate sample effectively yields \hat{T}_{sub} . The difference between the temperature oscillations $\Delta T = \hat{T}_{film} - \hat{T}_{sub}$ corresponds to the temperature difference between top and bottom side of the film, caused by the heat current $j_q = P/2\omega l$. Therefore the thermal conductivity can be inferred by Fourier's law:

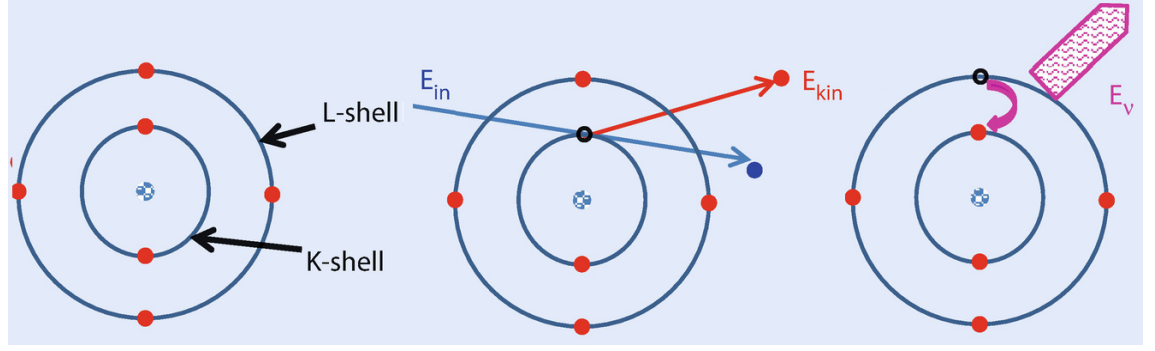


Figure 4.9: Basic process underlying energy dispersive X-ray spectroscopy (EDX). The collision with an external electron leads to the ejection of an electron from the inner K-shell. A transition from an outer shell subsequently leads to the emission of a X-ray photon with an energy characteristic of the element.

Adapted with permission from Springer Nature Customer Service Centre GmbH: Springer Nature Scanning Electron Microscopy and X-Ray Microanalysis by Joseph I. Goldstein; Dale E. Newbury; Joseph R. Michael; Nicholas W. M. Ritchie; John Henry, J. Scott; David C. Joy (2018)

$$j_q = -\kappa \left(-\frac{\hat{T}_{film} - \hat{T}_{sub}}{d} \right) \quad (4.16)$$

$$(4.17)$$

$$\kappa = \frac{1}{2} \frac{P}{wl} \frac{d}{\hat{T}_{film} - \hat{T}_{sub}} \quad (4.18)$$

with the film thickness d .

Similarly, any auxiliary layers, like buffer layers, can be added to the reference sample, so their contribution can be subtracted from the overall thermal conductivity.

4.3 Energy Dispersive X-ray Spectroscopy

The monitoring of the elemental composition is a key requirement for the magnetron sputter deposition from multi-component targets. The composition of the target and realized thin film can differ significantly depending on sputter parameters, target preparation and material. This is caused by resputtering effects [108], the element-specific spatial distribution in the sputter plume [94] and different sticking coefficient for the deposited elements on the specific substrate [109]. Additionally, phase separation potentially leads to sample inhomogeneity and therefore locally varying composition [110].

For the necessary elemental analysis, energy dispersive X-ray spectroscopy (EDX) can be used, which reveals the composition of a surface layer of specific thickness. It is based

4.3 Energy Dispersive X-ray Spectroscopy

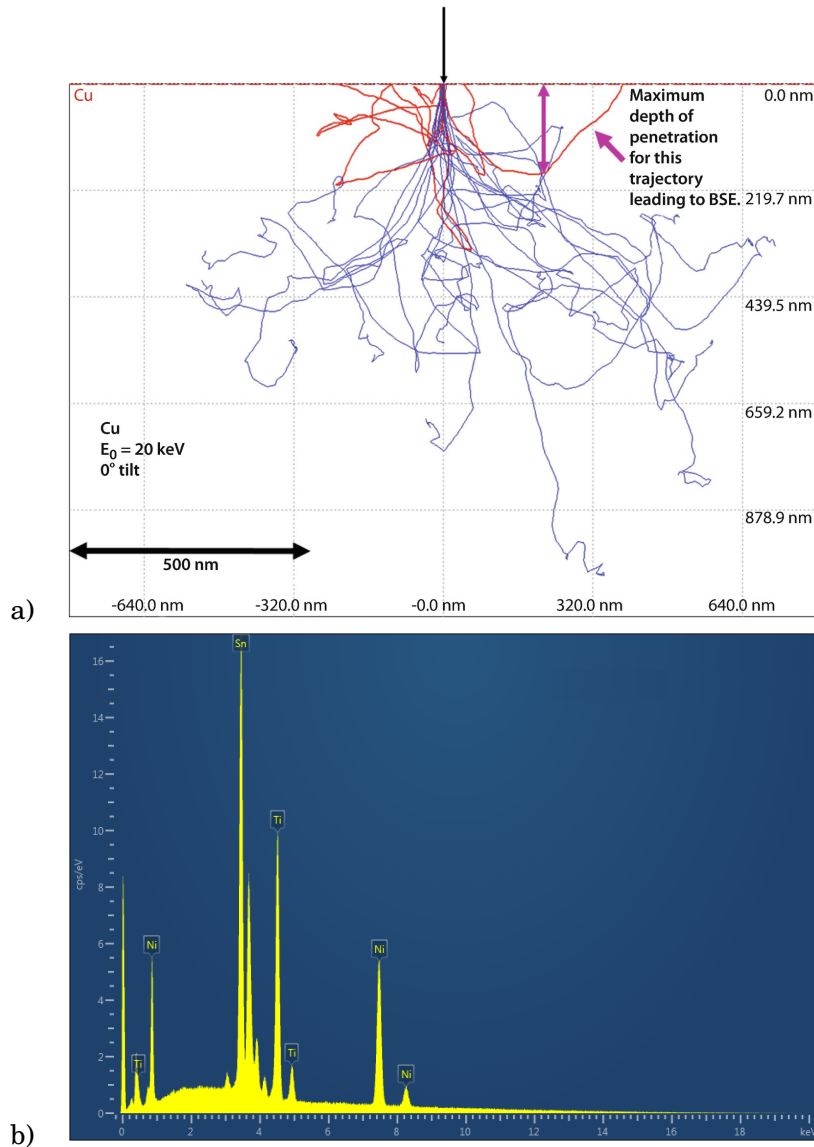


Figure 4.10: Illustration of electron energy absorption and resulting X-ray spectrum.

a) Trajectories of 20 keV electrons incident on a copper surface. Red lines correspond to backscattered electrons that are re-emitted from the surface. The trajectories represented by blue lines correspond to electrons that have all their energy absorbed in the material. Part of the energy leads to inner-shell transitions that cause the subsequent emission of characteristic X-ray radiation.

Reprinted by permission from Springer Nature Customer Service Centre GmbH: Springer Nature Scanning Electron Microscopy and X-Ray Microanalysis by Joseph I. Goldstein; Dale E. Newbury; Joseph R. Michael; Nicholas W. M. Ritchie; John Henry, J. Scott; David C. Joy (2018)

b) X-ray spectrum caused by a 20 keV electron beam on a TiNiSn surface. The peaks corresponding to characteristic inner-shell transition levels are marked with their corresponding element.

4 Experimental Techniques

on the electron beam-induced X-ray fluorescence, which leads to a highly element specific radiation spectrum. A typical measurement procedure is illustrated in Figure 4.10a. Electrons are accelerated and enter the sample volume depositing their energy. While some of the electrons are scattered backwards, subsequently being reemitted from the surface, most electrons lose all their kinetic energy within a characteristic penetration depth. This penetration depth varies depending on the sample material and on the initial electron energy between few hundreds of nm and few μm . Incident electrons are decelerated by the Coloumb interaction with the outer shell of the sample-atoms, leading to a continuous X-ray bremsstrahlung background. However, for high energy incident electrons, inelastic collisions with inner-shell electrons represents another route of energy dissipation, an example of which is shown in Figure 4.9. The incoming electron leads to the ejection of a K-shell electron, leaving behind an unoccupied low-energy state. This free state can be filled with different higher-energy electrons, leading to the emission of X-ray photons of element-specific characteristic energies. The process illustrated in Figure 4.9 corresponds to a common emission process, a transition from the L- to the K-shell, which leads to chracteristic K_α -radiation. The second lowest energy photons related to K-shell processes, corresponding to K_β radiation, are emitted by electrons from the third shell. Analogously, L_α , L_β -radiation correspond to the lowest energy photons for a process involving an L-shell vacancy.

As the transition energies are element-specific, the position of emission lines in the X-ray spectra yield qualitative understanding of the elemental composition. For a quantitative analysis, the intensity of emission lines are compared with a simulated value. However, in this case the absorption characteristic of both the incident electrons as well as the emitted X-rays have to be considered. In practice this is further complicated by the fact that both quantities depend on the sample geometry, requiring sufficiently smooth, defined surfaces and minimum thicknesses of typically several hundred nm.

4.4 X-Ray Diffraction

X-ray radiation forms part of the electromagnetic spectrum with wavelength between 0.1-10 nm. As this wavelength range corresponds to the typical atomic spacing in crystals, it is especially useful for structural analysis. For this purpose, the intensity of radiation scattered by the sample material is recorded for different incidence and scatter angles. The resulting interference pattern is sensitive to the atomic plane spacing, the unit cell arrangement and, to a lesser degree, to the atomic species. These aspects lead to a subset of angles at which characteristic maxima in the scattered intensity can be observed. These angles are given by Bragg's law [111]

$$n\lambda = 2d \sin \theta, \quad (4.19)$$

where λ is the wavelength, d is the atomic plane spacing, θ is the half-angle between incident and scattered beam and n is the diffraction order, $n = 1, 2, 3, \dots$. This law expresses the constructive interference condition of a X-ray beam with wavelength λ on the sample

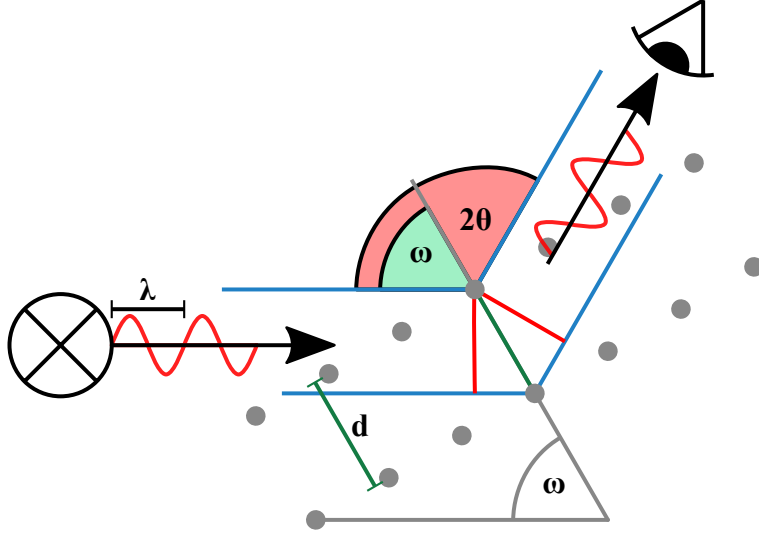


Figure 4.11: Illustration of the Bragg-Brentano geometry. The X-ray source and detector are placed on a common half circle around the sample. To record an interference pattern, the detector-source angle 2θ is scanned, while the sample is simultaneously rotated around its own axis at $\omega = \theta$.

material. For a perfectly ordered infinitely large crystal, destructive interference cancels out the scattered beam intensity in any other direction. For epitaxial thin films the resulting interference patterns are commonly recorded in the Bragg-Brentano geometry illustrated in Figure 4.11. In this configuration the X-ray source and detector are fixed on the same half-circle around the sample. To record an interference pattern, the detector-source angle 2θ is scanned, while the sample is rotated around its axis at $\omega = \theta$. Under these geometrical constraints, incident and scatter angles remain equal, while different diffraction conditions are realized.

With the recorded interference patterns, the lattice constant, the crystal structure and the unit cell configuration of crystalline materials can be routinely determined. Additional to this, information about the crystallinity, alignment uniformity, and the overall crystal quality can be gained from the deviation of reflexes from the ideal point-like shape. While the broadening of XRD-reflexes can have several causes, in a multi-crystalline material, it is dominated by the finite diffraction volume of the crystal grains. In this case the individual crystallite size can be estimated from the Scherrer equation [112]

$$L = K \frac{\lambda}{\Delta(2\theta_D) \cos(\theta_D)} \quad (4.20)$$

with the crystallite size L , the wavelength λ , the diffraction reflex width $\Delta\theta_D$ at the diffraction angle θ_D . The Scherrer factor expresses the geometrical shape of the crystallites with $K = 0.94$ corresponding to spheres [113]. Additional to the crystallite size, the degree of misalignment of individual grains can be determined via the diffraction reflex

4 Experimental Techniques

rocking curve. It is recorded by fixing the detector position on a specific diffraction angle θ_D and varying the sample orientation, $\omega = \theta_D \pm x$. For an ideal crystal, the interference condition is only met at $\omega = \theta_D$. However, in a multicrystalline material the individual crystallites are typically misaligned with respect to the main axis following a normal distribution. This distribution is recorded by the rocking curve and its width indicates the degree of misalignment in a multicrystalline material [114].

Superlattices

In superlattices the diffraction pattern is additionally influenced by the periodicity of the layer structure. The periodic sequence gives rise to additional reflexes around the main film diffraction angles. The spacing of these additional, satellite reflexes, is given by the superlattice period length δ via [115]

$$2 \frac{\sin(\theta)}{\lambda} = \frac{1}{d} \pm \frac{m}{\delta}, \quad (4.21)$$

where $m = 1, 2, 3, \dots$ is the satellite order.

Here, the intensity and number of distinguishable orders depends critically on the regularity of the superlattice structure. Random fluctuations of the individual layer thickness lead to partial or full suppression of satellite pattern formation. Therefore, both the period length and indications of the interface quality can be inferred from superlattice satellites.

5 P-type thin film $\text{Hf}_{0.5}\text{Zr}_{0.5}\text{CoSb}_{1-x}\text{Sn}_x$

5.1 Introduction

Current commercially available thermoelectric materials are based on rare or toxic substances such as tellurium, lead and Bismuth. Half Heusler compounds constitute a viable alternative, potentially employing earth abundant, non-toxic elements and reaching similar efficiencies [17].

As a promising candidate, n-type $(\text{Ti}, \text{Zr}, \text{Hf})\text{NiSn}$ has been well established both in bulk [47] and thin films [116]. Members of this family have demonstrated peak ZT -values of around 1.5 at 700 °C [117]. However, for efficient thermoelectric generators, an additional p-type material is necessary. Consequently, the search for this material intensified in the recent years. Among the investigated compounds, the $(\text{Ti}, \text{Zr}, \text{Hf})\text{Co}(\text{Sb}_{1-x}\text{Sn}_x)$ -family stands out with relatively low thermal conductivities combined with a high thermoelectric power factor [118]. These properties can in part be attributed to spontaneous phase separation: The material tends to precipitate into different phases with variations on the $(\text{Ti}, \text{Zr}, \text{Hf})$ and (Sb, Sn) -position (Figure 5.1) [119]. The grain boundaries between the phases give rise to additional phonon scattering, thereby reducing thermal conductivity. Additionally, phase separation was reported to increase both the Seebeck coefficient and electrical conductivity [120].

Thin film thermoelectric generators of $(\text{Ti}, \text{Zr}, \text{Hf})\text{Co}(\text{Sb}_{1-x}\text{Sn}_x)$ in combination with $(\text{Ti}, \text{Zr}, \text{Hf})\text{NiSn}$ could potentially become competitive with currently used BiTe [121]. For rational device fabrication, however, thin film growth of both materials on a common substrate has to be demonstrated [9]. While epitaxial growth of $(\text{Ti}, \text{Zr}, \text{Hf})\text{NiSn}$ on MgO is well documented [116], there is no similar experimental investigation for

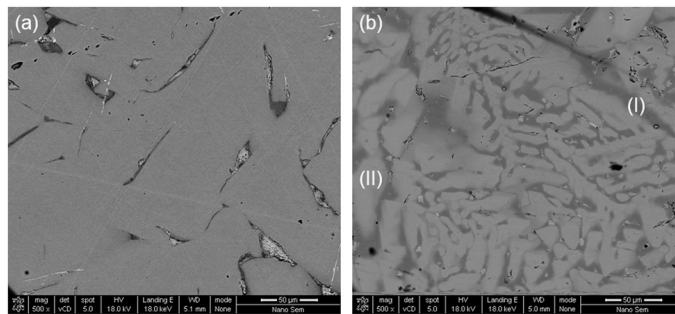


Figure 5.1: Exemplary depiction of phase separation in
a) $\text{Ti}_{0.5}\text{Hf}_{0.5}\text{CoSb}_{0.8}\text{Sn}_{0.2}$ and b) $\text{Ti}_{0.33}\text{Zr}_{0.33}\text{Hf}_{0.33}\text{CoSb}_{0.8}\text{Sn}_{0.2}$.
Image reproduced with consent from [35]

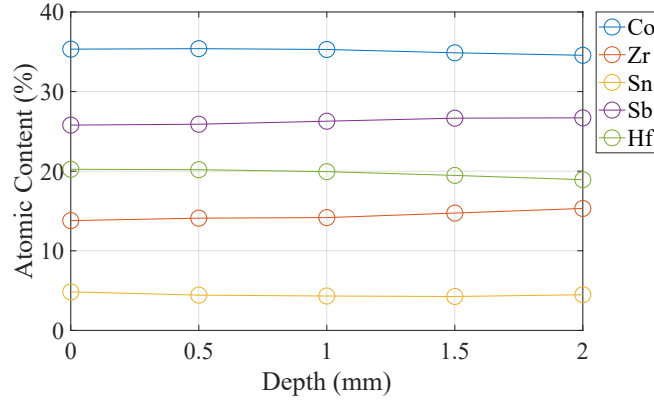


Figure 5.2: Target composition in dependence on the target depth.

(Ti, Zr, Hf)Co(Sb_{1-x}Sn_x).

Of this material family, (Zr_{0.5}Hf_{0.5})Co(Sb_{1-x}Sn_x) exhibits a relatively low tendency for spontaneous phase separation [122]. This makes it ideal for an initial thin film investigation, because it likely shows a less complex intrinsic phase-structure. Thus the central research question of this chapter are:

- Can (Ti, Zr, Hf)Co(Sb_{1-x}Sn_x) grow homogeneously on MgO, despite of its tendency for phase separation?
- How do bulk and thin film samples differ in their properties?

5.2 Sample Preparation

For magnetron sputter deposition, a homogeneous, compact target is necessary [93]. However, the elements constituting (Ti, Zr, Hf)CoSb_{1-x}Sn_x have widely differing melting points, potentially leading to target inhomogeneities. Zr and Hf have a melting point of 1855 °C and 2233 °C while Sn and Sb melt at 231 °C and 631 °C, respectively [123]. Additional to the low melting point, Sb exhibits a high vapor pressure in the liquid phase, making it prone to material loss during heating. The differing melting points are accounted for by using spark plasma sintering (SPS). Using SPS, the pre-reacted powder, bought from HMW Hauner GmbH & Co. KG, is only exposed to relatively low temperatures of around 1000 °C. The pulverized base material is compacted with a force of 69 kN at vacuum conditions, while being exposed to pulsed currents that heat the sample according to a preset temperature ramp over 60 minutes.

With this method, the (Zr_{0.5}Hf_{0.5})Co(Sb_{1-x}Sn_x)-powder was formed into compact sputter targets with high compositional depth homogeneity (Figure 5.2). For the homogeneity analysis a FEI Helios NanoLab 600i scanning electron microscope was used, performing energy-dispersive X-ray spectroscopy (EDX) on the edge of a fractured target with 20 kV accelerating voltage. An error of ±0.5% is estimated from a measurement on a related

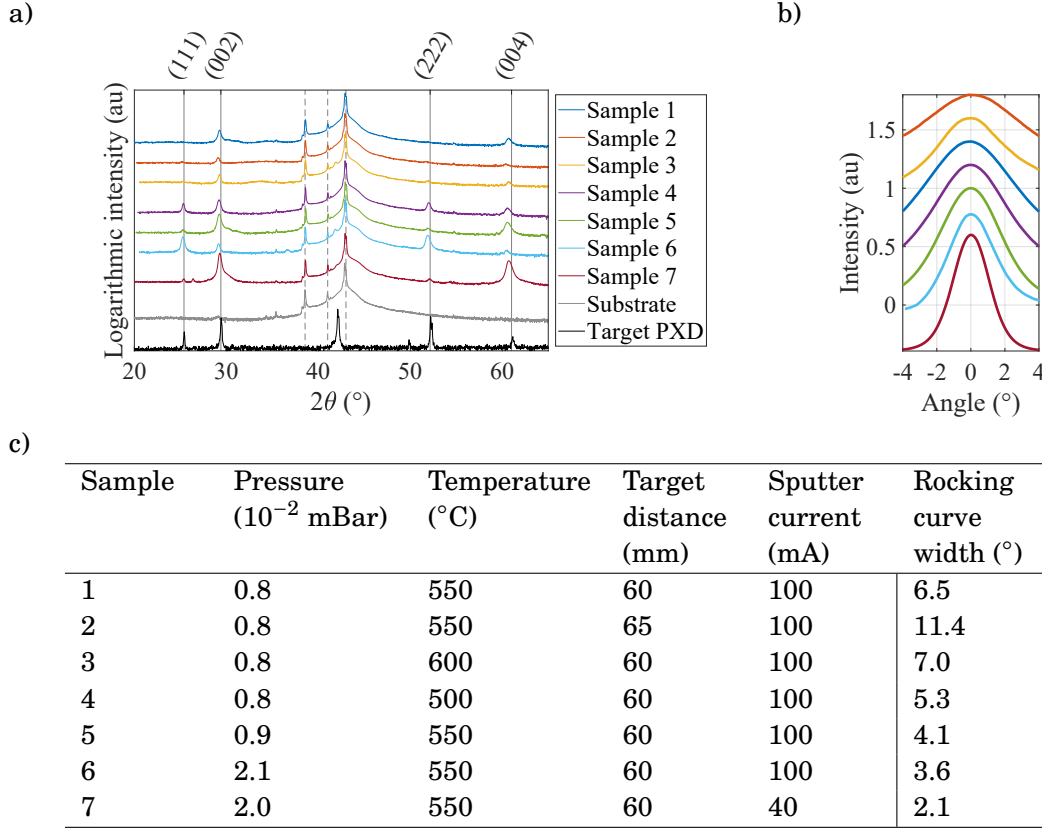


Figure 5.3: Crystalline qualities of $(\text{Zr}_{0.5}\text{Hf}_{0.5})\text{Co}(\text{Sb}_{1-x}\text{Sn}_x)$ thin film samples at selected sputter conditions.

a) XRD Scans with substrate scan and target PXD at the bottom. Film reflexes are marked with solid vertical lines, while substrate peaks are given by broken vertical lines.

b) Rocking curves of samples 1 to 7.

c) Sputter conditions for the displayed samples.

compound, which was verified by mass spectrometry. While the composition shows little variation with target depth, the ratio of Hf to Zr is approximately 42:58 instead of 50:50. However, as Hf and Zr are isoelectronic, the overall (Zr, Hf)-lattice site occupation is crucial, which is with $34.17 \pm 0.5\%$ close to the ideal 33.3%.

On the (Sb, Sn)-site, there is a stronger deficiency with $30.74 \pm 0.5\%$ instead of 33.3%, which is likely caused by material loss due to evaporation during heating. However, the ratio of Sb and Sn is close to the ideal with 14.5:85.5 instead of 15:85.

5.2.1 Optimization of Growth Conditions

The initial parameters for sputter deposition are based on the optimal conditions for the structurally similar TiNiSn [124]. The X-ray diffraction scans, Figure 5.3a, indicate the

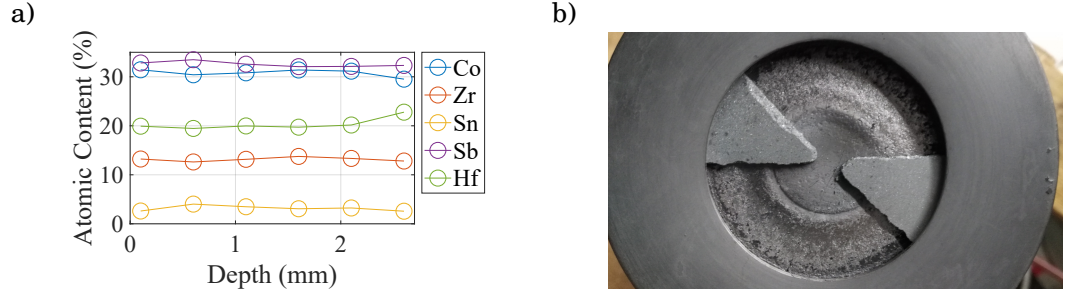


Figure 5.4: a) Composition of the second of the Sb-excess target over target depth. The target shows slightly more variation than the first, but is reasonably homogeneous over its thickness.
b) Target prepared with $\text{Sb}_{0.9}\text{Sn}_{0.1}$ -foil. From the covered part of the target an excess of Sb and Sn is deposited.

crystal structure and crystal orientation for different sputter powers, target-substrate distances, deposition temperatures and gas pressures during deposition. A summary of the used parameters is given in table 5.3c. Additionally, the rocking curves, Figure 5.3b, quantify the amount of tilt of individual grains and therefore the degree of epitaxy. The sample sputtered at TiNiSn-conditions exhibits a rocking curve width of 6.5° and the desired (002) orientation. However the film reflexes are relatively weak, indicating a low degree of crystallinity. Reducing the temperature to 500°C leads to slightly better epitaxy, but also an additional (111)-orientation. Increasing the substrate-target distance, on the other hand, leads to a deterioration of crystal quality, as does increasing the deposition temperature by 50°C . An increased sputter pressure improves crystallinity. An additionally lowered sputter current to 40 mA, leads to an even narrower rocking curve and a strongly selective (100)-growth.

5.2.2 Composition Variation

As the thin films lack antimony, over-stoichiometric addition of Sb is necessary. The reason for the deficiency is twofold: During target fabrication the volatile Sb tends to evaporate [35] and both Sb and Sn have a lower sticking coefficient as Co, Zr and Hf, which leads to a decreased deposition.

However, in a target with additional Sb, the excess tends to evaporate, leaving only a modest surplus (Table 5.1). The homogeneity in the excess Sb Target is reasonable, although there is slightly more variation (Figure 5.4), which could be caused by precipitating Sn.

With the surplus-target, the thin films increase in Sb-content from 23.36% to 26.1%, with the ideal being 28.33%. Additionally, the relative Co-excess of previous samples, which was caused by the lower Sb-content, is significantly reduced with $c_{\text{Co}} = 36.7\%$ instead of 38.8%. To compensate the remaining gap in Sb-content, a $\text{Sb}_{0.9}\text{Sn}_{0.1}$ -foil was used to partly cover the target (Figure 5.4). From the covered parts of the target excess Sb and

Co	Sn+Sb	Zr+Hf	Sn	Sb	Hf	Zr	S ($\mu\text{V/K}$)
Ideal							
33.33	33.33	33.33	5.00	28.33	16.67	16.67	-
PHH2 + SbSn-Foil							
Sputter power: 10-12 W							
34.55	32.80	32.65	1.68	31.12	17.87	14.78	-2.87
33.96	33.13	32.91	2.99	30.14	17.68	15.23	-11.01
Bulk							
$\text{Ti}_{0.33}\text{Zr}_{0.33}\text{Hf}_{0.33}\text{CoSb}_{0.8}\text{Sn}_{0.2}$							
33.3	33.3	-	6.67	26.7	-	-	153.15
Bulk							
$\text{Zr}_{0.5}\text{Hf}_{0.5}\text{CoSb}_{0.8}\text{Sn}_{0.2}$							
33.3	33.3	33.3	6.67	26.7	16.67	16.67	120.6
PHH2 + SbSn-Foil							
Sputter power: 25-28 W							
31.41	34.20	34.40	3.79	30.405	19.61	14.78	17.3
31.33	34.54	34.13	2.62	31.92	19.13	15	9.22
30.96	33.32	35.71	1.82	31.5	20.14	15.57	6.11
25.53	45.80	28.67	3.33	42.46	16.68	11.99	-
PHH2 thin film							
36.67	28.58	34.74	2.48	26.1	18.53	16.21	-
Sb-excess target (PHH2)							
31.10	35.81	33.09	3.36	32.45	19.74	13.35	-
PHH1 thin film							
38.83	27.61	33.56	4.25	23.36	16.3	17.26	-
First target (PHH1)							
35.09	30.74	34.17	4.47	26.27	19.75	14.42	-
Ideal							
33.33	33.33	33.33	5.00	28.33	16.67	16.67	-

Table 5.1: Composition of manufactured samples and targets.

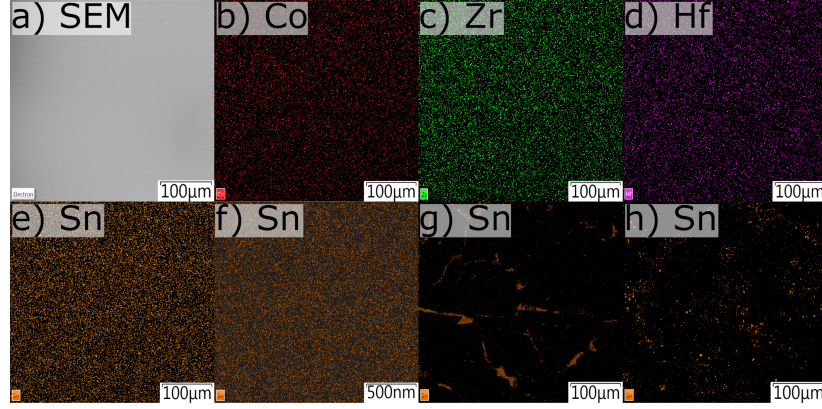


Figure 5.5: Compositional maps of the $\text{Zr}_{0.46}\text{Hf}_{0.53}\text{Co}_{1.02}\text{Sb}_{0.90}\text{Sn}_{0.09}$ thin film sample in comparison with two bulk samples. Image a) shows a SEM-image of the thin film, while images b-f) show the distribution of different constituent elements. Here, f) corresponds to the maximum available magnification of the EDX-system. g) and h) show the Sn-distribution in bulk $\text{Zr}_{0.5}\text{Hf}_{0.5}\text{CoSb}_{0.80}\text{Sn}_{0.2}$ and $\text{Ti}_{0.33}\text{Zr}_{0.33}\text{Hf}_{0.33}\text{CoSb}_{0.80}\text{Sn}_{0.2}$, respectively.

Sn are deposited, balancing the overall composition. The 1-2 mm thick Sb-Sn foil was produced in a cold pressing step, with the ductile tin giving stability to the sheet. While the resulting films now exhibit an overall deficiency in Sn, the filling fraction of the shared (Sb, Sn) atomic position is close to the ideal.

The SbSn-foil coverage controls the filling fraction of the (Sb, Sn)-position. Lowering the sputter power can additionally balance both the filling fraction of the Co and the (Hf, Zr)-position. By varying sputter conditions and foil coverage, a range of different sample compositions has been realized, see table 5.1, with the closest to the ideal being $(\text{Zr, Hf})_{0.99}\text{Co}_{1.02}(\text{Sb, Sn})_{0.99}$. The low power samples use the optimum sputter condition found in section 5.2.1, while high power samples use a higher current of 100 mA.

As shown in Figure 5.6, all samples show the intended half-Heusler phase, with two dominant crystal directions: The (111) and (001) orientation. The rocking curves are $3\text{-}4^\circ$ and $4\text{-}5^\circ$ for high power and low power samples, respectively, with rocking curves of the (111)-direction being roughly double as wide.

In the low power samples an additional reflex between 30.8° and 31° occurs that does not fit to any reflexes in the powder X-ray diffraction pattern of the target material. In more sensitive powder X-ray diffraction investigations of related materials, several foreign phases have been identified [122], depending on growth conditions and composition. The most prevalent of these are $\text{Hf, (Ti, Hf)}_x\text{Sn}_y$ binary compounds and elemental Sn. The β -Sn-phase fits the XRD-reflex with a slight strain of 1.23%. The Scherrer equation gives an estimate of the size of these potential inclusions [112]:

$$\Delta 2\Theta = \frac{K\lambda}{L \cos(\Theta)} \quad (5.1)$$

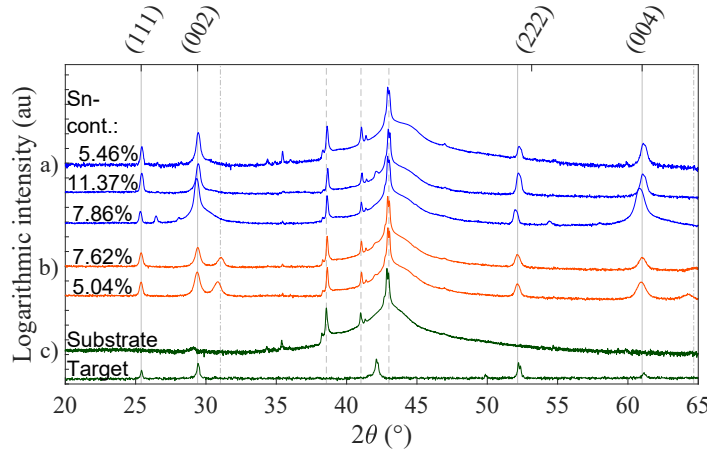


Figure 5.6: X-ray diffraction data of thin films samples from the Sb-excess target. The film reflexes are marked with solid vertical lines, the substrate reflex by broken vertical lines and a foreign phase reflex at $30.8-31^\circ$ by a vertical dash-dot line. The Sn content is given on the left margin and the diffractograms are grouped in three categories:

- a) High power samples, sputtered at 25-28 W.
- b) Low power samples, 10-12 W.
- c) Scan of a substrate and powder diffraction pattern of the target material.

Where K is the Scherrer shape factor, the reflexes half-width is $\Delta 2\Theta$, the wavelength is λ and the diffraction angle is Θ . The equation assumes a regular geometry of the inclusions and relates their finite size with the deviation of their reflexes from the ideal line-shape. For assumed spherical precipitates [113], the equation yields inclusions in the range of 16-18 nm. Consequently, the inclusions are not visible in the SEM-images in Figure 5.5, where the resolution is limited to approximately 30 nm. The SEM-images are augmented by element mapping images, which have been created from energy dispersive X-ray spectroscopy data measured with a FEI Helios NanoLab 600i scanning electron microscope. All investigated samples, low power and high power, show no fluctuations above the noise threshold, which proofs a high homogeneity compared to both investigated bulk samples. The first one is a $Zr_{0.5}Hf_{0.5}CoSb_{0.80}Sn_{0.2}$, which corresponds in composition to the thin film samples with a slightly higher doping level. In previous studies, it showed very little phase separation in comparison to related compounds [122]. The second bulk sample on the other hand, $Ti_{0.33}Zr_{0.33}Hf_{0.33}CoSb_{0.80}Sn_{0.2}$, is an example for a strongly phase separated material [119].

In corresponding AFM images displaying the surface topography (Figure 5.7), features in the discussed size of few tens of nm are clearly visible. However, as the imaging method is insensitive to composition and Sn only makes up 1.82 - 3.79% of the material, it is difficult to attribute individual grains to a possible β -Sn phase. In general, the topographies of samples with and without foreign phase reflexes are similar.

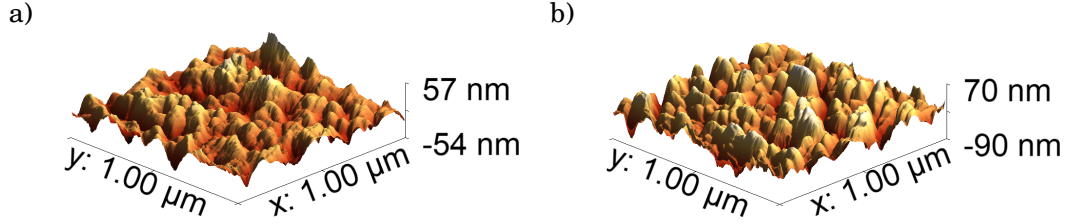


Figure 5.7: Topographic AFM scan of samples with different XRD-properties.

a) A sample showing a foreign phase reflex in the XRD.

b) A sample exhibiting only half-Heusler and substrate reflexes.

5.3 Electronic Characterization

Bulk samples of $(\text{Hf,Zr,Ti})\text{Co}(\text{Sb,Sn})$ exhibit favorable electronic properties for thermoelectric energy conversion, with high Seebeck coefficients and relatively low electrical resistivities [125]. However, they also show a pronounced sensitivity towards deviations in their composition, especially in the ratio of Sb to Sn [119]. Therefore, the sputtering process from a single 5-component target represents an particularly challenging task. It encompasses the simultaneous optimization of composition, crystalline quality and film morphology.

After the successful demonstration of near stoichiometric growth in section 5.2.2, this chapter summarizes the comparison of electronic properties of bulk and thin film samples. As minuscule amounts of electronic defects potentially alter the electronic make-up of a material, details of the growth process are crucial. This is especially true for the presented material family, as spontaneous phase separation can easily come to dominate its behavior.

Consequently, two bulk samples act as a reference. The first, $\text{Zr}_{0.5}\text{Hf}_{0.5}\text{CoSb}_{0.80}\text{Sn}_{0.2}$, only exhibits comparatively little phase separation. It corresponds in composition to the target material. $\text{Ti}_{0.33}\text{Zr}_{0.33}\text{Hf}_{0.33}\text{CoSb}_{0.80}\text{Sn}_{0.2}$ on the other hand, tends to phase separate to a much larger degree.

Due to composition variations caused by the deposition process, all thin film samples exhibit a lower Sn on Sb substitution compared to the bulk samples. In both bulk samples 20% of Sb is substituted, while in the investigated thin films it amounts to 5.5%, 9.0% and 11.4%, respectively. As Sn acts as an acceptor, the lowered substitution corresponds to a lower doping level.

In the deposition process, the sputter power presents itself as the most crucial parameter. Multiple sputter powers produce viable samples in respect to composition, but distinct crystalline and morphological features. Consequently, the analysis includes thin films of different sputter powers: Two high power and one low power sample. The selected thin films correspond to a subset with a composition close to the ideal.

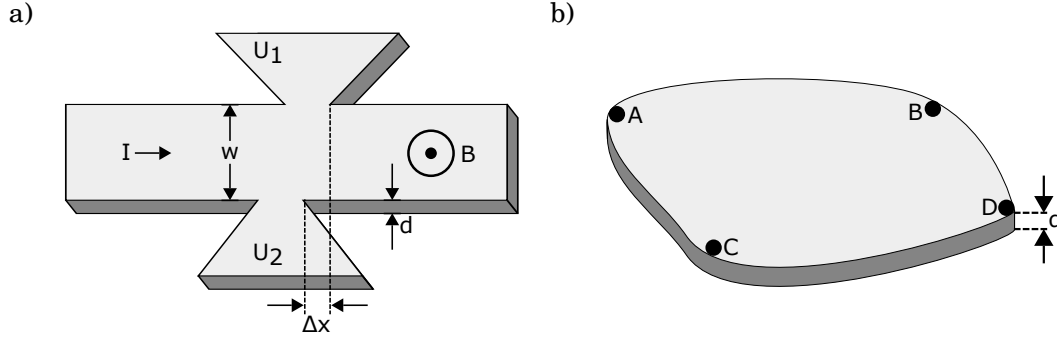


Figure 5.8: Measurement structures for Hall-effect measurements.

- a) Hall-bar structure, sketched with an exaggerated lateral offset.
 b) Van-der-Pauw-configuration.

5.3.1 Experimental Setup

A variable temperature cryostat supplied temperatures in a range of 2 to 300 K for resistivity and Hall-effect measurements. As part of the setup, an 11 T superconducting magnet drives a -5 to 5 T ramp to generate the necessary Hall voltages. Different approaches ensure clear, low noise signals for thin film bulk samples: A structuring step employing optical lithography produces a Hall bar geometry from the thin films (Figure 5.8a). For an ideal Hall-bar, the 0 T voltage is zero, for higher field the signal is purely given by the Hall-voltage. The bulk samples, on the other hand, remain unstructured except for a polishing step reducing their overall thickness. As the Hall-signal is inversely proportional to the thickness, the signal to noise-ratio is improved for thinner samples. Four contacts on the edges of the polished samples provide a van-der-Pauw terminal setup (Figure 5.8b).

Despite of the pre-structuring, several noise-sources play an important role. The influence is especially pronounced in a subset of samples with a comparatively low intrinsic signal. For the thin film samples, the most significant error lies in the structuring process: Slight irregularities lead to an offset Δx between opposing Hall voltage contacts. The signal therefore contains a longitudinal contribution $U_\rho \propto \rho \Delta x$. As this contribution is resistive, it shares the same temperature dependence (approx. $U_\rho \propto T$) and field dependence ($U_\rho \propto B^2$) with the main film resistivity. To subtract this contribution, the magnetic field is ramped from a negative field to a positive field of the same magnitude. An symmetrising operation applied on the data separates the resistive contribution from the Hall Signal. As the Hall-voltage depends asymmetrically on the field ($U_H \propto B$) and the resistivity symmetrically ($U_\rho \propto B^2$), the process ideally yields the pure Hall-voltage:

$$U_{H,asym}(B) = \frac{U_{raw}(B) - U_{raw}(-B)}{2} \quad (5.2)$$

$$= U_H(B) \quad (5.3)$$

and

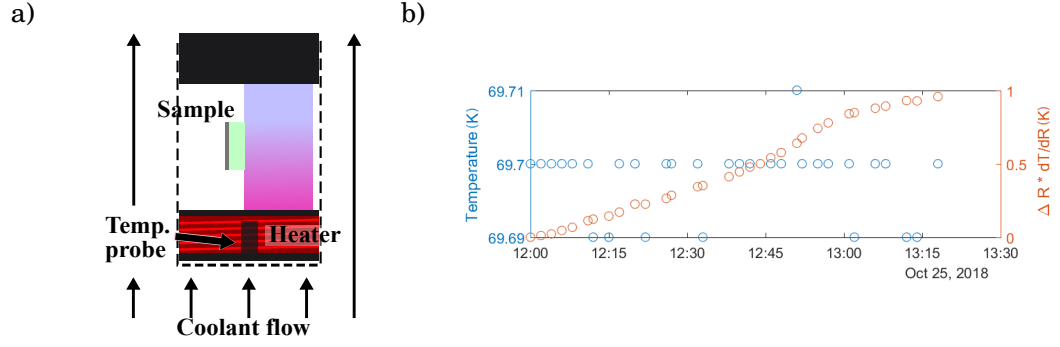


Figure 5.9: Effect of sample space geometry on temperature measurement.

a) The color gradient illustrates a temperature difference between the heater position and the sample mount. The temperature probe is situated within the heater coil.

b) Temperature measured by the temperature probe (blue) and the deviation of real sample temperature as inferred by its resistance characteristics (red).

$$U_{H,sym}(B) = \frac{U_{raw}(B) + U_{raw}(-B)}{2} \quad (5.4)$$

$$= U_{\rho}(B) \quad (5.5)$$

However, a non-zero resistive contribution persists in the asymmetrical part as a result of a temperature drift ΔT between the measurements $U_{raw}(B)$ and $U_{raw}(-B)$. In this case, the resistive contributions of both measurements do not cancel, and the residual error is determined by the temperature coefficient of the material

$$U_{H,asym}(B, \Delta T) = U_H(B) + \frac{1}{2} \frac{dU_{\rho}}{dT} \Delta T \quad (5.6)$$

This makes the temperature stability the main limiting factor in the measurement of low signal samples. In practice, two heaters are employed to lead to a constant temperature in the sample space. One of them heats the gas flow, while the other applies heat to the sample space itself. Both of them counteract the coolant flow to enable a more adaptive temperature regulation. The controllability and fast response of the electrical heaters compensate variations in the coolant flow. In fact, the design of the used coolant system is prone to long term drifts in gas flux. While the heaters can compensate the varying flow, a drift in real sample temperature can result from the sample space geometry. Figure 5.9a shows an illustration of the sample space, while Figure 5.9b shows an exemplary temperature measurement under changing coolant flow. The temperature is measured by the sample space thermometer on the one hand and calculated from the sample resistance on the other hand. To calculate the second value, the temperature coefficient of the

resistance $dR(T)/dT$ in a separate measurement, from which the temperature drift can be inferred with

$$\Delta T = \frac{dR}{dT} \Delta R. \quad (5.7)$$

With the resistance change ΔR and the underlying temperature difference ΔT .

The measurement reveals a drift of 1 K of the real sample temperature over 90 minutes, while the measured sample space temperature stayed constant within 2/100 K. The reason for the difference lies in a temperature gradient in the sample space, with the area close to the heater being hotter. With reducing coolant flow and thus less efficient cooling, the heater power reduces accordingly and the gradient diminishes. During a measurement, this temperature drift cannot be monitored constantly, which is why care must be taken to minimize coolant flow drift. Even so, a residual error from this source likely persists. table 5.2 shows the resistive offset, the temperature coefficient and an estimate of the influence of a supposed 1 K temperature drift on the measured signal.

The intrinsically lower magnitude of Hall-signals and resistive contribution in part of the sample series makes the use of a more sophisticated measurement scheme necessary. In this scheme, instead of a continuous ramp, the magnetic field is alternated between positive and negative field in successive measurements. This protocol minimizes the time between individual measurements and thus the temperature drift. At the same time, supposing the temperature changes by a constant value ΔT between measurements, the residual resistive offset can be subtracted by an additional measurement step. This is done with the magnetic fields $(B_+, B_-, B_+) = (B, -B, B)$ at temperatures $(T_1, T_2, T_3) = (T, T + \Delta T, T + 2\Delta T)$ in consecutive measurements by applying the correction:

Sample	Resistive offset (mV)	Temperature coefficient ($\cdot 10^{-3}$ 1/K)	6 T Hall- Voltage (μ V)	Resistive drift (μ V)	Relative error
1	-1.9	1.04	80	2	2.5%
2	0.6	0.36	1.6	0.24	15%
3	-4.3	0.89	11	3.82	34.7%

Table 5.2: Overview over thin film samples Hall signals and the resistive drift upon a supposed 1 K change in sample temperature. The sample 1, 2 and 3 stand for the thin films with the composition $\text{Zr}_{0.47}\text{Hf}_{0.60}\text{Co}_{0.93}\text{Sb}_{0.95}\text{Sn}_{0.05}$, $\text{Zr}_{0.46}\text{Hf}_{0.53}\text{Co}_{1.04}\text{Sb}_{0.90}\text{Sn}_{0.9}$, and $\text{Zr}_{0.44}\text{Hf}_{0.59}\text{Co}_{0.94}\text{Sb}_{0.91}\text{Sn}_{0.11}$, respectively.

$$U_{H,asym}(B) = \frac{1}{2} \left(\frac{U_{raw}(+B, T_1) + U_{raw}(+B, T_3)}{2} - U_{raw}(-B, T_2) \right) \quad (5.8)$$

$$= \frac{1}{2} \left(\frac{U_H(+B) + U_\rho(+B) + [U_H(+B) + U_\rho(+B) + \alpha 2\Delta T]}{2} \right) \quad (5.9)$$

$$- [-U_H(-B) + U_\rho(-B) + \alpha \Delta T] \right) \quad (5.10)$$

$$= U_H(B) \quad (5.11)$$

with $\alpha = \frac{dU_\rho}{dR}$ being the temperature coefficient of resistance. With this protocol the Hall-constant the Hall-constant can be determined reliably even for low-signal samples.

Seebeck-Coefficient Measurement Setup

For the Seebeck measurements a homemade device is used: The samples are clamped between two copper blocks, one of which is heated. In this way a temperature gradient of around 3° C/mm is generated with a mean temperature around 70 °C. Thermocouples are placed on two distinct points on the sample surface. The thermovoltages of the individual thermocouples provide the local temperature of the contact points. With the same leads, the voltage difference between the two points can be measured. The ratio of the voltage difference and the temperature difference yields the Seebeck coefficient of the material at a temperature slightly elevated above room temperature.

$$S = - \frac{\Delta V}{\Delta T} \quad (5.12)$$

5.3.2 Results and Discussion

Seebeck Coefficient

Depending on sputter power, the thin film Seebeck coefficients transition from positive to negative sign (Table 5.1). At high power conditions they are positive and increase monotonically with the content of acceptor-like Sn. For low power samples they are negative, which is in agreement with the assumption of Sn precipitations. With part of the Sn missing from the half-Heusler matrix, it resembles the n-type host material (Zr,Hf)CoSb [126].

Overall, the thin films exhibit a lower Seebeck coefficient by roughly one order of magnitude relative to the bulk samples.

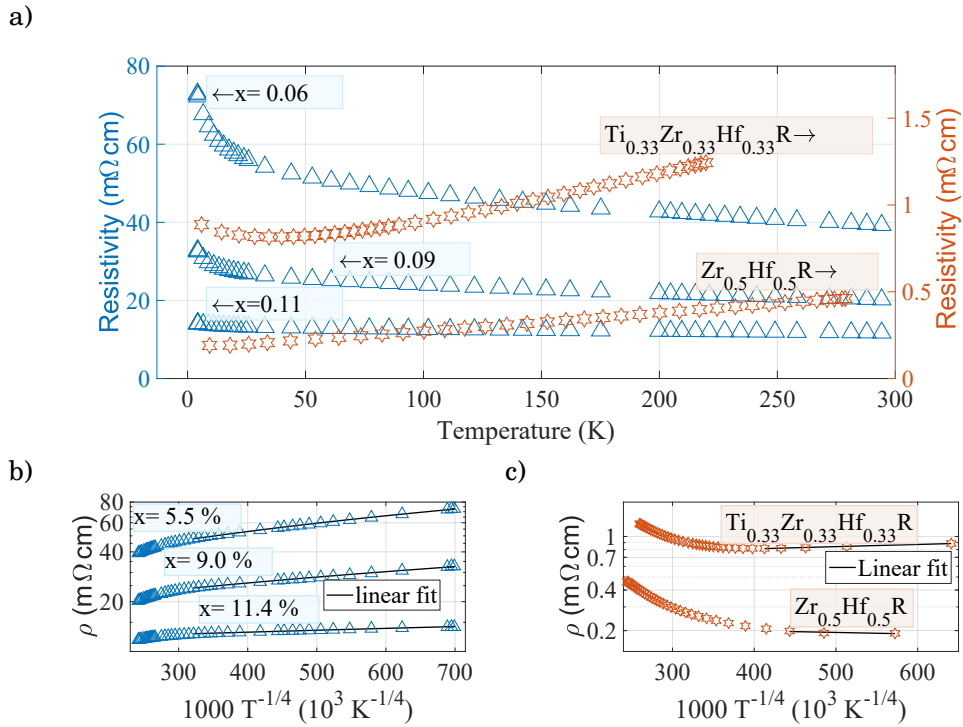


Figure 5.10: Temperature dependent resistivity of $(\text{Zr}_{0.5}\text{Hf}_{0.5})\text{Co}(\text{Sb}_{1-x}\text{Sn}_x)$ thin films and $\text{Zr}_{0.5}\text{Hf}_{0.5}\text{CoSb}_{0.80}\text{Sn}_{0.2}$ and $\text{Ti}_{0.33}\text{Zr}_{0.33}\text{Hf}_{0.33}\text{CoSb}_{0.80}\text{Sn}_{0.2}$ bulk samples.

a) Overview over sample resistivity for thin films (left) and bulk samples (right).

b) $\log(\rho)$ vs $1/T^{0.25}$ -representation of thin film resistivity.

c) $\log(\rho)$ vs $1/T^{0.25}$ -representation of bulk resistivity.

Resistivity

The thin film samples show a decrease in resistivity towards higher temperatures. The increase is steep at low temperatures and flattens towards 300 K, see Figure 5.10a. While the decreasing resistivity is indicative of a semiconductor, the range is uncharacteristically low: The total change stays within a factor of two. Comparing the overall level, a dependence on Sn-content is apparent. The higher the substitution of Sb by acceptor-like Sn, the lower the resistivity. Below roughly 100 K, the material adapts a $\log(\rho) \propto T^{-1/4}$ behavior (Figure 5.10b), which indicates a variable range hopping (VRH) transport mechanism [91, 92].

The corresponding bulk samples show a resistivity that is lower by roughly one order of magnitude (Figure 5.10a). It increases towards higher temperatures, indicative of a semi-metal. This is in compliance with several previous studies, where the material was found to behave semi-metal-like [118]. However, at low temperatures, resistivity increases slightly, akin to the thin films. The lower overall resistivity compared to these thin films could be attributed to the higher doping level. In bulk samples 20 % of Sb is substituted by Sn, while in thin films substitution only amounts to 5.5 %, 9.0 % and 11.4 %, respectively.

Hall Effect

The Hall effect signals of both bulk and thin film samples are linear in B over the whole temperature range (Figure 5.11), with the Hall voltage varying strongly between samples. It ranges from $U_H = 0.25\mu\text{V}$ to $10\mu\text{V}$ at 5 T for the thin film samples and $0.9\mu\text{V}$ to $2\mu\text{V}$ at 5 T for the bulk samples. Because of the low intensity of the signals, they can be significantly distorted by various noise sources described in section 5.3.1.

The Hall constants determined from the slope of the Hall-signals are positive for high temperatures, as was previously reported for this material [118]. However, at low temperatures the sign of the Hall constant changes for all thin film samples, suggesting a transition from hole-dominated transport to electron conduction. While the $\text{Zr}_{0.5}\text{Hf}_{0.5}\text{CoSb}_{0.80}\text{Sn}_{0.2}$ bulk sample also changes sign between 2.5 and 9.6 K, the $\text{Ti}_{0.33}\text{Zr}_{0.33}\text{Hf}_{0.33}\text{CoSb}_{0.80}\text{Sn}_{0.2}$ bulk sample stays p-type conducting down to the lowest temperature of 2.46 K.

The charge carrier concentrations calculated from these Hall-constants reflect the variability already observed in the raw Hall-signals. The charge carrier concentrations given in Figure 5.12a result from the relation $n = -\frac{1}{eR_H}$ [89], where R_H is the Hall constant and e is the elementary charge. However, this equation relies on a single dominant charge carrier species, which is a questionable assumption at least for parts of the temperature range. At high temperatures, where all samples show a clear p-type behavior, the charge carrier concentrations vary by more than one order of magnitude between samples, with no clear dependence between Sn-content and charge carrier concentration. Part of this variation is likely caused by varying degrees of compensation of electrons and holes. Thus, in a more sophisticated model, both charge carrier types are considered using the relation [89]

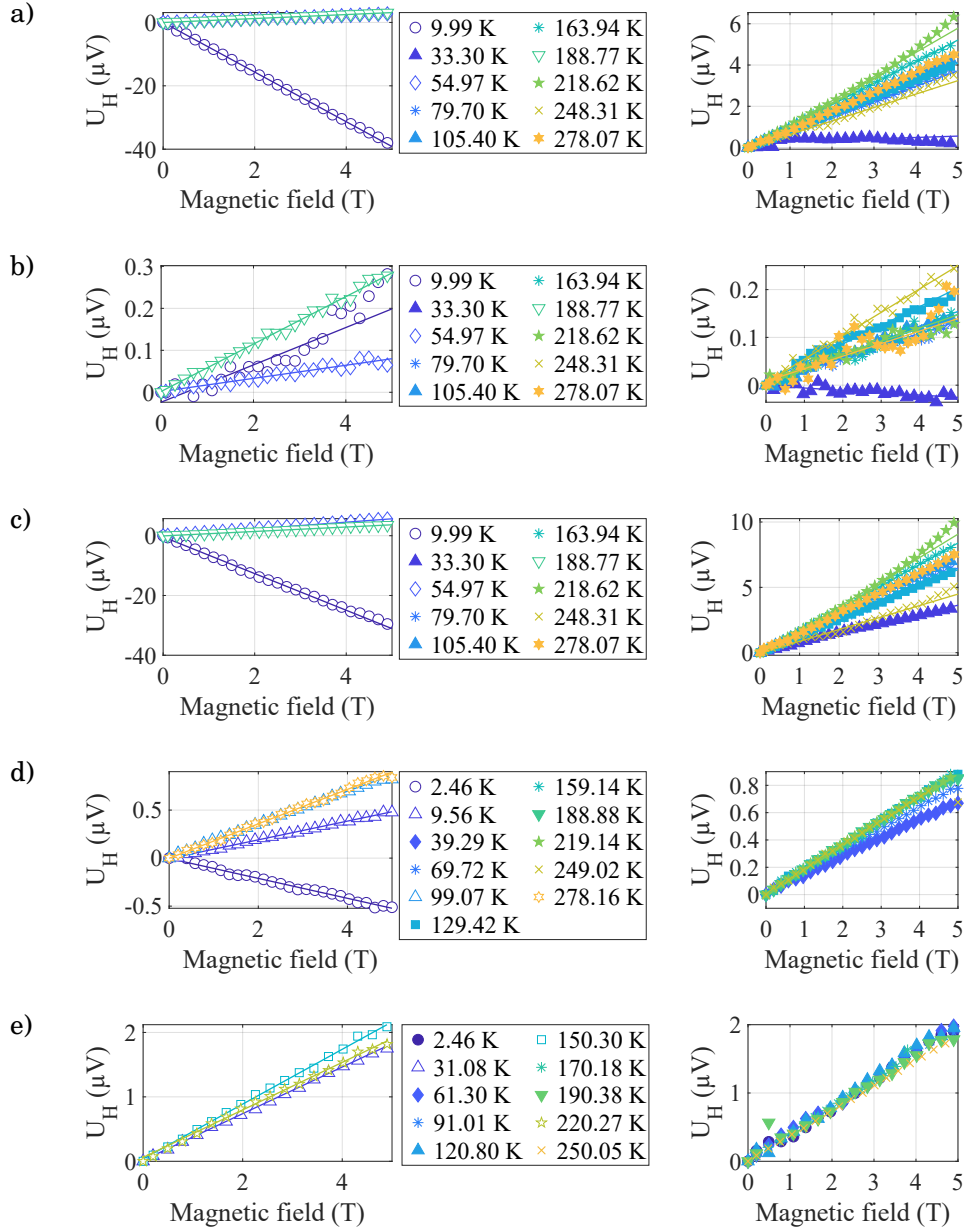


Figure 5.11: Hall voltage raw data for thin film and bulk samples. Hall voltages are symmetrized to account for different contributions discussed in section 5.3.1. A selection of datasets are shown in the left column with empty symbols. The right column displays all datasets with a positive slope.

- a) $\text{Zr}_{0.47}\text{Hf}_{0.60}\text{Co}_{0.93}\text{Sb}_{0.95}\text{Sn}_{0.05}$ thin film
b) $\text{Zr}_{0.44}\text{Hf}_{0.59}\text{Co}_{0.94}\text{Sb}_{0.91}\text{Sn}_{0.11}$ thin film
c) $\text{Zr}_{0.46}\text{Hf}_{0.53}\text{Co}_{1.04}\text{Sb}_{0.90}\text{Sn}_{0.09}$ thin film
d) $\text{Zr}_{0.5}\text{Hf}_{0.5}\text{CoSb}_{0.80}\text{Sn}_{0.20}$ bulk sample
e) $\text{Zr}_{0.33}\text{Hf}_{0.33}\text{Ti}_{0.34}\text{CoSb}_{0.80}\text{Sn}_{0.20}$ bulk sample

a)

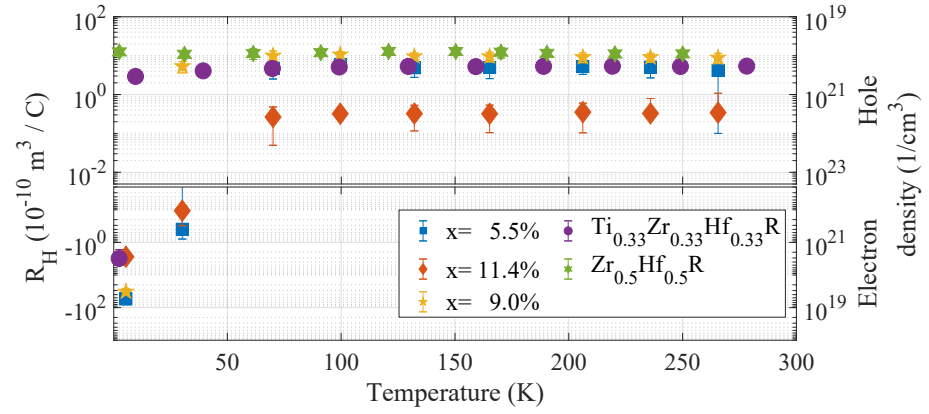


Figure 5.12: Temperature dependent Hall constant data of $(\text{Zr}_{0.5}\text{Hf}_{0.5})\text{Co}(\text{Sb}_{1-x}\text{Sn}_x)$ thin films and $\text{Zr}_{0.5}\text{Hf}_{0.5}\text{R}$ and $\text{Ti}_{0.33}\text{Zr}_{0.33}\text{Hf}_{0.33}\text{R}$ bulk samples with $\text{R} = \text{CoSb}_{0.80}\text{Sn}_{0.2}$.

a) Overview over experimental data in logarithmic representation with positive values in the top plot and negative data in the lower one. The left y-axis shows the Hall constant, while the right one displays the corresponding electron and hole densities in a single band model. The error bars correspond to the uncertainties from the fit of the Hall signal.

$$R_H = \frac{p\mu_p^2 - n\mu_n^2}{e(p\mu_p + n\mu_n)^2} \quad (5.13)$$

With the charge carrier concentrations n and p and the charge carrier mobilities μ_n and μ_p for electrons and holes, respectively.

However, as this equation relies on four free parameters (n , p , μ_n , μ_p) instead of 1, additional assumptions are necessary, to reduce complexity.

5.3.3 Models of Electronic Transport

When accounting for interacting impurity states three cases can be distinguished that depend on the concentration of electronic defects:

- At low concentrations of acceptor-states, the electronic properties are determined by thermal excitation of electronic holes from acceptor states into the valence band. The temperature dependence will be widely dominated by the charge carrier densities, which depend exponentially on temperature.
- At high concentration levels, acceptor states will overlap to form an impurity band, which dominates the electronic properties. The material will act semi-metal like, which concurs with bulk resistivity data and previous reports for bulk samples [118]

at high temperatures. In this case the charge carrier density is widely independent of temperature, $n, p = \text{const.}$

- At intermediate concentrations electronic holes will not be completely delocalized. However, they will be able to hop from one defect state to the other. While different hopping mechanisms can be prevalent, this process is effectively thermally activated and can lead to the typical $\log(\rho) \propto T^{-1/4}$ temperature behavior of the resistivity observed at low temperatures in thin films (Figure 5.10b).

Thermal Excitation of Holes

From the transition of n-type to p-type in most samples, an increase of electronic hole concentration is apparent towards higher temperatures. The thermal excitation of holes from electronic defects can explain this increase. The model sketched in this section corresponds to the first case explained in section 5.3.3.

As candidates for these dominant defects, there are several possibilities. The most common one is extrinsic: Sn-on-Sb sites were purposefully introduced by substitution. They represent deep acceptor-like defects with relatively high activation energies [29].

Apart from these extrinsic substitution, there are several intrinsic defects, with the lowest formation energies being represented by Cobalt interstitials (Co(i)) and Cobalt vacancies (V(Co)), both of which act as electron donors. As all samples exhibit a slight excess of Co, the Co(i) defect states are expected to be dominant. Due to its relatively low activation energy, they will contribute a mostly constant electronic background, $n = \text{const.}$, which is competing with and partly compensates electronic holes from thermally activated Sn-on-Sb defect states.

The relatively constant high temperature resistivity and Hall effect indicate little variation of the mobility at high temperatures. It is also negligible in the narrow region of transition between n- and p-type, where a strong change in charge carrier number is assumed in this model.

Consequently, the electron mobility μ_e will be assumed constant with temperature: $\mu_e = \text{const.}$ the hole mobility μ_p will be assumed constant for thin film samples and weakly $\mu_p \propto \frac{1}{T}$ in bulk samples, to account for semi-metal like behavior.

The electronic hole density p follows an Arrhenius-type behavior depending on the characteristic activation energy of acceptors E_p and acceptor density p_0 :

$$p = p_0 \exp(-E_p/k_B T). \quad (5.14)$$

With this set of parameters, together with the elementary charge e , both the Hall constant $R_H(T)$ and resistivity $\rho(T)$ can be expressed:

$$\rho(T) = 1/(nb + p(T))e\mu_p \quad (5.15)$$

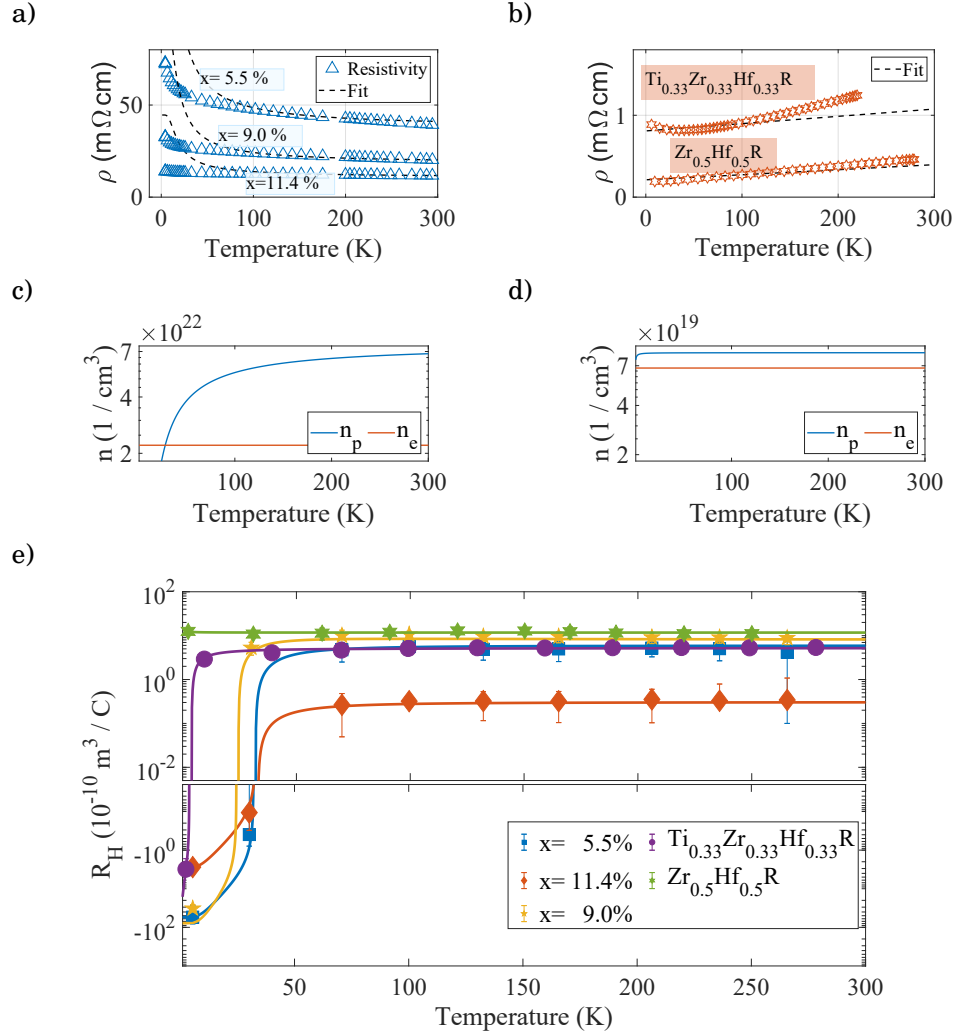


Figure 5.13: Fit of resistivity and Hall constant using the model of thermally excited electronic holes.

a) $(\text{Zr}_{0.5}\text{Hf}_{0.5})\text{Co}(\text{Sb}_{1-x}\text{Sn}_x)$ thin film resistivities.

b) $\text{Zr}_{0.5}\text{Hf}_{0.5}\text{R}$ and $\text{Ti}_{0.33}\text{Zr}_{0.33}\text{Hf}_{0.33}\text{R}$ bulk sample resistivities with $\text{R} = \text{CoSb}_{0.80}\text{Sn}_{0.20}$.

c) Charge carrier density of the $(\text{Zr}_{0.44}\text{Hf}_{0.59})\text{Co}_{0.94}(\text{Sb}_{0.91}\text{Sn}_{0.11})$ thin film sample.

d) Charge carrier density of the $(\text{Zr}_{0.5}\text{Hf}_{0.5})\text{Co}(\text{Sb}_{0.80}\text{Sn}_{0.20})$ bulk sample.

e) Temperature dependent Hall constants.

$$R_H(T) = \frac{p(T) - nb^2}{e(p(T) + nb)^2}. \quad (5.16)$$

In total, the model is based on six parameters, p_0 , E_p , n_e , b , μ_p and the electron mobility, which is dependent on the other parameters, $\mu_e = \mu_p b$. The values used in Figure 5.13 are given in table 5.3.

The parameters are determined by the data to different degrees of certainty. While p_0 can be deduced reliably from the high temperature Hall constant and μ_p from high temperature resistivity, both E_p and b are more complex. Together they determine the position of the transition region from n- to p-type. The experimental data can be reproduced satisfactorily with multiple pairs of E_p and b . consequently, only their order of magnitude can reliably be determined. However, with a level of around 6 meV for the thin film samples, it is apparent that the activation energy is lower than expected for a deep acceptor state. This is even more clear for the bulk samples, which exhibit an activation energy of around 10^{-2} meV.

	HP 5.5%	HP 11.4%	LP 9.0%	Bulk 1	Bulk 2
$n_{p,0}$ (1/cm ³)	$4.1 \cdot 10^{21}$	$7.7 \cdot 10^{22}$	$4.0 \cdot 10^{21}$	$8.4 \cdot 10^{19}$	$5.1 \cdot 10^{21}$
E_p (meV)	6	6	6	$1.7 \cdot 10^{-2}$	$2.6 \cdot 10^{-2}$
n_e (1/cm ³)	$1.1 \cdot 10^{21}$	$2.2 \cdot 10^{22}$	$8.0 \cdot 10^{20}$	$6.8 \cdot 10^{19}$	$5.3 \cdot 10^{19}$
b	1.1	1.1	1.1	1.1	1.1
μ_p (cm ² /Vs)	$3.10 \cdot 10^{-2}$	$0.58 \cdot 10^{-2}$	$0.70 \cdot 10^{-2}$	195	1.72
μ_e (cm ² /Vs)	$3.41 \cdot 10^{-2}$	$0.63 \cdot 10^{-2}$	$0.75 \cdot 10^{-2}$	214.5	1.89

Table 5.3: Parameters used in the model for bulk (Bulk 1 and 2) and thin film samples grown at a high sputter power (HP) and low sputter power (LP) at varying Sn-on-Sb substitution levels.

(HP 5.5%) 5.5% substitution, grown at ~25 W.

(HP 9.0%) 9% substitution, grown at ~25 W.

(LP 11.4%) 11.4% substitution, grown at ~10 W.

(Bulk 1) Zr_{0.5}Hf_{0.5}CoSb_{0.80}Sn_{0.20} bulk sample.

(Bulk 2) Zr_{0.33}Hf_{0.33}Ti_{0.34}CoSb_{0.80}Sn_{0.20} bulk sample.

5 *P-type thin film $\text{Hf}_{0.5}\text{Zr}_{0.5}\text{CoSb}_{1-x}\text{Sn}_x$*

The electron density, finally, is determined by fitting the model to the data with the previously determined parameters. The initial guess for the fit can be deduced from the low temperature Hall constant data, where n-type conduction is dominant.

While the model of thermally activated electronic hole concentration can explain the Hall constant and the high temperature resistivity for thin films, it deviates for bulk samples and low temperature resistivity. This deviation could be caused by the failure of the assumption of independent Sn-on-Sb-states. With a substitution level of 5.5%, 9.0% and 11.4% for thin film samples and 20% for bulk samples it is likely that some form of interaction between defect states will take place. This is especially true for bulk samples with their higher level of substitution, for which the model fits markedly worse.

With considering only the first case, the simple model presented in this section can clearly not capture the full complexity of the electronic structure. In the next section, a complementary model is detailed, which assumes the third case of partially delocalized defect states, which enable hopping mechanisms to dominate electronic transport.

Hole Localization

A $\log(\rho) = 1/T^{1/4}$ temperature dependence fits well to the low temperature thin film data, indicating a dominance of hopping mechanisms. This means that the assumption of free charge carriers is questionable. More likely, the electrons and holes move through a complex energy landscape. They find localized states, the characteristic energies of which vary with their individual environments. Charge carriers move from defect to defect, with the transition probability depending on how close they are in space and energy. This mechanism, called variable range hopping (VRH), is described in detail in section 3.2. It leads to a characteristic $\log \rho \propto 1/T^{1/4}$ dependence of resistivity on temperature.

With increasing temperature, charge carriers enter the nearest neighbor hopping (NNH) regime, where hopping is mainly limited to adjacent atoms. This type of localization leads to the resistivity adapting an Arrhenius-type behavior, $\log(\rho) \propto 1/T$.

Figure 5.14 presents a model, where electronic transport is dominated by the hopping mechanisms described above.

The holes in this picture are confined to a deep impurity band formed by Sn-on-Sb doping sites. The density of holes is taken as constant, $p = \text{const}$, with their mobility following a combination of VRH and NNH:

$$\mu_{films} = \mu_{NNH} + \mu_{VRH} \quad (5.17)$$

$$= \mu_{NNH,0} \exp\left(-\frac{E_{NNH}}{k_B T}\right) + \mu_{VRH,0} \exp\left(-\frac{\phi_{VRH}}{T^{1/4}}\right) \quad (5.18)$$

For bulk samples, the VRH-part is neglected. However, an additional term is introduced to account for the semi-metal behavior at high temperatures:

$$\mu_{bulk} = \left[\mu_{NNH,0} \exp\left(-\frac{E_{NNH}}{k_B T}\right) \right] \cdot \left(\frac{1}{\alpha T + \beta} \right) \quad (5.19)$$

A constant background of electrons, provided by cobalt interstitials, is assumed, $n = \text{const}$. As their activation energy is low [29], they are assumed to be ionized even at low temperatures. These electrons can move freely through the conduction band, in contrast to the holes in the only partly-continuous impurity band, therefore their mobility dependence is neglected ($\mu_e \approx \text{const}$).

The model implicitly assumes the coexistence of holes and electrons. This is typical in semi-metals, when valence and conduction band overlap.

While band-structure calculations of $(\text{Hf, Zr, Ti})\text{Co}(\text{Sb}_x\text{Sn}_{1-x})$ reveal a band-gap, several mechanisms can lead to band-bending and ultimately band-overlap. The most commonly discussed are Zr-Sn antisite defects [127], Co-Frenkel pairs [27] and Co-interstitials [128].

In total the model consists of seven free parameters (Table 5.4) and μ_p as a depen-

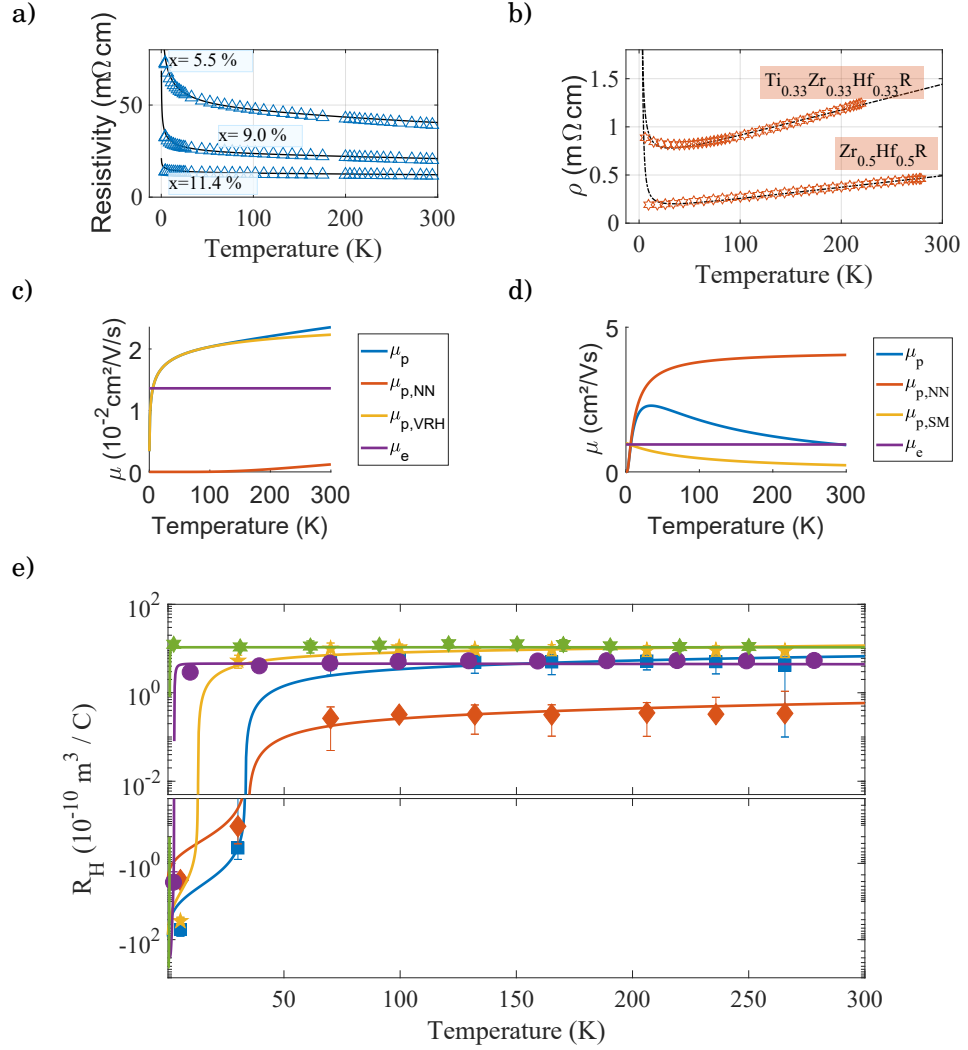


Figure 5.14: Fit of resistivity and Hall constant using the model of thermally excited electronic holes.

a) $(\text{Zr}_{0.5}\text{Hf}_{0.5})\text{Co}(\text{Sb}_{1-x}\text{Sn}_x)$ thin film resistivities.

b) $\text{Zr}_{0.5}\text{Hf}_{0.5}\text{R}$ and $\text{Ti}_{0.33}\text{Zr}_{0.33}\text{Hf}_{0.33}\text{R}$ bulk sample resistivities with $\text{R} = \text{CoSb}_{0.80}\text{Sn}_{0.20}$.

c) Charge carrier mobility of the $(\text{Zr}_{0.45}\text{Hf}_{0.54})\text{Co}_{1.02}(\text{Sb}_{0.92}\text{Sn}_{0.08})$ thin film sample.

d) Charge carrier mobility of the $(\text{Zr}_{0.5}\text{Hf}_{0.5})\text{Co}(\text{Sb}_{0.80}\text{Sn}_{0.20})$ bulk sample.

e) Temperature dependent Hall constant.

dent parameter. These hopping coefficients are determined from the resistivity, while the charge carrier densities follow from the Hall constant data, analogous to the corresponding quantities in the thermal excitation model (Section 5.3.3).

The mobilities are roughly one to two order of magnitudes smaller for thin films compared to bulk. This can have two reasons:

- The structural order is lower.
- The lower doping levels lead to less available acceptor-levels and thus potentially to a less continuous impurity band.

The lower structural order is supported by the relatively broad rocking curves found in the XRD-examination of the thin films. Both effects lead to a stronger dominance of hopping mechanisms.

The low power sample with 9% substitution has the lowest hole density, despite of having a significantly higher Sn-content than other thin film samples. This supports the assumption, that part of the Sn precipitates and therefore does not act as a dopant (see Section 5.2.2).

In conclusion, the localization of holes in an impurity band explains both the increase in resistivity at low temperatures and the change in dominant charge carrier species at low temperatures. The model fits significantly better for thin films than for bulk samples, which could mean that bulk samples are in transition from case 2 to case 3 described in section 5.3.3: Electric holes are almost completely delocalized in an impurity band and localization is only noticable at very low temperatures.

However, the $(\text{Hf}_{0.5}\text{Zr}_{0.5})\text{Co}(\text{Sb}_x\text{Sn}_{1-x})$ bulk sample changes sign at low temperatures, implying localization and transport carried by electrons and holes, thus bipolar transport. In case of bipolar transport, the electron contribution diminishes the hole contribution [129]:

$$S = \frac{\sigma_p S_p - \sigma_n S_n}{\sigma_p + \sigma_n} \quad (5.20)$$

This effect can explain the lower Seebeck coefficient compared to $(\text{Hf}_{0.33}\text{Zr}_{0.33}\text{Ti}_{0.33})\text{Co}(\text{Sb}_x\text{Sn}_{1-x})$.

Potentially, the electron background and partial hole localization are important to understand the properties of the material family as a whole.

	HP 5.5%	HP 11.4%	LP 9.0%	Bulk 1	Bulk 2
$n_{p,0}$ ($1/\text{cm}^3$)	$3.14 \cdot 10^{21}$	$1.08 \cdot 10^{22}$	$1.95 \cdot 10^{21}$	$1.35 \cdot 10^{22}$	$5.82 \cdot 10^{21}$
n_e ($1/\text{cm}^3$)	$5.11 \cdot 10^{20}$	$1.90 \cdot 10^{22}$	$4.68 \cdot 10^{20}$	$2.13 \cdot 10^{20}$	$1.17 \cdot 10^{20}$
$\mu_{0,VRH}$ (cm^2/Vs)	$5.55 \cdot 10^{-2}$	$3.00 \cdot 10^{-2}$	$16.0 \cdot 10^{-2}$	-	-
ϕ_{VRH} ($\text{K}^{1/4}$)	10.8	2.29	5.02	-	-
$\mu_{0,NN}$ (cm^2/Vs)	$2.03 \cdot 10^{-2}$	$0.90 \cdot 10^{-2}$	$6.02 \cdot 10^{-2}$	1	1
E_{NN} (meV^3)	51.70	51.68	60.24	0.82	0.32
$\mu_{0,p}$ (cm^2/Vs)	$7.58 \cdot 10^{-2}$	$3.90 \cdot 10^{-2}$	$22.0 \cdot 10^{-2}$	1	1
μ_e (cm^2/Vs)	$6.46 \cdot 10^{-2}$	$1.36 \cdot 10^{-2}$	$14.8 \cdot 10^{-2}$	0.95	0.1

Table 5.4: Parameters used in the model for bulk (Bulk 1 and 2) and thin film samples grown at a high sputter power (HP) and low sputter power (LP) at varying Sn-on-Sb substitution levels.

(HP 5.5%) 5.5% substitution, grown at ~ 25 W.

(HP 9.0%) 9% substitution, grown at ~ 25 W.

(LP 11.4%) 11.4% substitution, grown at ~ 10 W.

(Bulk 1) $\text{Zr}_{0.5}\text{Hf}_{0.5}\text{CoSb}_{0.80}\text{Sn}_{0.20}$ bulk sample.

(Bulk 2) $\text{Zr}_{0.33}\text{Hf}_{0.33}\text{Ti}_{0.34}\text{CoSb}_{0.80}\text{Sn}_{0.20}$ bulk sample.

5.4 Conclusion

In this chapter, near stoichiometric growth of thin films from a single 5-component magnetron sputter target has been demonstrated. Different target configurations and sputter conditions yield a range of different compositions, growth qualities and film morphologies. Of the different parameters, the sputter power stands out as the most relevant. Consequently, thin films sputtered at different powers were compared with two bulk reference samples, strongly phase separated $\text{Zr}_{0.33}\text{Hf}_{0.33}\text{Ti}_{0.34}\text{CoSb}_{0.80}\text{Sn}_{0.20}$ and more homogeneous $\text{Zr}_{0.5}\text{Hf}_{0.5}\text{CoSb}_{0.80}\text{Sn}_{0.20}$. The data shows a transition from semiconductor, over hopping, to semi-metal like behavior depending on Sn-on-Sb substitution. In this transition, the bulk samples are closer to the semi-metal side, while in the thin films the hopping mechanisms dominate. This is caused by a lower Sn-content, further lowered by Sn precipitating into nano-inclusions in some samples. The resulting lower doping level leads to a discontinuous impurity band.

To explain the electronic properties, two different models are applicable. A model describing thermal excitation of holes reproduces the Hall constants reasonably. However it fails for bulk and low temperature thin film resistivity. A complementary model relying on hole localization provides a better agreement to the resistivity and retains a reasonable agreement with the Hall constant. While it fits markedly better to thin films, it also roughly replicates bulk resistivity. To understand the reason for the deviations, it is important to review the assumptions that underpin either model and the physical realities behind it. As discussed above, the Hall constant of a semiconductor is given by

$$R_H = \frac{p\mu_p^2 - n\mu_n^2}{e(p\mu_p + n\mu_n)^2}, \quad (5.21)$$

where, in its general form, all four quantities depend on temperature, $n(T), p(T), \mu_n(T), \mu_p(T)$. Charge carriers have a finite probability to be thermally excited that increases with rising temperature. On the other hand, the mobilities are unlikely to be flat, with the underlying scattering mechanisms being typically heavily temperature dependent. Nevertheless, either model disregards one mechanism in favor of the other. The localization model focuses on the hole mobility $\mu_p(T)$, fixing the parameters $\mu_e, n, p = \text{const}$, while the thermal excitation model investigates the hole density $p(T)$, with $\mu_n, n, p = \text{const}$. Here, it is improbable that the fixed parameters are truly constant, rather the implied assumption is that one mechanism comes to dominate the electronic properties. Conversely, if one of the models would fail to describe the data reasonably, it is unlikely that the underlying mechanism would play a dominant role. In reality, neither is one mechanism dominant across all samples and temperatures, nor can its influence be disregarded outright. The analysis suggests that hole localization plays an important role in $(\text{Ti}, \text{Zr}, \text{Hf})\text{Co}(\text{Sb}_{1-x}\text{Sn}_x)$, while not being the sole mechanism. As a contributing factor, a lower hole localization can explain why the thermoelectric power factor tends to improve with increasing Sn-contents for $x < 0.15$ in this material family.

To summarize, the main conclusions of this chapter are:

5 *P-type thin film $\text{Hf}_{0.5}\text{Zr}_{0.5}\text{CoSb}_{1-x}\text{Sn}_x$*

- The (Ti, Zr, Hf)Co(Sb_{1-x}Sn_x)-material family clearly exhibits bipolar behavior at low temperatures.
- In thin films Sn can partly precipitate into nano-inclusions, depending on sputter conditions. Here the sputter power sticks out as the most significant parameter.
- Hole localization can dominate electronic transport at low temperatures, especially for low-Sn-samples.

6 Controlled Intermixing Superlattices

6.1 Introduction

In composite materials, internal interfaces are used to introduce additional thermal barriers, either through implementation by nanostructuring techniques or by self-organizing properties that lead to natural microstructures. Because of the high interface density, the interaction of heat carrying phonons with internal boundary layers is a highly dominant aspect that depends critically on the make-up and topography of the interfacial area. Theoretical studies find orders of magnitude difference in the thermal boundary resistance depending on the interface quality. However, the experimental verification of these predictions poses difficult challenges both in the preparation and the examination of internal boundary layers. The formation of a boundary layer in most growth methods is fundamentally a random process, which can only indirectly be manipulated by the change of process parameters. Additionally, the interface by definition has an extension of only a few atomic planes, as it is fundamentally a two-dimensional entity that can be broadened to some degree by interdiffusion.

This study explores a new technique to grow superlattices with highly tunable interface qualities. In a HfNiSn/TiNiSn superlattice an additional interlayer of $\text{Ti}_{0.5}\text{Hf}_{0.5}\text{NiSn}$ is inserted at every material boundary. This interlayer serves as a highly tunable simulation of naturally occurring intermixing by diffusion. The interface quality is probed by X-ray diffraction and conclusively characterized by transmission electron microscopy on an atomic level. The thermal properties are studied by measuring the thermal conductivity by using the 3ω -technique.

Exemplary layer sequences with interlayers of different thicknesses are illustrated in Figure 6.1. For a one unit cell (UC) intermixing layer, the ratio of Hf to Ti in the boundary layer is 1-1, with an assumed random horizontal distribution. For an effective half unit cell intermixing layer, the intermixing layer consists of 0.25-0.75 and 0.75-0.25 of HfNiSn-TiNiSn and TiNiSn-HfNiSn, respectively. The superlattices with no interlayer correspond to pristine superlattices, which in case of TiNiSn/HfNiSn has little natural intermixing.

The relationship between bulk-like and interface related effects was inferred by comparing systems with differing interface densities at identical total system sizes. In Figure 6.1 this is exemplified by superlattices with a 6x6 and a 2x2 makeup, respectively. This key feature, the period length, is verified by X-ray diffraction (XRD). Additionally, satellite reflexes in the XRD-patterns can quantify the regularity of the superlattice structure itself and thus serve as a proxy for interface quality. This inferred interface quality is verified by transmission electron microscopy.

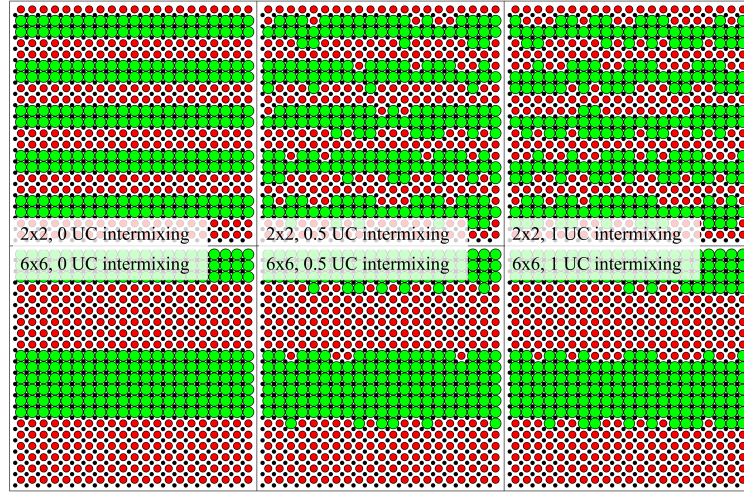


Figure 6.1: Illustration of superlattice design with varying unit cells (UC) of intermixing. The label indicates the period length in UC of TiNiSn and HfNiSn, respectively. Additionally the amount of added $\text{Ti}_{0.5}\text{Hf}_{0.5}\text{NiSn}$ in the interlayer is given. Black dots correspond to the NiSn framework common to both main layers, while green and red dots indicate Hf and Ti, respectively. The horizontal distribution was assumed to be random, preserving the average Hf/Ti-ratio in each layer.

6.2 Theoretical Model of Thermal Conductivity in TiNiSn Superlattices

6.2.1 Separating Layer and Interface Contribution

The thermal properties in the cross-plane direction can be expressed by a series circuit of thermal resistances given by the individual superlattice periods. Here the superlattice thermal resistance is given by

$$R_{SL} = \sum_i^N R_i \quad (6.1)$$

where N is the number of periods and R_i is the thermal resistance of a single period consisting of a thickness d_1 of TiNiSn, d_2 of HfNiSn and d_I of $\text{Ti}_{0.5}\text{Hf}_{0.5}\text{NiSn}$. From this thermal resistance, the thermal resistivity can be defined as an effective property of the system

$$\rho = \frac{1}{\kappa} = \frac{R_i}{d_1 + d_2 + d_I}, \quad (6.2)$$

where κ is the thermal conductivity.

6.2 Theoretical Model of Thermal Conductivity in TiNiSn Superlattices

We can define the bulk-like thermal resistivity assuming that every individual layer contributes to the overall transport with its respective bulk thermal resistivity,

$$\rho_{bulk} = \frac{\rho_1 d_1 + \rho_2 d_2 + \rho_I d_I}{d_1 + d_2 + d_I}, \quad (6.3)$$

where ρ_1 corresponds to the TiNiSn thermal resistivity, ρ_2 to HfNiSn, ρ_I to $\text{Ti}_{0.5}\text{Hf}_{0.5}\text{NiSn}$ and $d_{1/2/I}$ to the respective layer thicknesses.

However, the experimental resistivity is typically significantly larger than this theoretical value. One reason for this is that the use of the bulk thermal resistivity for thin layer sizes is not appropriate. The thermal resistivity derived from the Fourier law relies on the assumption of diffusive phonon transport. However, in structures where the Knudsen-number $Kn = \frac{l}{L}$, the ratio between mean free path and characteristic length, is larger than one, a significant portion of heat is transported ballistically [130, 131]. In this case, Alvarez et al. propose a correction factor ϕ based on extended reversible thermodynamics (ERT), the finite size term, which quantifies the deviation of the inner-layer thermal resistivity from the value expected by a purely diffusive description [132]

$$R'_i = (\rho_{bulk} + \phi)d, \quad (6.4)$$

with the period length $d = d_1 + d_2 + d_I$.

Additionally, every interface provides a fixed thermal boundary resistance. It is caused by a finite probability of transmission of heat carrying phonons across the interface. With the thermal boundary resistance per superlattice period R_{TBR} we get:

$$R_i = (\rho_{bulk} + \phi)d + R_{TBR}. \quad (6.5)$$

Experimentally, the interface related terms in this equation can be analyzed by subtracting ρ_{bulk} , which can be calculated from the known bulk thermal resistivities,

$$\rho_{intf} = \rho - \rho_{bulk} = \phi + \frac{R_{TBR}}{d}, \quad (6.6)$$

where ρ_{intf} expresses the excess thermal resistivity caused by the layer structure.

To quantify the influence of ρ_{intf} concisely, the interface material equivalent will be used in the remaining chapter

$$d_{equi} = \frac{\rho_{intf}}{\rho_{bulk}} \cdot d. \quad (6.7)$$

d_{equi} therefore expresses the amount of material that corresponds to the interface thermal resistance contribution of a single period, such that

$$R_i = \rho_{bulk} \cdot (d + d_{equi}). \quad (6.8)$$

This means that when the material equivalent equals the period length, both interface related and bulk-like terms contribute equally to thermal resistivity.

6.2.2 Estimating the Finite Size Term and Thermal Boundary Resistance for TiNiSn and HfNiSn Superlattices

With the known material parameters of TiNiSn and HfNiSn both the finite size term ϕ and the thermal boundary resistance R_{TBR} can be estimated. Here, the assumed interface quality is crucial for the resulting thermal boundary resistances. Consequently, a model developed by Alvarez et al. [83] is used, which can be easily adjusted for different interface topographies. With it, the order of magnitude of the superlattice thermal resistivity can be estimated in dependence of a specular parameter $p = 0$, which serves as a measure of interface quality.

It is based on a combination of the acoustic mismatch model (AMM) and the diffusive mismatch model (DMM), to include scatter mechanisms specific to different interface types. In this framework, interfaces are mainly characterized by their transmission coefficients τ , which can be calculated within AMM, τ_S , and in DMM, τ_D . It gives the fraction of phonons that are transmitted across an interface. In AMM, this transmission coefficient depends mainly on the acoustic impedances $Z = \rho_i v_i$, where i denotes the material and ρ_i and v_i correspond to the mass density and mean phonon velocity, respectively. For a given incidence angle θ_i and transmission angle θ_j , the transmission coefficient is then given by [71]:

$$\tau_{Sij} = \frac{4\rho_i v_i \rho_j v_j \cos\theta_i \cos\theta_j}{|\rho_j v_j \cos\theta_j + \rho_i v_i \cos\theta_i|}, \quad (6.9)$$

where i and j correspond to TiNiSn and HfNiSn and v_i is the respective Debye velocity. The Debye velocity is calculated from the longitudinal and transversal group velocities of the relevant acoustical branch, which are averaged over the first Brillouin-zone. Here, the phonon dispersion relation is based on DFT-calculations performed by G. Fiedler[133]. From the group velocities the Debye velocity can be calculated as

$$\frac{1}{v} = \sqrt[3]{\frac{1}{v_L^3} + 2 \cdot \frac{1}{v_T^3}}, \quad (6.10)$$

where v_L and v_T are the mean longitudinal and transversal velocities, respectively.

The transmission angle in equation 6.9 can be derived from the incident angle using Snell's law, which, under consideration of inelastic processes takes the form [71]

$$(C_i v_i)^{1/2} \sin\theta_i = (C_j v_j)^{1/2} \sin\theta_j \quad (6.11)$$

where C_i and C_j is the specific heat of material i and j , respectively.

The transmission coefficient in 6.9 gives the transition probability of a phonon of a given angle for well-prepared interfaces. It is especially useful for experiments at low temperatures, where the intrinsically longer characteristic phonon wavelength lowers the requirements on interface quality.

6.2 Theoretical Model of Thermal Conductivity in TiNiSn Superlattices

Analogously to the extreme case of near-perfect interfaces, the transmission coefficient can be calculated for high interface scattering rates. In this case the diffusive mismatch model is appropriate, which assumes 100% chance of scattering at the interface, which randomizes the propagation direction of every incoming phonon. Similar to AMM, the transition probability can be expressed as a function of the phonon propagation velocity and the specific heat [75]

$$\tau_{Dij} = \frac{C_j v_j}{C_i v_i + C_j v_j}. \quad (6.12)$$

While most realistic interfaces at room temperature are adequately described by equation 6.12, systems with high-quality interfaces can have a significant non-diffusive contribution. In this case the description improves from a combination of both extreme cases, in which the specularity parameter p weighs the two models against each other. Here, $p = 1$ corresponds to perfect interfaces, in which AMM is completely applicable, while $p = 0$ describes the fully diffusive case, which is given by DMM. The combination of equations 6.9 and 6.12 together with the specularity parameter yields the transmission function Γ_{ij}

$$\begin{aligned} \Gamma_{ij} &= p\Gamma_{Sij} + (1-p)\Gamma_{Dij} \\ &= p \cdot 2 \int \tau_{Sij}(\mu) \mu d\mu + (1-p) \int \tau_{Dij} \mu d\mu \end{aligned} \quad (6.13)$$

where $\mu = \cos\theta_i$ is used for the angular integration of the transmission coefficients. The transmission function gives the mean transmission probability of phonon coming from material i entering material j .

As in a superlattice, and interface of TiNiSn-HfNiSn is always paired with an HfNiSn-TiNiSn, a mean transmission function will be assumed

$$\Gamma = \frac{\Gamma_{ij} + \Gamma_{ji}}{2} \quad (6.14)$$

Figure 6.2 shows the estimated transmission function, with the key parameters used in the simulation given in table 6.1. Γ is significantly lower in the DMM case than for atomically flat interfaces in the AMM case. While this is true for most material combinations, it

	Debye velocity v_d (m/s)	Heat capacity C_i ($\cdot 10^6$ J/m ³ K)	Debye temperature θ_D (K)
Source	[133]	[134]	[134]
TiNiSn	3560	2.31	380.1
HfNiSn	3090	2.65	316.2

Table 6.1: Literature values used in the estimation of the effective interface thermal resistance. The Debye velocity has been calculated from the band structure simulations given in [133].

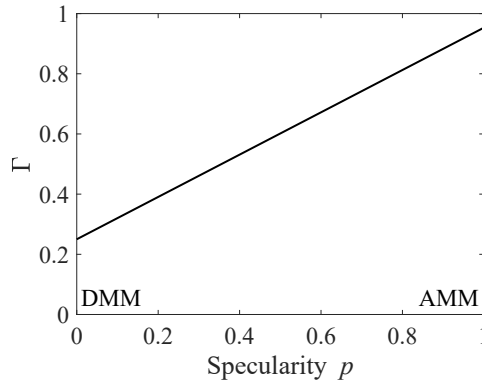


Figure 6.2: Mean transition function of a TiNiSn/HfNiSn interface. It gives the transmission probability of an incident phonon, averaged over all angles. The specularity parameter quantifies the interface quality, with one being a perfect plane and zero corresponding to 100% interface scattering probability. $p = 0$ is appropriately described by the diffusive mismatch model, DMM, while $p = 1$ corresponds to the acoustic mismatch model, AMM.

is particularly pronounced for TiNiSn/HfNiSn. In the pure AMM-case of $p = 1$, the transmission coefficient is as high as $\sim 95\%$, while it is $\sim 70\%$ for SiGe and $\sim 85\%$ for AlAs/GaAs [83]. This is likely due to the similar propagation velocities on TiNiSn/ HfNiSn, which are only different by 15% and the similar atomic masses of 225 g/mol and 356 g/mol for TiNiSn and HfNiSn respectively. While Hf and Ti have widely differing atomic masses, both compounds share Ni and Sn as common elements, which decreases mass contrast. In comparison, Ge has more than double the atomic mass than Si, with 72.6 g/mol vs 28.1 g/mol. Together with the difference in group velocities of close to 50%, this leads to a much higher acoustic contrast.

Because of the low acoustic contrast in TiNiSn/ HfNiSn, a decrease of specularity by interface quality deterioration should have a significant impact on thermal conductivity, as smooth interfaces constitute particularly ineffective thermal barriers. Therefore the difference in the diffusive DMM-like scatter mechanism and the specular AMM-like scatter mechanism is especially large.

This is amplified by the fact that the high transmissivity lowers phonon confinement within the individual layers. In the case of smooth TiNiSn/ HfNiSn layers with a transmission probability of $\sim 95\%$, the confinement is practically negligible. However, by fully diffusive scattering close to 75% of phonons are confined to a single layer, effectively increasing the base thermal resistivity. To quantify this phenomenon, an effective device size can be calculated. It corresponds the mean of length scales in a superlattice, weighted with the probability of phonons to be transmitted across the specific length. The share of phonons that are not transmitted across a single interface is given by $(1 - \Gamma)$ and their effective device length is L , which is the thickness of an individual layer. The share of phonons to transmit across a single interface and to be confined within the next layer

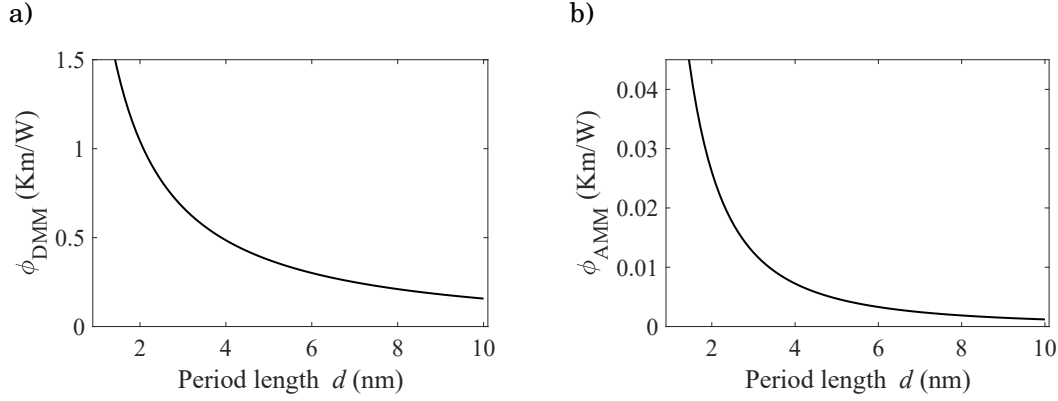


Figure 6.3: Finite size term in dependence of period length. It gives the increase in thermal resistivity caused by the partial phonon confinement within the superlattice.

a) Finite size term within the diffusive mismatch model (DMM), i.e. assuming 100% diffusive interface interaction. It ranges from 15% at 10 nm period length to 145% at 1.5 nm.

b) Finite size term calculated with the acoustic mismatch model (AMM). The correction of the thermal resistivity stays within few percent of the bulk value.

consequently is given by $(1 - \Gamma)\Gamma$, with the device size $2L$. For the general case of the n -th layer the probability becomes $(1 - \Gamma)\Gamma^{n-1}$. Here the probability of a phonon to be transmitted to the layer n is Γ^{n-1} and the probability for it to be confined in the n -th layer is $(1 - \Gamma)$. For the whole system we can therefore define an average device size as

$$L_{\text{eff}} = \sum_{n=1}^{N-1} (1 - \Gamma)\Gamma^{n-1}L_n + \Gamma^{N-1}L_N, \quad (6.15)$$

where L is the individual layer thickness, $L_n = n \cdot L$ and N is the number of individual layers. The last term $\Gamma^{N-1}L_N$ takes into account that all phonons are confined within the overall system boundaries and that therefore the device size cannot exceed L_N . As each period contains two individual layers, L corresponds to half of the period length and N corresponds to double the number of periods.

This effective system size is used in the extended irreversible thermodynamics framework developed by Alvarez et al. to estimate the finite size term [135]

$$\phi_i = \rho_{\text{bulk}} \left(\frac{2\pi l_i^2}{L_{\text{eff}}^2} \left[\sqrt{1 + \left(\frac{2\pi l_i}{L_{\text{eff}}} \right)^2} - 1 \right]^{-1} - 1 \right). \quad (6.16)$$

Here the mean free path is calculated from the bulk thermal conductivities using the Debye-Callaway model [136, 137]

$$l_i = \frac{k_B \rho_i}{2\pi^2 v_D^2} \left(\frac{k_B T}{\hbar} \right)^3 \int_0^{\theta_D/T} \frac{x^4 e^x}{(e^x - 1)^2} dx, \quad (6.17)$$

with the Boltzmann-constant k_B , the thermal resistivity ρ_i , the Debye velocity v_D , the temperature T , the reduced Planck constant \hbar and the Debye-temperature θ_D . For the material parameters θ_D , C_i/C_j and for the group velocities, the literature values given in table 6.1 are used.

As expected, the finite size term corresponds to a significant contribution in the case of dominant diffusive interface scattering, Figure 6.3a. In this case, it reaches a value of around 1 Km/W for a period length of 2 nm. This corresponds to roughly four times the mean bulk thermal resistivity. This means that in a superlattice of period length 2 nm with completely diffusive interface interaction, the inner-layer thermal resistivity is increased 5-fold compared to bulk. Towards smaller period length the finite size contribution drops, down to 40% of bulk resistivity for a 10 nm period length superlattice.

In the AMM case, Figure 6.3b, the finite size contribution stays lower than 20% of the bulk thermal resistivities, even for low period length. For larger period length samples, the contribution quickly diminishes further. In TiNiSn/HfNiSn superlattices with specular interfaces the inner-layer resistivity is therefore clearly dominated by bulk-like effects and the confinement plays a negligible role. In general the contribution of the finite size term is 15-20 times smaller in the AMM case compared to the DMM case below 5 nm.

Additional to the phonon confinement, the only partial transmission of heat carrying phonons across an interface leads to direct thermal resistance. The contribution can be directly quantified with the transmission coefficient and the mean amount of heat that is carried per phonon. Under a density of states expressed by the Debye approximation, Swartz et al. give the following term for the thermal boundary resistance [75]

$$R_{ij} = \frac{4\pi^2 \hbar^3 v_i}{k_B \Gamma_{ij} T^3} \frac{1}{\int_0^{\theta_D/T} x^4 e^x / (e^x - 1)^2 dx}, \quad (6.18)$$

with the Debye-temperature θ_D , the Debye-velocity v_i , the Boltzmann-constant k_B and the reduced Planck-constant \hbar . The equation expresses the thermal resistance associated with a transmission from material i to material j. While in general the direction of transmission plays a role, in TiNiSn/HfNiSn $R_{ij} \approx R_{ji}$, because of their similar material properties. For this reason and because in all investigated systems the number of TiNiSn-HfNiSn interfaces is equal to the HfNiSn-TiNiSn interfaces, a mean thermal boundary resistance is used for the remaining chapter

$$R_{TBR} = \frac{R_{ij} + R_{ji}}{2} - \rho_i \cdot l_i - \rho_j \cdot l_j, \quad (6.19)$$

Here the thermal boundary resistance is additionally corrected by a contribution of a layer l_i or l_j , respectively, adjacent to the interface, which is implicitly included in equation 6.18.

6.2 Theoretical Model of Thermal Conductivity in TiNiSn Superlattices

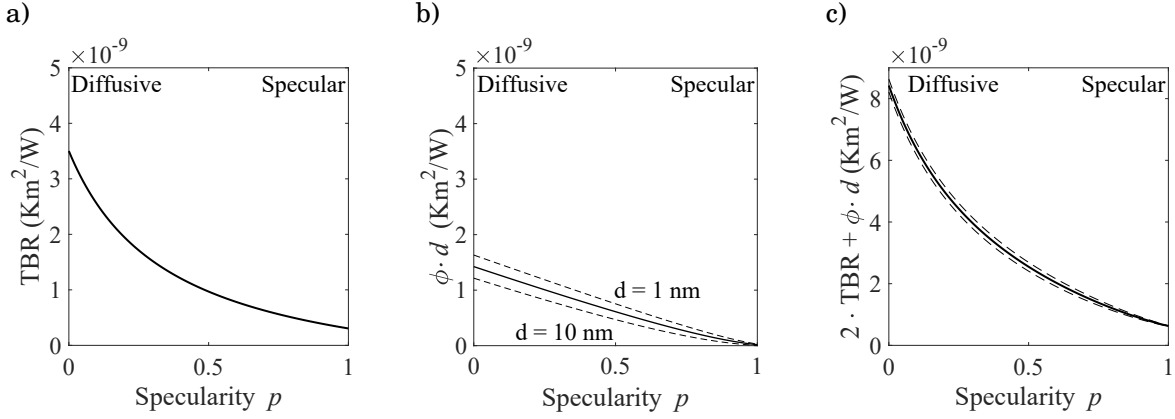


Figure 6.4: Contributions to effective interface resistance.

a) Thermal boundary resistance of a TiNiSn/HfNiSn interface in dependence of the specularity. $p = 0$ corresponds to the fully diffusive and $p = 1$ corresponds to the fully specular case.

b) Thermal resistance contribution of the finite size term per superlattice period. The broken lines correspond to period lengths of 10 nm and 1 nm, respectively, while the solid line corresponds to the mean value

c) Sum of the contributions a) and b) to the thermal resistance per period length. The broken lines correspond to period lengths 1 nm and 10 nm.

As with the finite size term, the thermal boundary resistance is significantly larger in the diffusive case than in the specular case, Figure 6.4a. Both values differ by roughly an order of magnitude with the TBR in the DMM case being $3.9 \cdot 10^{-9} \text{ Km}^2/\text{W}$ and $0.3 \cdot 10^{-9} \text{ Km}^2/\text{W}$ in the AMM case. For all interface types, the influence of the thermal boundary resistance dominates the thermal resistance of a single period over the influence of the finite size term, Figure 6.4b. The contribution of a single interface is roughly 2.5 larger than the inner-layer resistivity increase by the finite size term for the diffusive case and 17 times larger for the specular case. The finite size term in general depends on the period length, however, as both ϕ_{DMM} and ϕ_{AMM} approximately follow a $\propto 1/d$ behavior, their contribution per period length ϕd is roughly constant. In consequence, this is also true for the effective interface resistance, which is the sum of inner-layer and TBR contributions given in Figure 6.4c,

$$R_{intf} = 2R_{TBR} + \phi \cdot d, \quad (6.20)$$

as two interfaces per period contribute a TBR, the finite size contribution $\phi \cdot d$ is comparatively small.

6.3 Sample Preparation

6.3.1 Target Fabrication

For the preparation of the samples a magnetron sputter deposition technique was chosen. This growth method provides a reasonable deposition rate combined with a high controllability of the film morphology. For magnetron sputtering, compact, homogeneous discs of the deposition material are needed as the target for ion bombardment. For the deposition process three targets of HfNiSn, TiNiSn and $\text{Ti}_{0.5}\text{Hf}_{0.5}\text{NiSn}$ were manufactured. However, the fabrication of targets from these materials is challenging for multiple reasons. The compounds exhibit large expansion coefficient, which means that when they are quenched after an arc-melting process, they tend to crack. On the other hand, the constituting elements Ti, Hf, Ni, Sn exhibit widely varying melting points with 2233 °C, 1668 °C, 1455 °C and 232 °C, respectively. This means that while an increased temperature increases the resulting target density, it also produces a liquid, highly mobile Sn-phase in a sintering process and thus potentially target inhomogeneities. To address these challenges, the target material is pre-reacted in a arc melting step producing TiNiSn and HfNiSn. The resulting base material is ground to a powder for subsequent compacting. These first two steps were performed by the HMW Hauner GmbH & Co. KG. This base powder is then sintered at 1000 °C, well below the melting point of the compound, to compact targets in a spark plasma sintering (SPS) step. Here, the powder is pressed while being heated by a pulsed current, following a pre-set temperature profile.

To assess the target homogeneity, energy dispersive X-ray spectroscopy (EDX) was performed using an FEI Helios Nanolab 600i scanning electron microscope setup. In Figure 6.5a) each data point corresponds to the mean content of the constituent elements on a $100 \times 100 \mu\text{m}$ area, with a vertical spacing of 0.2 mm between the sample area. As a comparison, the lateral variation is recorded in Figure 6.5b) for 25 equal frames at random horizontal positions around the target center.

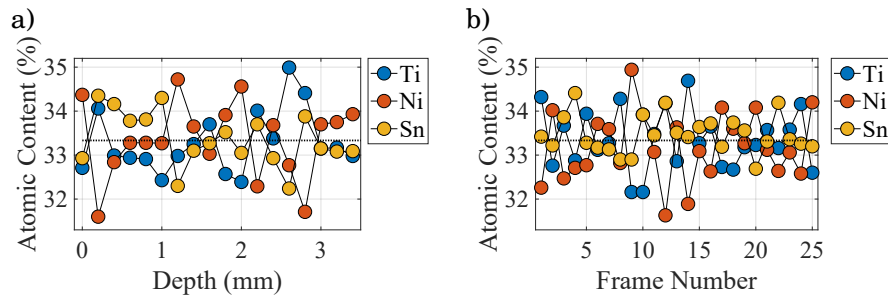


Figure 6.5: Composition homogeneity of the sputter targets as measured by energy dispersive X-ray spectroscopy (EDX). The values correspond to mean composition of $100 \times 100 \mu\text{m}$ windows that are distributed
a) at different target depths and
b) for random frames at equal depth around the center of the target.

Both plots exhibit similar scattering, suggesting the absence of a overall composition gradient. The mean composition is close to the ideal 1-1-1, with Ti, $33.40 \pm 0.77\%$, Ni, $33.06 \pm 0.88\%$ and Sn, $33.54 \pm 0.58\%$. The error gives the standard deviation over the measurement set, which is compatible with the typical error of EDX-measurements.

6.3.2 Thin films

From the sintered targets, thin films were grown on (001)-single crystalline MgO substrates that were provided by CrysTec GmbH. The optimum growth temperature of 550°C was determined in a previous study [138]. The temperature provides reasonable crystalline quality, while resulting in relatively smooth surface topographies. Additionally, it was demonstrated by TEM that the relatively low temperature limits interdiffusion and thus leads to clearly defined superlattices.

The flow of Argon gas is chosen to attain a minimal pressure, while still providing stable plasma conditions. In a pre-study a low sputter pressure was found to be beneficial to attain narrower rocking curves and therefore higher crystalline quality.

Sample Design

The overall sample structure (Figure 6.6) was designed to achieve a reliable insulating barrier and high quality crystal growth. Additional to the film of interest, the sample is composed of two buffer layers, an AlO_x insulating spacer layer, a SiO_2/MgO insulating barrier and the 3ω heater structure

This gold heater structure is manufactured on top of an additional MgO/ SiO_2 insulating layer. It consists of three 10 nm thick MgO layers inside a SiO_2 matrix. The MgO layers proved to be particularly effective in preventing a dielectric breakdown between film of interest and measurement structure, as well as mechanical penetration by surface features. This MgO/ SiO_2 -barrier is grown on top of an AlO_x insulating spacer layer. The film of interest underneath the insulating layer consists of alternating layers of TiNiSn and HfNiSn. The total thickness of all films is around 900 nm, which leads to, depending on period thickness, 200-800 individual layers. $\text{Ti}_{0.5}\text{Hf}_{0.5}\text{NiSn}$ acts as an interlayer separating the main components with a thickness of 0.3 and 0.6 nm, respectively. This makes the share of the $\text{Ti}_{0.5}\text{Hf}_{0.5}\text{NiSn}$ interlayer 50% and 25% for the lowest period length of 2 by 2 unit cells (UC), respectively and 12.5% and 6.3% for the largest period length of 8 by 8 UC.

To improve the growth characteristics, the film of interest is deposited on a Vanadium

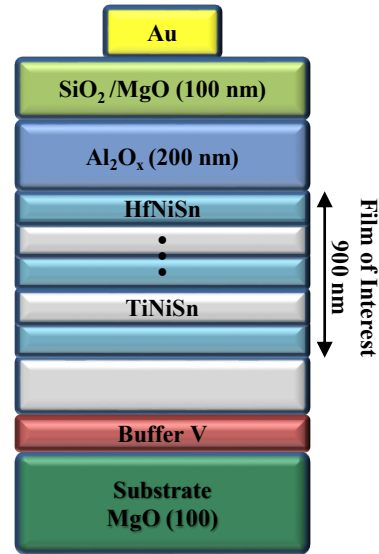


Figure 6.6:
Basic sample design

and a TiNiSn buffer layer, both of which have a thickness of around 20 nm. Vanadium exhibits a hetero-epitaxial growth on the (001)-MgO plane, leading to good crystalline quality and smooth surface morphology. This is despite of the large apparent lattice mismatch between MgO and V, with lattice constants of 4.21 Å and 3.024 Å [139]. The reason for the growth compatibility is that the vanadium planes are rotated by 45°, which leads to a ratio of the lattice spacings in the relevant directions of almost exactly 2-1, which makes the effective lattice mismatch

$$\frac{2 \cdot a_V}{\sqrt{2} \cdot a_{MgO}} - 1 = 1.58\%. \quad (6.21)$$

Additionally to relaxing the lattice mismatch, vanadium can act as a barrier that prevents Ti/Hf depletion at the substrate-film interface. Indications of relevant depletion mechanisms were found for thin metal films on oxide layers [140] and confirmed for the TiNiSn-system on MgO [124].

6.4 Structural Characterization

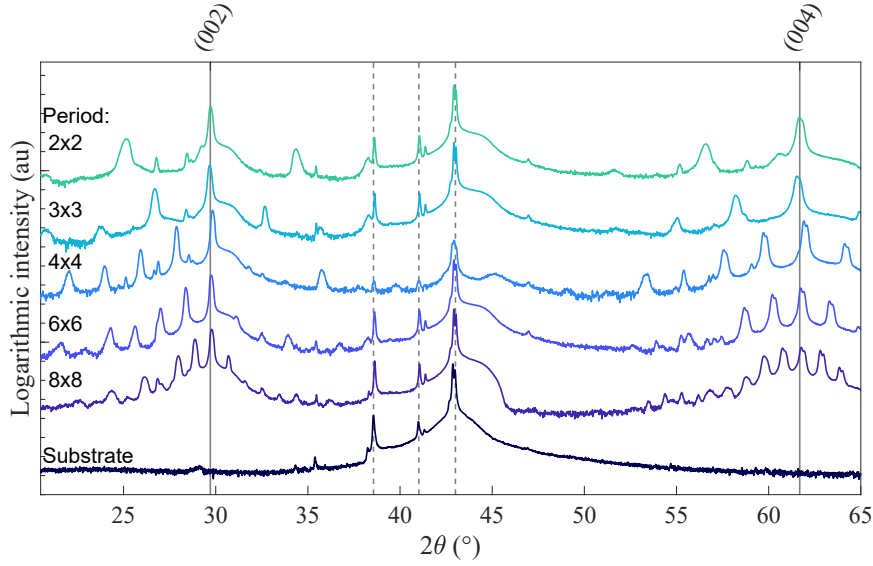
6.4.1 Crystalline Quality by X-ray diffraction

Figure 6.7a show the XRD-patterns of pristine superlattices of different period thicknesses. They demonstrate the intended (002)-growth with a high specificity regarding growth-direction. The crystal quality, measured by their rocking curves, is consistent over the sample series, with rocking curve widths varying between 0.5-0.9°. No systematic trend over time is visible, which provides comparability of samples within the sample series. In accordance with the inverse dependence of satellite spacing and period length, the satellite density increases from the 2x2 to the 8x8 superlattice. However, for all superlattices multiple clear satellites are visible, enabling the precise determination of period length. For this analysis CADEM [141] was used, an algorithm which reconstructs XRD-patterns of superlattice sequences, which can be defined layer by layer. Here also different interface qualities can be considered by inserting composition gradients at the boundary layers.

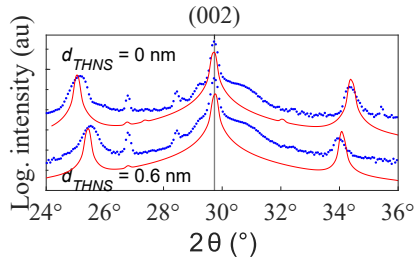
In Figure 6.7b a superlattice with a period of two unit cells TiNiSn by two unit cells HfNiSn is simulated and compared to corresponding experimental diffraction patterns. Two different curves are displayed, corresponding to different interlayer thicknesses. The upper curve shows a pristine superlattice, while in the lower one, one unit cell of $Ti_{0.5}Hf_{0.5}NiSn$ is inserted at the boundary. The respective simulations are adapted accordingly. Especially the satellite around 34° exhibits significant attenuation by the lowered interface definition compared to the pristine superlattice.

This effect is much less pronounced in the 6x6 superlattice, an analogous satellite pattern of which is displayed in Figure 6.7c. Here, more satellites up to an order of 3 are clearly visible. However the difference between the intermixing and the pristine superlattice is negligible. This is likely because of the lower share of the intermixing layer on total volume compared to the previous sample. While in the 2x2-superlattice the intermixing

a)



b)



c)

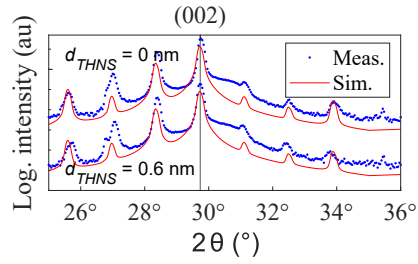


Figure 6.7: Characterization of superlattice samples by X-ray diffraction.

- a) Overview over XRD scans of smooth superlattices with different period lengths.
- b) Experiment and simulation of a smooth superlattice and a superlattice with an artificial intermixing layer of 1 unit cells, i.e. 0.6 nm. The period length is 2x2 UC.
- c) Experimental and simulated XRD patterns of 6x6 superlattices of smooth and artificial intermixing superlattices.

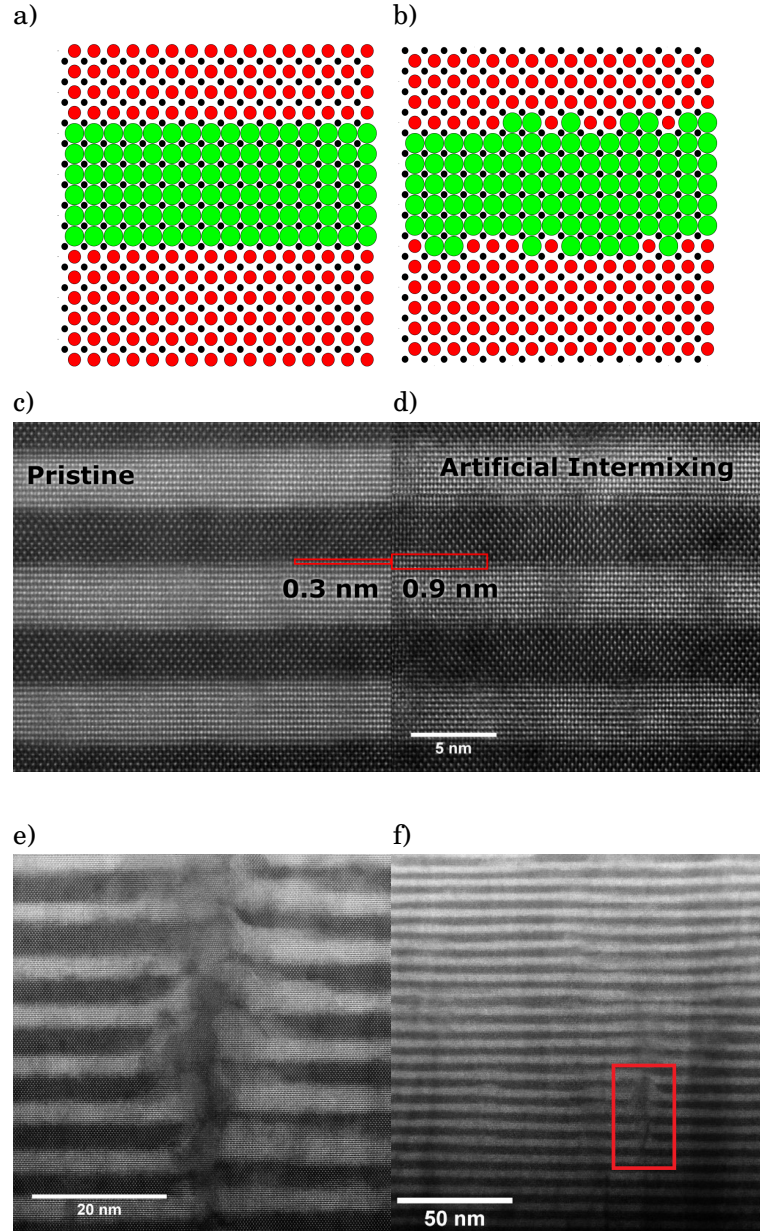


Figure 6.8: a) and b) Illustration of the intended superlattice design of a pristine superlattice and a 1 UC artificial intermixing layer superlattice, respectively. In between the main layers of TiNiSn and HfNiSn, one UC of $\text{Ti}_{0.5}\text{Hf}_{0.5}\text{NiSn}$ is deposited.
c) and d) High resolution transmission electron microscopy (HR-TEM) image of a 6x6 superlattice with pristine interfaces and 1 UC intermixing, respectively. The natural intermixing layer of around 0.3 nm and 0.9 nm is marked with a red box.
e) Disordered domain that separates ordered columns.
f) Disordered inclusion that is completely enclosed in the superlattice matrix.

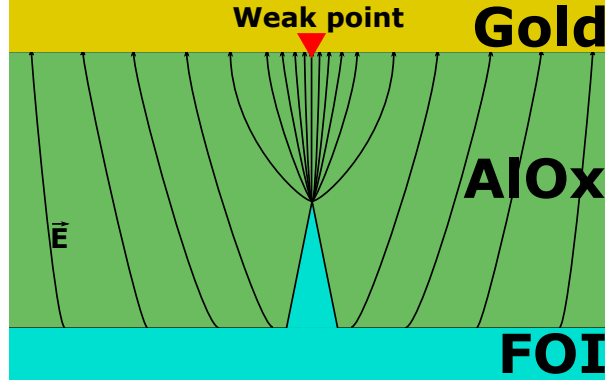


Figure 6.9: Illustration of the electrical field configuration in the insulating barrier with the introduction of spike-like features. The sharp edge of the features lead to a strong accumulation of field lines and thus high electrical fields.

layer makes up 50% of the overall system it is lower than 17% for the 6x6 superlattice. Consequently, for the sample series as a whole, X-ray diffraction data can only give an indication of the efficacy of the interface manipulation method. Therefore, additionally high resolution transmission electron microscopy has been performed to characterize the boundary layers of exemplary samples.

6.4.2 Transmission Electron Microscopy

For interface characterization, high-resolution scanning transmission electron microscopy (HAADF HR-STEM) was performed by M. Trapp¹ on a JEOL JEM ARM 200F equipped with a Cs-corrected condenser system, operated at an acceleration voltage of 200 keV. In accordance with a previous HR-TEM study [142] on TiNiSn/HfNiSn structures grown by a similar procedure, the structures exhibit a well-defined layer structure in the majority of the sample volume. The material forms columnar grains with a diameter of 100-200 nm that stretch typically over the entire film thickness. These columns are separated by narrow disordered domains, as depicted in Figure 6.8e. While the bulk of the material exhibits the intended nanostructure, small disordered inclusions are sparsely distributed through the sample volume (Figure 6.8f). As can be seen in Figure 6.8c, the intrinsic intermixing layer in a pristine TiNiSn/HfNiSn superlattice is confined to 0.3 nm, corresponding to half a unit cell (UC). In Figure 6.8d, the same superlattice design is modified with an additional 0.6 nm Ti_{0.5}Hf_{0.5}NiSn interlayer at each interface. Consequently, the boundary layer is extended to 0.9 nm while the overall sample characteristics remain similar.

Overall, the TEM-study verifies the growth of superlattices with tunable interface qualities and otherwise comparable properties.

¹Institute of Applied Geosciences, Darmstadt University of Technology, Schnitzspahnstrasse 9, 64287 Darmstadt, Germany

6.4.3 Surface Morphology

While the internal structure and crystalline properties are consistent over the sample series, the surface morphology exhibits a large variation between samples. It is dominated by particle-like features, which can vary in form, number and overall dimensions. These partly spike-shaped protrusions can interfere with the 3ω -thermal conductivity measurement by penetrating the insulating layer and shorting the 3ω -heater structures. Figure 6.9 illustrates how the sharp edges can weaken the insulating barrier by lowering the local breakdown voltage. As a consequence, the insulating barriers are broken by both types of particles in Figure 6.10a and b. In a the particles are sparse but their height exceeds the insulator thickness of $0.2\ \mu\text{m}$ significantly. The particles in b, on the other hand, are distributed much more densely, but are comparable in height with the AlO_x layer. Figure 6.10c and d illustrate the correlation between particle height and film deposition temperature. In c the particles are ordered according to their growth date, potentially revealing effects related to target aging. While there is a weak trend with time, it is superseded with a correlated trend in substrate temperature. This variation in substrate

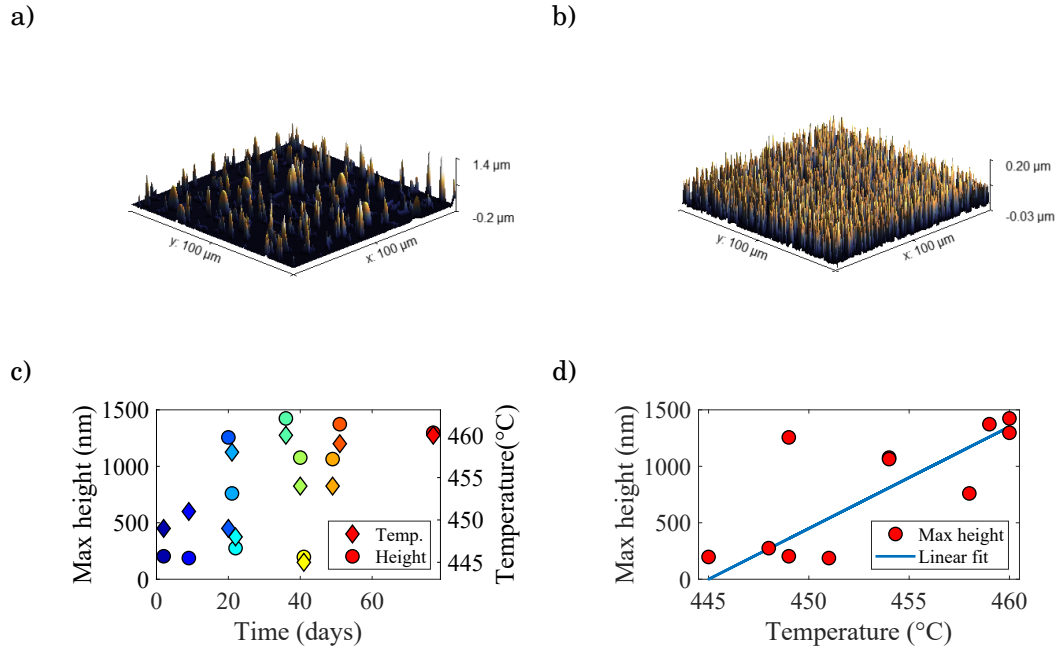


Figure 6.10:

- a/b) Exemplary AFM measurements of two samples. The height and coverage of precipitate particles differ significantly between samples.
- c) The maximum height of precipitate particles and deposition temperature as a function of creation date.
- d) Correlation plot of maximum height of precipitate particles and deposition temperature.

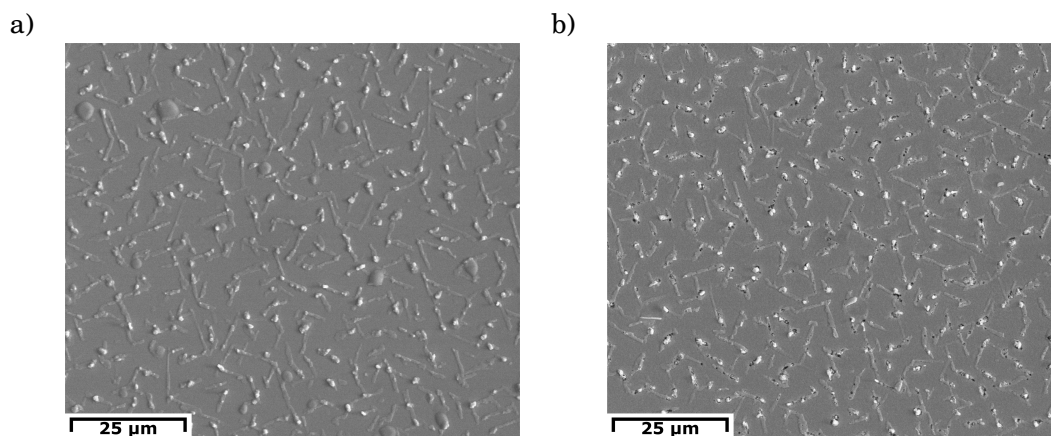


Figure 6.11:

- a) Exemplary SEM-image of a sample surface. The surface morphology is dominated by round, relatively flat and elongated, partly spike-shaped particles. The elongated particles tend to orient along few main directions.
- b) The same sample after treatment with NaOH. While the round particles are effectively removed, the elongated particles are much less affected.

temperature is likely caused by varying radiative coupling between the constant heater temperature and the substrate holder. As the back side of the substrate holder, which is coupled the closest to the heater, is progressively covered with target material, its surface properties are prone to change over time. To eliminate this variation, the sample temperature was monitored separately by probing the thermal radiation emitted by the substrate and adjusted to 440 °C- 445 °C.

The particles on a typical surface, Figure 6.11a, can be divided by their morphology into two subcategories. The first category consists of elongated particles with sharp, spike-like features that are largely oriented along few main directions. The other type of particle are broader, round particles, which are much less high. The round particles are sensitive to NaOH and weak acids, while the elongated ones and the main film withstand both widely intact, Figure 6.11b. Also polishing by ion etching at a grazing angle proves to be ineffective.

The difference in etching resistance between the different particle types raises the question of their chemical composition. To evaluate compositional makeup of the sample surfaces energy-dispersive X-ray spectroscopy (EDX) was used, employing a FEI Helios NanoLab 600i scanning electron microscope at a 20 kV accelerating voltage. Figure 6.12a reveals a strong Sn-accumulation at the round particles and a weaker but still significant accumulation at the elongated particles. Looking at the quantitative data, Table 6.12b, a relatively weak additional Ni-accumulation is noticeable for the elongated particles. Here, the data can only indicate the composition of the particles, as their limited thickness and irregular shape can distort the measured composition. Especially, a significant contribution from the main-film has to be considered, as a the electron beam penetrates the

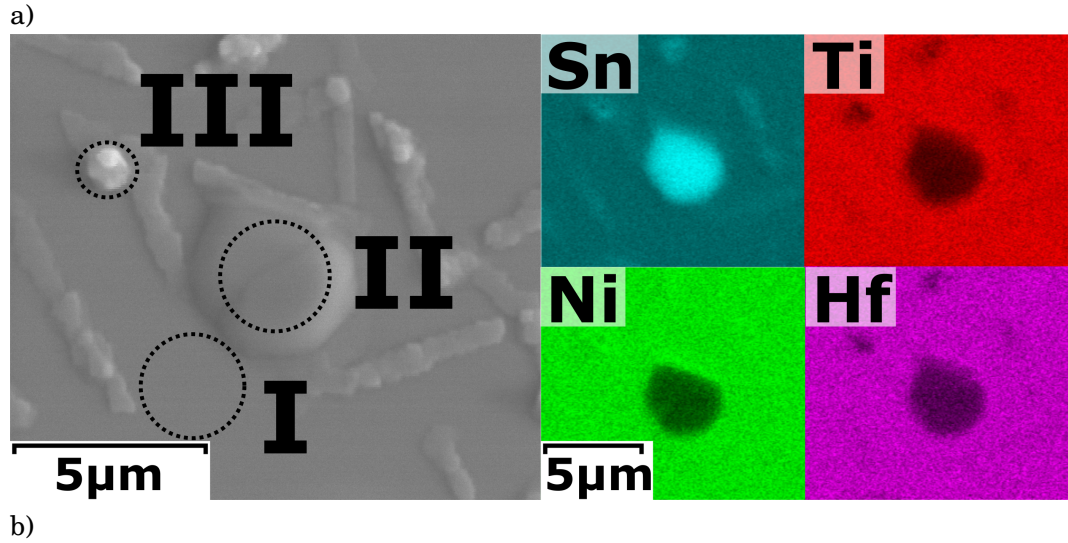


Figure 6.12: Compositional analysis of an exemplary sample surface.

a) SEM image with the quantitatively analyzed areas being marked with I, II, and III, respectively. On the right side composition maps of the same area are shown of all four components. The composition maps are calculated based on energy-dispersive X-ray (EDX) spectroscopy measurements.

b) Quantitative breakdown of the main areas investigated in the analysis. Here I corresponds to a baseline measurement of the main film, II to a circular particle and III to an spike-feature of an elongated particle. The signal of measurement II and III includes a contribution from the main film, as the probing electron beam partly penetrates the particles. Therefore the measured composition only reflects the real particle composition partly.

particles to varying degrees and reaches into the main film. Nevertheless, a ratio of more than 5 to 1 of Sn to Ni in the round particles indicate a strong Sn excess. Indeed the samples grown from stoichiometric targets exhibit a significant Sn-surplus, as measured by EDX and independently verified by mass spectroscopy. The mass spectroscopy measurements were performed in the Karlsruhe Institute of Technology by the group of Prof. Dr. Hans Jürgen Seifert. The consequent position in the phase diagram, Figure 6.13a, suggests the possible formation of an elemental Sn-phase and Ni_3Sn_4 . Sn-phases explain the chemical resistance characteristics of the round particles, as Sn exhibits a typical

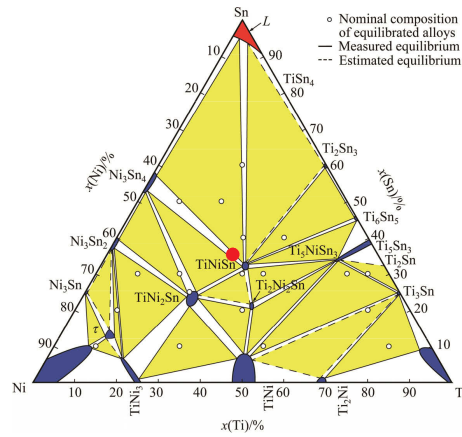


Figure 6.13: Position in the TiNiSn phase diagram of the investigated samples. The position suggests elemental Sn and Ni_3Sn_4 as the most likely precipitates. TiNiSn phase diagram reprinted from Transactions of Nonferrous Metals Society of China, Volume 28, Yonggang Meng WANG, Hua-shan LIU, Ge-mei CAI and Zhanpeng JIN, measurement of phase equilibria in Ti-Ni-Sn system, pages 819–828, Copyright 2018 with permission from Elsevier. [143].

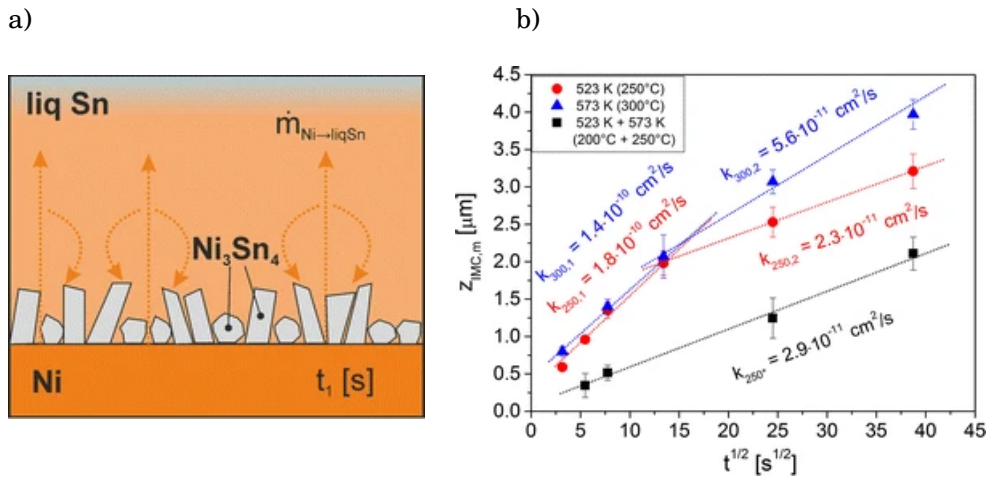


Figure 6.14: Typical Ni_3Sn_4 growth characteristics.

a) Needle like morphology that forms on a Ni-Sn boundary layer.

b) Feature height that shows a clear dependence on growth temperature for long growth times.

Reprinted by permission from Springer Nature Customer Service Centre GmbH: Springer Nature

Lis, Adrian, Christoph Kenel, and Christian Leinenbach. 2016. "Characteristics of Reactive Ni_3Sn_4 Formation and Growth in Ni-Sn Interlayer Systems." Metallurgical and Materials Transactions A 47 (6): 2596–2608. [144]

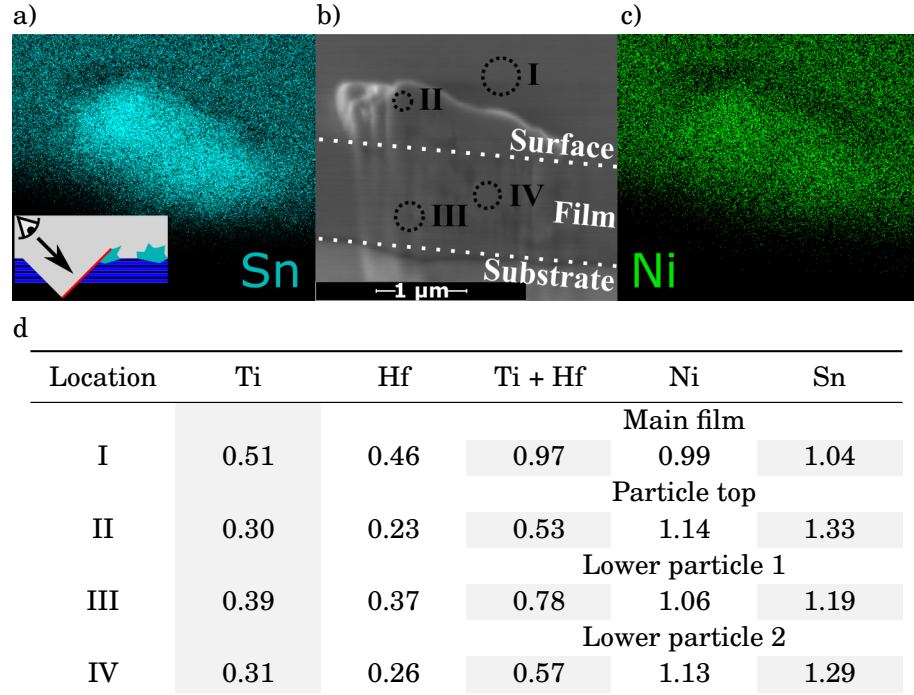


Figure 6.15: SEM (b) and composition maps (a and c) from EDX measurements (a,c) on a wedge-cut sample. In the investigated area a cross-sectional cut is prepared in-situ via focused ion-beam etching.

d) Quantitative analysis of the four areas I, II, III and IV. The composition has a contribution from the main film that depends on the local particle thickness.

sensitivity towards treatment with NaOH. The elongated particles, on the other hand, coincide with the typical morphology of Ni_3Sn_4 -particles. As shown in Figure 6.14a, Ni_3Sn_4 tends to form needle-like crystallites. Here Lis et al. found a characteristic link of feature size with growth temperature, Figure 6.14b, which coincides with the observations in the investigated sample series.

While both particles appear as a surface effect, the question remains, how far they stretch into (Hf,Ti)NiSn-matrix. In order to evaluate the degree of inclusion of the particles into the main film, an area of an exemplary sample was modified using a focused ion beam technique. A wedge-shaped trench was cut, passing through several particles, revealing their cross-section for examination by SEM and EDX. The elongated particle show the expected accumulation of Sn and a weaker accumulation of Ni. The particle is localized mostly on the sample surface. However, it stretches into the main film to some degree. The round particles, on the other hand, only exhibit a Sn-accumulation and are localized exclusively on the surface. To correct the composition variation in the thin films, the targets were adapted to reach a closer agreement of the sputtered thin films with the 1-1-1 composition of (Hf,Ti)-Ni-Sn, Figure 6.16c. Here special care was taken

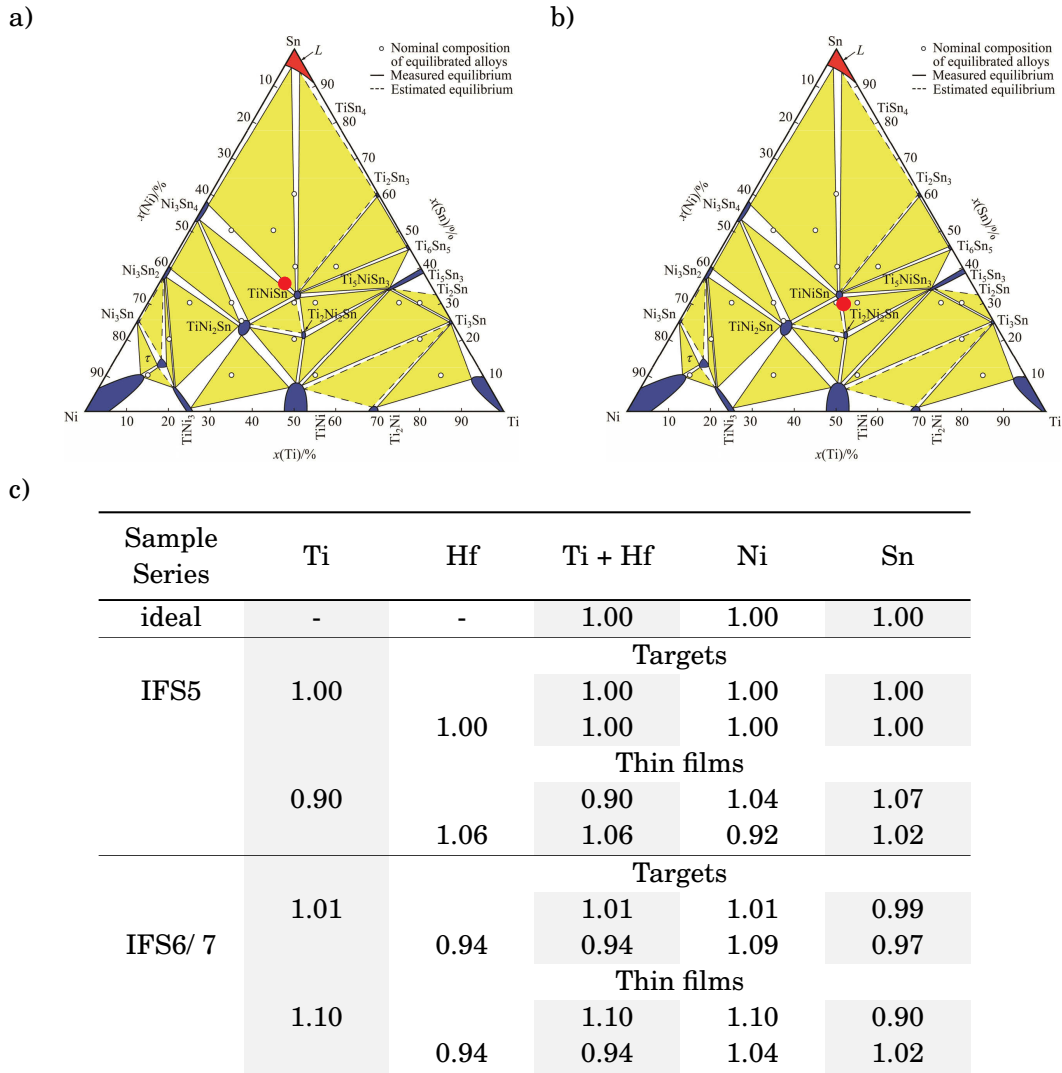


Figure 6.16: Position of the thin film samples in the TiNiSn phase diagram grown from a stoichiometric target (a) and a target with adapted composition (b). The red dot marks the realized composition, respectively. The adapted target composition moves the samples to a more Ni-rich area of the phase-diagram, effectively reducing the content of excess Sn.

c) shows quantitative data on target and thin film composition, respectively, for the first and subsequent sample series, interface series 5, 6, and 7 (IFS5, IFS6 and IFS7)

The TiNiSn phase diagram is reprinted from Transactions of Nonferrous Metals Society of China, Volume 28, Yonggang Meng WANG, Hua-shan LIU, Ge-mei CAI and Zhanpeng JIN, measurement of phase equilibria in Ti-Ni-Sn system, pages 819–828, Copyright 2018 with permission from Elsevier. [143].

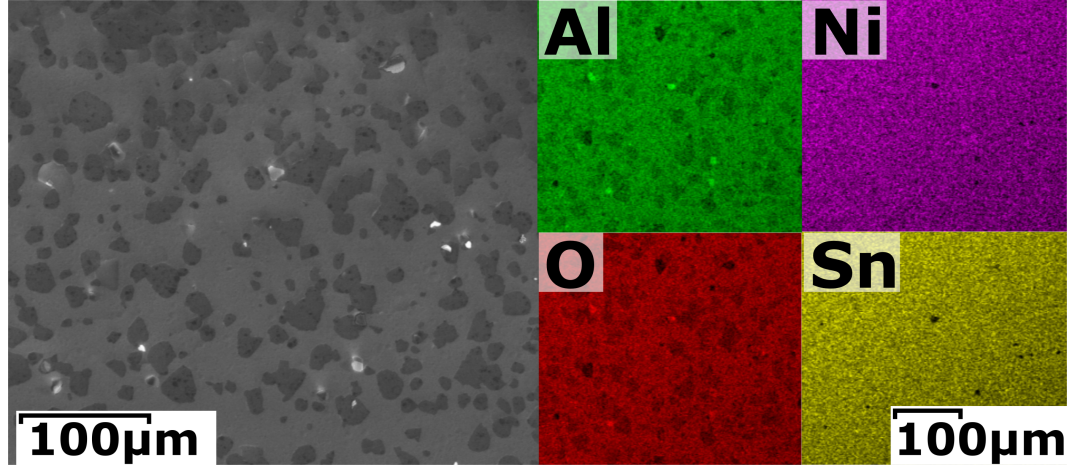


Figure 6.17: SEM image and compositional maps of a faulty AlO_x -barrier. The elemental distributions reveal inhomogeneities in Al and O, while the Sn and Ni distribution is mostly homogeneous.

to inhibit the formation of spike-like Ni_3Sn_4 -features. The realized composition is moved further towards the Ni-rich section of the phase diagram. While this change in composition reduced overall density and height of particles, precipitation at the sample surfaces still occur to varying degrees. These remaining particles made a further optimization of the used insulating barrier necessary.

6.4.4 AlO_x -layer Optimization

For the AlO_x deposition process a reactive sputtering procedure was chosen, which allows to use an aluminum metal target rather than insulating AlO_x . Metal as a target material prevents build-up of charge on the target surface and a better heat management, due to its intrinsically higher thermal conductivity. Additionally, metals exhibit a better adhesion to the relevant $\text{TiNiSn}/\text{HfNiSn}$ surfaces than corresponding oxides, leading to a more uniform, reliable insulating layer. During the sputtering process, sputtered Al and O_2 that is mixed into the working gas medium react to aluminum oxide.

However, the process parameters in reactive sputtering have to be carefully chosen to attain adequate insulating layers. Similar to sputtering in a pure argon atmosphere, the sputter pressure, the growth temperature, target-substrate distance and sputter power have to be considered. Additionally, however, the fraction of oxygen on the working gas medium plays a role, as well as the overall gas exchange rate. In fact, the morphology of the resulting AlO_x -film depends critically on the sputter conditions, with different possible growth regimes.

An example of a faulty AlO_x -insulating layer is shown in Figure 6.17. A SEM-image of a clearly discontinuous film is shown alongside compositional maps. The Ni- and Sn-maps suggest a continuous film underneath the insulating layer, while both Al and O reflect the irregular surface features apparent from the SEM-image. Because of the limited thick-

ness of the AlO_x -layer of around 200 nm no quantitative analysis is possible, however, the formation of domains with varying compositions is evident.

The shift in growth behavior of the presented example was caused by a change in overall working medium flow. Other process parameters like the sputter pressure, the oxygen-argon ratio, sputter power, etc, were kept constant, while the pump driving the gas exchange provided less turn-over due to mechanical aging. Due to the diminished flow, the reactive environment in the deposition process was changed, ultimately leading to a different growth regime.

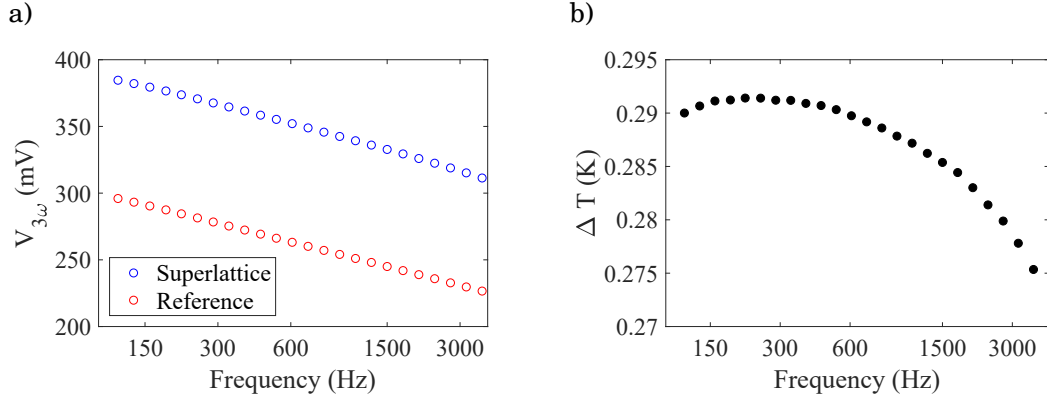


Figure 6.18: Raw signals associated with the 3ω -technique for two exemplary samples. The x-axis is spaced logarithmically to accommodate to the typical $\ln(2\omega)$ -dependence.

a) Third harmonic of the voltage drop across a heater structure caused by an oscillating current for a superlattice sample (blue) and a reference sample (red).

b) Difference in the temperature oscillations calculated from the voltages in a).

6.5 Experimental Results

6.5.1 The 3ω -Signal of Superlattices

To verify the theoretically estimated thermal boundary resistances, superlattices of TiNiSn/ HfNiSn with period lengths of 2-10 nm have been grown with 0, 0.5 UC and 1 UC artificial intermixing, respectively. While their layer sequence varies, their overall thickness is kept equal. Their thermal conductivity has been determined by measuring their 3ω signal and comparing it with a corresponding reference sample. Figure 6.18 shows the 3ω signals of a 3.6 nm TiNiSn and 3.6 nm HfNiSn superlattice with 1 UC intermixing. It is compared with a reference sample, which consists of the substrate with a 20 nm vanadium and 20 nm TiNiSn buffer layer, 5 superlattice periods and an insulating layer. The insulating layer is identical across all samples of the sample series and consists of 200 nm of AlO_x and 100 nm SiO_2/MgO . As detailed in section 4.2 the temperature oscillations can be determined from the $V_{3\omega}$ -signal via

$$\hat{T} \approx \frac{2V_{3\omega}}{\alpha V_{\omega}} \quad (6.22)$$

with the 1ω -voltage component V_{ω} and the temperature coefficient α .

As shown in Figure 6.18a, both the superlattice and the reference sample have the same frequency characteristic. This $\propto \ln(2\omega)$ -dependence is dictated by the common substrate. However, a significant offset is apparent, which is caused by the added thermal resistance

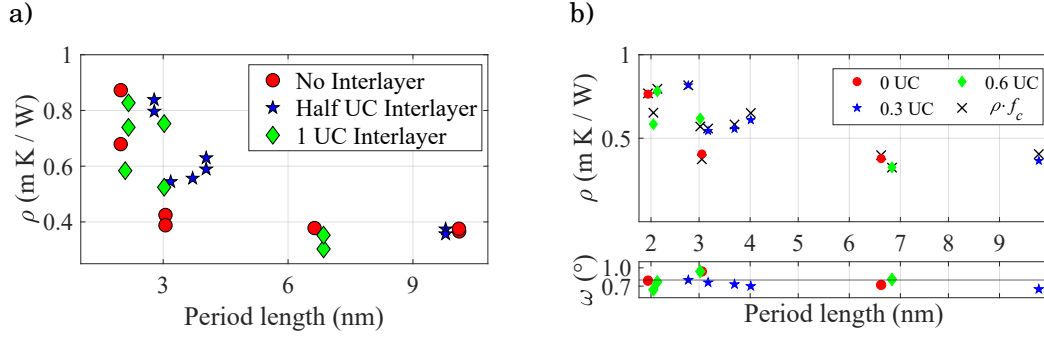


Figure 6.19: Thermal resistivities in dependence of the period length.

a) Thermal resistivities of the sample series. For every period two measurements exist that are performed to ensure reproducibility. Red dots correspond to pristine superlattices, blue stars to samples with 0.5 unit cells (UC) of intermixing and green diamonds are 1 UC intermixing samples.

b) Average thermal resistivities, where samples at the same period lengths are aggregated. The black crosses correspond to values corrected by crystalline quality with a correction factor $\alpha = 0.5$.

contributed by the superlattice. From this offset the thermal difference in temperature oscillations can be calculated with

$$\Delta T = \hat{T}_{SL} - \hat{T}_{Ref}, \quad (6.23)$$

which corresponds to the temperature difference caused by the additional thermal resistance of the superlattice relative to the reference sample. With the given heating power of 20 mW per $20 \cdot 10^{-9} \text{ m}^2$, the temperature difference caused by the superlattice amounts to $287.3 \pm 4 \text{ mK}$, as displayed in Figure 6.18b. The thermal resistivity then follows from the Fourier law via

$$\rho = \frac{1}{\kappa} = \frac{1}{j_Q} \nabla T = \frac{1}{P/A} \frac{\Delta T}{L}, \quad (6.24)$$

where κ is the thermal conductivity, A is the total area of the heater, P is the applied heating power, L is the superlattice thickness and j_Q is the heat flux per unit area.

6.5.2 Thermal Resistivity Measurements

In Figure 6.19a, the thermal resistivity of 22 samples of period lengths between 2 and 10 nm are shown. For every period length two independent measurements were performed to ensure reproducibility. For this purpose, identical samples were produced on a double-substrate holder, so they encounter identical sputter conditions.

6 Controlled Intermixing Superlattices

The sample series consists of samples with three distinct interface types, pristine superlattices, superlattices with 0.5 UC artificial intermixing and superlattices with 1 UC artificial intermixing. All interface types exhibit a strong increase in thermal resistivity towards small period lengths. While they have similar thermal resistivities for large period length, they differ significantly by interface type for period length below 6 nm. Here, the 0.5 UC intermixing superlattice increases strongest for small period length, the 1 UC superlattice second and the pristine superlattice shows the weakest increase.

Both, the overall increase in thermal resistivity and the differentiation at small period length, could be caused by a trivial change in growth behavior, in which the added intermixing acts as a buffer layer, promoting improved crystalline growth. As the thermal conductivity has a strong correlation with crystal quality in general and the rocking curve width specifically [145], this would lead to a lower thermal resistivity. In Figure 6.19b, the thermal resistivity data is multiplied with an empirical correction factor, which is given by

$$f_c = \left(\frac{\omega_0}{\omega} \right)^\alpha \quad (6.25)$$

where ω is the rocking curve width, ω_0 is the mean value across the sample series and α is an adjustable parameter. However, both the increase in thermal resistivity and the differentiation into the interface types towards smaller period lengths are robust against any choice of the exponent α . The rocking curve widths are relatively constant, have a low overall value and there is no apparent systematic trend across the sample series. Consequently, the thermal properties cannot merely be explained by a trivial dependence on growth behavior.

Rather it is more likely that with lower period length, the increasing number of interfaces start to dominate thermal properties overall. To extract the effect of the interfaces, the model introduced in section 6.2.1 is used to separate interface-related and bulk-like contributions

$$\rho = \rho_{bulk} + \rho_{intf} \quad (6.26)$$

$$= \rho_{bulk} \left(\frac{d + d_{equi}}{d} \right), \quad (6.27)$$

where ρ_{bulk} is the mean bulk resistivity of the constituent materials, d is the period length and d_{equi} is the effective interface material equivalent. The material equivalent gives the amount of additional material that corresponds to the thermal resistance supplied by the interfaces in a single superlattice period. It serves as the adjustable parameter in the fitting function, equation 6.27.

The sum of the bulk and interface thermal resistivity is displayed in Figure 6.20a, while it is separated into the two contributions in Figure 6.20b. For the largest period length the thermal resistivity almost completely corresponds to the mean of the bulk thermal resistivities. As the intermixing layer thickness is negligible relative to the total sample volume, this mean value is almost the same for all three interface types. At small period

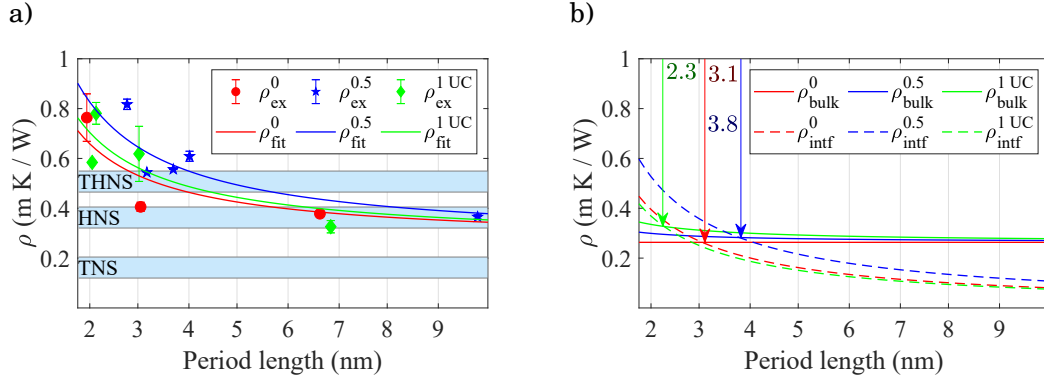


Figure 6.20: Thermal resistivity data together with a fit separating bulk-like and interface related contributions.

a) Thermal resistivity together with the fit. The error bars correspond to the deviation of two samples grown at the same period length.

b) The interface and bulk-like contribution to the thermal resistivity extracted by the fit. For each interface type the period length is marked, where both contributions are equal. This point corresponds to the interface material equivalent.

reused with permission, Heinz et al. [146].

length the 1 UC intermixing superlattices exhibit a significantly larger bulk-like contribution, as their $\text{Ti}_{0.5}\text{Hf}_{0.5}\text{NiSn}$ -content becomes comparable to the main components TiNiSn and HfNiSn . As the thermal resistivity of the mixed component is about two times larger than the mean of the main components, this leads to a larger expected bulk-like resistivity. This is why, although the 1 UC intermixing superlattice has a larger overall thermal resistivity increase towards smaller periods, the interface material equivalent is still $\sim 25\%$ smaller compared to the pristine superlattice. The half UC intermixing superlattice, however, has a larger interface contribution by $\sim 22\%$.

In Figure 6.21 the extracted thermal resistivities are compared to the value expected from the theoretical model explained in section 6.2.2. The reduction of interface defini-

Artificial intermixing layer thickness (unit cells)	Interface material equivalent d_{equi} (nm)	Effective thermal interface resistance ($\cdot 10^{-9} \text{Km}^2/\text{W}$)
0	3.0	0.81
0.5	3.8	1.08
1	2.3	0.75

Table 6.2: Material equivalents for different interface designs. The material equivalent expresses how much additional material corresponds to an individual interface in terms of thermal resistance.

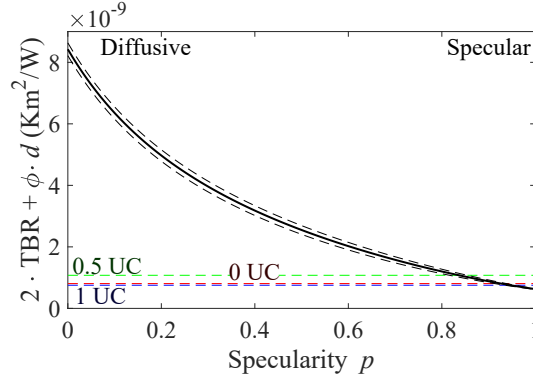


Figure 6.21: Model of the effective interface thermal resistivity in dependence of the specularity parameter p . It reflects the interface quality with the specular case $p = 1$ corresponding to perfectly flat atomar interfaces and $p = 0$ expressing heavily interface scattering dominated material boundaries. Additionally the experimental thermal resistance values are given for a pristine, a 0.5 UC and a 1 UC intermixing superlattice.

tion by the introduced intermixing layer is expected to increase thermal resistivity significantly. This should be especially pronounced in the TiNiSn/HfNiSn-systems, as the acoustic contrast is comparatively low. The thermal resistivity of the half UC-intermixing superlattice coincides with this observation, as it is significantly larger than the pristine superlattice. For further increased artificial intermixing, however, the model fails to explain the decrease in thermal resistivity.

A reason for the inaccuracy of model could be the assumption of the boundary layer as a 2-dimensional entity, the properties of which being fully described by the speularity parameter p . However, in the case of the 1 UC intermixing superlattice, the intermixing layer contributes up to 50% of the total sample volume for small period lengths. Yang et al. [85] suggest the finite extension of the interfacial region as an important aspect of thermal transport behavior. The boundary layer, being a mixture of the the main layer components, naturally exhibits intermediate acoustic properties. Therefore the lowered acoustic contrast promotes phonon transition, competing with the lowered interface specularity. As depicted in Figure 6.22, the result is a maximum in thermal boundary resistance for intermediate intermixing for most material combinations.

6.6 Summary

In this chapter the thermal resistivities of superlattices with different period lengths and interface types have been compared. The interfaces exhibit different amounts of intermixing, corresponding to pristine superlattices, 0.5 UC added intermixing and 1 UC artificial intermixing. The superlattices of all interface types show a dominance of interface-related thermal resistivity contributions towards smaller period length. This interface related contribution has been extracted and compared with estimations from an analyt-

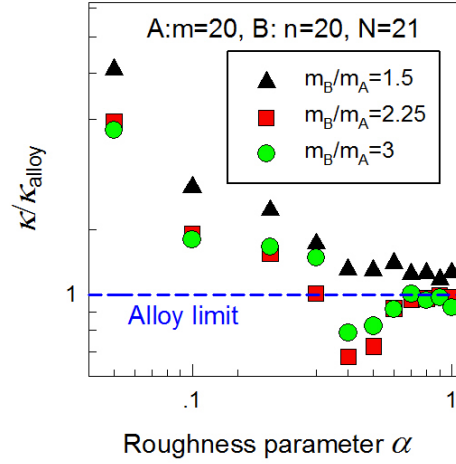


Figure 6.22: Phonon bridge effect in superlattices. Superlattices exhibit a characteristic minimum in thermal conductivity in dependence on their interface roughness parameter. The roughness parameter quantifies the effect of intermixing and the accompanying extension of the boundary layer. Reprinted figure with permission from Yang, Xiaolong; Li, Wu; Physical Review Materials, 2, 015401 (2018) Copyright 2020 by the American Physical Society

ical model developed by Alvarez et al [83]. This model combines the acoustic mismatch model (AMM) and diffusive mismatch model (DMM) to supply a description of superlattice, which can be adapted to the relevant interface quality. It shows that smooth interfaces in the TiNiSn/HfNiSn constitute relatively inefficient thermal barriers compared to other model systems like SiGe and AlAs/GaAs. Inversely, it demonstrates that these superlattices can profit particularly from added interface intermixing.

However, the comparison with the experiment reveals a competing effect of a decrease in local acoustic contrast by intermixing. The experimental thermal resistivity confirms the prediction of Yang et al. [85], which suggest an intermediate material boundary intermixing to optimize thermal resistivity. In accordance with their results, the study finds that an added intermixing of 0.5 UC increases the thermal resistivity relative to both the pristine superlattice and superlattices with more intermixing. Additionally it becomes clear, that interface-related and bulk-like contributions become comparable at length scales between 2-4 nm. The study shows that in the optimization of interfaces at the relevant device sizes, both the impact of interface specularly and the modification of local acoustic contrast by intermixing have to be considered.

Conclusion

With the availability of increasingly efficient thermoelectric material systems, wafer-based, low scale thermoelectric generators become progressively more interesting. This idea has been explored as on-chip solutions on the basis of different compounds, enabling autonomous sensors, heat radiation sensing and active point cooling. The choice of half-Heusler compounds as a material system presents itself due to their well-established, favorable thermoelectric properties and inherent adaptability. Half-Heusler compounds are materials with a XYZ molecular formula, where the X and Y-positions can be filled with a variety of transition metals, while Z is typically given by a p-block element. Because of the multitude of possible combinations and substitutions, a wide range of material properties can be engineered. Among common half-Heusler compounds are metals, topological insulators, Weyl-semimetals and ferromagnetic materials. For thermoelectric research, a sub-group is particularly interesting, which is formed by especially stable semiconductor-like compounds. Most notably, (Ti,Zr,Hf)NiSn compounds stand out with a thermoelectric conversion efficiency close to commercially available materials, with a technically interesting operative window of 500 °C- 900 °C. Consequently, (Ti,Zr,Hf)NiSn has been thoroughly researched and adapted to viable bulk and thin film-based systems.

As complementary research, (Ti,Zr,Hf)CoSb_{1-x}Sn_x-based materials have been explored as a p-type counterpart with comparable efficiencies. Compatible p- and n-type materials make the transition from a one- to an advantageous two-legged device design possible.

The resulting thin film generators present unique routes for the further optimization of thermoelectric properties. These routes rely on the precise control of the nano-structure that is inherent to thin film deposition processes. Specifically the fabrication of periodic layer arrangements using the superlattice approach provides an opportunity to manipulate thermoelectric properties. The additional internal boundaries of the layer structure act as thermal barriers that enable thermal transport engineering by adapting the parameters of the deposition process and the layer sequence. Here, the material boundary morphology represents a crucial aspect with profound relevance for thermoelectrics research specifically and nano-scale thermal transport in general.

This study explores the feasibility of thin film thermoelectric generators based on magnetron sputter deposited half-Heusler materials. It investigates two main aspects:

- A. The adaptation in thin film form of high conversion efficiency p-type (Hf,Zr)CoSb_{1-x}Sn_x to complement the established n-type (Ti,Zr,Hf)NiSn.
- B. The refinement of the superlattice approach by introducing an artificial intermixing layer to optimize the material as a thermal barrier.

A: P-type Thermoelectrics

As a candidate for a p-type thin film material, $\text{Hf}_{0.5}\text{Zr}_{0.5}\text{CoSb}_{1-x}\text{Sn}_x$ was chosen, because of the high demonstrated conversion efficiency and comparatively high intrinsic phase stability. The bulk material was compacted in a spark plasma sintering process to attain a suitable magnetron sputter target. This process is complicated by the melting points of Zr and Sn differing by roughly a factor of 8 and the high vapor pressure of Sb, leading to material loss. Consequently the process parameters had to be carefully controlled to yield a homogeneous, near-stoichiometric target. In the subsequent sputter deposition step from a single 5-component target, a similar degree of control is necessary for the fabrication of thin films. By adapting the sputter parameters, it is possible to navigate different growth regimes with distinct compositional and morphological properties. One of these regimes indicates the formation of nano-precipitates of acceptor-like Sn from the half Heusler matrix, potentially lowering the effective doping level. This morphological change was accompanied by a characteristic transition from a positive to a negative Seebeck coefficient, compatible with the assumptions of reduced doping.

To investigate this growth regime and to compare it with others, a range of thin film samples with distinct properties has been compared with two corresponding bulk samples. The resistivity shows an uptake of hopping-like conduction at low temperatures, which is dominant in thin films and only weakly expressed in bulk. Similarly, a bipolar behavior in the Hall-constant was observed for thin films, which was less pronounced in the bulk samples. For the thin films it was accompanied with a characteristic sign change in the Hall constant at intermediate temperatures of 20- 50 K, which was only observed in one of the bulk samples at lower temperatures of 2- 4 K. Based on a literature review, two impurity types were found to most likely dictate this behavior and electronic transport in general. The Sn-on-Sb substitution, introduced by extrinsic doping, provides deep acceptor levels, while cobalt interstitials, acting as shallow donors, supply conduction electrons. Based on these two impurities, two mechanisms were discussed to explain both the resistivity and Hall-effect data. The first mechanism assumes thermally activated ionization of deep acceptor states as the driver of the n-to-p transition. This mechanism describes the sign change in the Hall constant and the high temperature resistivity well. However, in the low temperature regime, where hopping-like behavior was observed, it deviates significantly from the experimental data. Consequently, a second mechanism was explored, in which electronic transport is carried within an impurity band formed by deep acceptor states, with a constant electron background. Towards low temperatures, the holes localize in the impurity band, leading to the electron background to become dominant and the Hall constant to change sign. This viewpoint explains both the Hall constant data and the resistivity over the whole temperature range reasonably well.

Overall the electrical transport properties give insight into $(\text{Hf,Zr})\text{CoSb}_{1-x}\text{Sn}_x$ as a whole. Both bulk and thin films samples have been identified as a fundamentally bipolar systems, where both electrons and holes determine electronic properties in concert. This is especially relevant for thermoelectrics, as p-type and n-type contributions to the Seebeck coefficient partially cancel each other out. Therefore, suppressing one mechanism can be an effective way of increasing the Seebeck coefficient and therefore optimizing conversion

efficiency. Additionally, the study demonstrates the relevance of hopping mechanisms and the role of the impurity band in the evolution of electronic properties.

B: Controlled Intermixing Superlattices

After significant thermal resistance increase could be demonstrated for TiNiSn/HfNiSn superlattices in previous work, this study explores the impact of interface quality in the same system. For this purpose, artificial intermixing layers are inserted at the material boundaries in the form of 50-50 mixtures of the main components. By varying the interlayer thickness, different interface types were prepared: Pristine TiNiSn/HfNiSn interfaces, 0.5 unit cell (UC) artificial intermixing and 1 UC artificial intermixing interfaces. The realized layer sequence was verified via X-ray diffraction, which was augmented with transmission electron microscopy to perform a full boundary layer characterization. The resulting structures were analyzed with respect to their thermal resistance with the 3ω -method in dependence of both period length and degree of intermixing. To interpret the resulting data, an analytical model of thermal transport in superlattices was adapted to TiNiSn/HfNiSn. It yields a particularly low efficacy of smooth interfaces as thermal barriers, which is a consequence of the comparatively low acoustic contrast. However, the model also finds that increasing intermixing has an especially large impact on optimizing the thermal resistance in this system. The experimental data of superlattices with moderate intermixing supports this view: Here the thermal resistance is increased by 22% compared to pristine superlattices. However, this model fails to explain superlattices with stronger intermixing for which the thermal resistance is decreased. In this case, a simulation of Yang et al. in generic superlattices gives further insight, which additionally takes the finite extent of the interfacial area into account. In agreement with our results, this study finds a maximum in the thermal resistance of superlattices for an intermediate degree of intermixing for most material combinations. The reason for the decrease of thermal resistance for strong intermixing is the function of the intermixing layer as an acoustic buffer. For short period length, the intermixing layer reaches up to 50% of the total sample volume in the investigated samples. As this intermixing layer naturally exhibits mediating acoustic properties between TiNiSn and HfNiSn it promotes phonon transmission. Therefore the two discussed effects compete with each other: The material boundary deterioration increases interface scattering, while the intermixing reduces the acoustic contrast locally. Both mechanisms in concert lead to an intermediate degree of intermixing that maximizes thermal resistance. This is especially relevant for layer structures with characteristic lengths of 2-4 nm, where interface and inner-layer effects contribute equally. Here, the interface part varies by more than 50% depending on interface quality.

Bibliography

- [1] IPCC, M. Allen, M. Babiker, Y. Chen, H. de Coninck, S. Connors, R. van Diemen, O. Dube, K. Ebi, F. Engelbrecht, M. Ferrat, J. Ford, P. Forster, S. Fuss, T. Guillén Bolaños, J. Harold, O. Hoegh-Guldberg, J.-C. Hourcade, D. Huppmann, and K. Zickfeld, *Summary for Policymakers. In: Global warming of 1.5°C. An IPCC Special Report*. 2018.
- [2] A. Shakouri, “Recent Developments in Semiconductor Thermoelectric Physics and Materials,” *Annu. Rev. Mater. Res.*, vol. 41, no. 1, pp. 399–431, 2011.
- [3] H. Ibach and H. Lüth, *Festkörperphysik*. Springer Berlin Heidelberg, 2009.
- [4] ASM, *ASM handbook Volume 2 - Properties and selection: Nonferrous alloys and special-purpose materials*, vol. 2. ASM International, 1993.
- [5] C. B. Vining, “An inconvenient truth about thermoelectrics,” *Nat. Mater.*, vol. 8, no. 2, pp. 83–85, 2009.
- [6] X. Zheng, C. Liu, Y. Yan, and Q. Wang, “A review of thermoelectrics research – Recent developments and potentials for sustainable and renewable energy applications,” *Renew. Sustain. Energy Rev.*, vol. 32, pp. 486–503, apr 2014.
- [7] S. Hunklinger, *Festkörperphysik*. De Gruyter Oldenbourg, 2009.
- [8] G. Pennelli, “Review of nanostructured devices for thermoelectric applications,” *Beilstein J. Nanotechnol.*, vol. 5, pp. 1268–1284, aug 2014.
- [9] S. LeBlanc, S. K. Yee, M. L. Scullin, C. Dames, and K. E. Goodson, “Material and manufacturing cost considerations for thermoelectrics,” *Renew. Sustain. Energy Rev.*, vol. 32, pp. 313–327, apr 2014.
- [10] L. Yang, Z. G. Chen, M. S. Dargusch, and J. Zou, “High Performance Thermoelectric Materials: Progress and Their Applications,” *Adv. Energy Mater.*, vol. 8, no. 6, pp. 1–28, 2018.
- [11] G. J. Snyder and E. S. Toberer, “Complex thermoelectric materials,” *Nat. Mater.*, vol. 7, pp. 105–114, feb 2008.
- [12] J. P. Heremans, B. Wiendlocha, and A. M. Chamoire, “Resonant levels in bulk thermoelectric semiconductors,” feb 2012.
- [13] C. Kittel, *Introduction to Solid State Physics, 8th edition*. Wiley, 1996.

- [14] T. M. Tritt, “Thermoelectric Phenomena, Materials, and Applications,” *Annu. Rev. Mater. Res.*, vol. 41, pp. 433–448, aug 2011.
- [15] J. Grandidier, J. B. Gilbert, and G. A. Carr, “Cassini Power Subsystem,” tech. rep., NASA/JPL, feb 2017.
- [16] K. B. Masood, P. Kumar, R. A. Singh, and J. Singh, “Odyssey of thermoelectric materials: foundation of the complex structure,” *J. Phys. Commun.*, vol. 2, p. 062001, jun 2018.
- [17] S. Chen and Z. Ren, “Recent progress of half-Heusler for moderate temperature thermoelectric applications,” *Mater. Today*, vol. 16, pp. 387–395, oct 2013.
- [18] L. Chen, S. Gao, X. Zeng, A. Mehdizadeh Dehkordi, T. M. Tritt, and S. J. Poon, “Uncovering high thermoelectric figure of merit in (Hf,Zr)NiSn half-Heusler alloys,” *Appl. Phys. Lett.*, vol. 107, p. 041902, jul 2015.
- [19] T. Graf, C. Felser, and S. S. Parkin, “Simple rules for the understanding of Heusler compounds,” *Prog. Solid State Chem.*, vol. 39, pp. 1–50, may 2011.
- [20] J. Toboła, L. Jodin, P. Pecheur, H. Scherrer, G. Venturini, B. Malaman, and S. Kaprzyk, “Composition-induced metal-semiconductor-metal crossover in half-Heusler Fe_{1-x}Ni_xTiSn,” *Phys. Rev. B - Condens. Matter Mater. Phys.*, vol. 64, pp. 1551031–1551037, oct 2001.
- [21] C. Shekhar, N. Kumar, V. Grinenko, S. Singh, R. Sarkar, H. Luetkens, S. C. Wu, Y. Zhang, A. C. Komarek, E. Kampert, Y. Skourski, J. Wosnitza, W. Schnelle, A. McCollam, U. Zeitler, J. Kübler, B. Yan, H. H. Klauss, S. S. Parkin, and C. Felser, “Anomalous Hall effect in Weyl semimetal half-Heusler compounds RPtBi (R = Gd and Nd),” *Proc. Natl. Acad. Sci. U. S. A.*, vol. 115, pp. 9140–9144, sep 2018.
- [22] T. Block, M. J. Carey, B. A. Gurney, and O. Jepsen, “Band-structure calculations of the half-metallic ferromagnetism and structural stability of full- and half-Heusler phases,” *Phys. Rev. B - Condens. Matter Mater. Phys.*, vol. 70, p. 205114, nov 2004.
- [23] D. T. Do, S. D. Mahanti, and J. J. Pulikkoti, “Electronic structure of Zr-Ni-Sn systems: Role of clustering and nanostructures in half-Heusler and Heusler limits,” *J. Phys. Condens. Matter*, vol. 26, no. 27, 2014.
- [24] J. Schmitt, Z. M. Gibbs, G. J. Snyder, and C. Felser, “Resolving the true band gap of ZrNiSn half-Heusler thermoelectric materials,” *Mater. Horizons*, vol. 2, no. 1, pp. 68–75, 2015.
- [25] F. G. Aliev, N. B. Brandt, V. V. Moshchalkov, V. V. Kozyrkov, R. V. Skolozdra, and A. I. Belogorokhov, “Gap at the Fermi level in the intermetallic vacancy system RBiSn(R=Ti,Zr,Hf),” *Zeitschrift für Phys. B Condens. Matter*, vol. 75, pp. 167–171, jun 1989.

- [26] V. V. Romaka, P. Rogl, L. Romaka, Y. Stadnyk, A. Grytsiv, O. Lakh, and V. Krayovskii, “Peculiarities of structural disorder in Zr- and Hf-containing Heusler and half-Heusler stannides,” *Intermetallics*, vol. 35, pp. 45–52, apr 2013.
- [27] P. Larson, S. D. Mahanti, and M. G. Kanatzidis, “Structural stability of Ni-containing half-Heusler compounds,” *Phys. Rev. B Condens. Matter*, vol. 62, pp. 12754–12762, nov 2000.
- [28] S. Ogut and K. M. Rabe, “Band gap and stability in the ternary intermetallic compounds NiSnM (M = Ti, Zr, Hf): A First-principles study,” *J. Appl. Phys.*, vol. 51, no. 16, 1995.
- [29] Y. G. Yu, X. Zhang, and A. Zunger, “Natural off-stoichiometry causes carrier doping in half-Heusler filled tetrahedral structures,” *Phys. Rev. B Condens. Matter*, vol. 95, no. 8, pp. 1–25, 2017.
- [30] H. Geng and H. Zhang, “Effects of phase separation on the thermoelectric properties of (Ti, Zr, Hf)NiSn half-Heusler alloys,” *J. Appl. Phys.*, vol. 116, no. 3, p. 33708, 2014.
- [31] W. Xie, A. Weidenkaff, X. Tang, Q. Zhang, J. Poon, and T. Tritt, “Recent Advances in Nanostructured Thermoelectric Half-Heusler Compounds,” *Nanomaterials*, vol. 2, no. 4, pp. 379–412, 2012.
- [32] M. Samanta, K. Pal, U. V. Waghmare, and K. Biswas, “Intrinsically Low Thermal Conductivity and High Carrier Mobility in Dual Topological Quantum Material, n-Type BiTe,” *Angew. Chemie*, vol. 132, pp. 4852–4859, mar 2020.
- [33] S. Sakurada and N. Shutoh, “Effect of Ti substitution on the thermoelectric properties of (Zr,Hf)NiSn half-Heusler compounds,” *Appl. Phys. Lett.*, vol. 86, no. 8, pp. 1–3, 2005.
- [34] S. Bhattacharya, T. M. Tritt, Y. Xia, V. Ponnambalam, S. J. Poon, and N. Thadhani, “Grain structure effects on the lattice thermal conductivity of Ti-based half-Heusler alloys,” *Appl. Phys. Lett.*, vol. 81, pp. 43–45, jul 2002.
- [35] E. Rausch, B. Balke, S. Ouardi, and C. Felser, “Enhanced thermoelectric performance in the p-type half-Heusler (Ti/Zr/Hf)CoSb_{0.8}Sn_{0.2} system via phase separation,” *Phys. Chem. Chem. Phys.*, vol. 16, no. 46, pp. 25258–25262, 2014.
- [36] R. Gross and A. Marx, *Festkörperphysik*. Berlin, Boston: De Gruyter Oldenbourg, 2014.
- [37] D. D. Royer and E. Dieulesaint, *Elastic waves in solids*. Springer, 2000.
- [38] C. V. Raman, “A New Radiation,” *Indian J. Phys.*, vol. 2, pp. 387–398, 1929.
- [39] S. N. Eliassen, A. Katre, G. K. Madsen, C. Persson, O. M. Løvvik, and K. Berland, “Lattice thermal conductivity of Ti_xZr_yHf_{1-x-y}NiSn half-Heusler alloys calculated

- from first principles: Key role of nature of phonon modes,” *Phys. Rev. B*, vol. 95, no. 4, pp. 1–9, 2017.
- [40] G. Ding, G. Y. Gao, and K. L. Yao, “Examining the thermal conductivity of the half-Heusler alloy TiNiSn by first-principles calculations,” *J. Phys. D: Appl. Phys.*, vol. 48, no. 23, pp. 22–26, 2015.
 - [41] J. Yang, “Theory of Thermal Conductivity,” in *Therm. Conduct.*, pp. 1–20, Springer US, oct 2006.
 - [42] C. Matthiessen, Augustus; Vogt, “IV. On the influence of temperature on the electric conducting-power of alloys,” *Philos. Trans. R. Soc. London*, vol. 154, pp. 167–200, dec 1864.
 - [43] J. Yang, D. T. Morelli, G. P. Meisner, W. Chen, J. S. Dyck, and C. Uher, “Influence of electron-phonon interaction on the lattice thermal conductivity of (formula presented),” *Phys. Rev. B - Condens. Matter Mater. Phys.*, vol. 65, pp. 1–5, feb 2002.
 - [44] D. M. Rowe, *Thermoelectrics handbook: macro to nano*. Taylor and Francis Group, 2005.
 - [45] R. Feynman, R. Leighton, M. Sands, and S. Treiman, *The Feynman lectures on physics - Mainly Electromagnetism and Matter*. Basic Books, 1964.
 - [46] M. Maldovan, “Narrow low-frequency spectrum and heat management by thermocrystals,” *Phys. Rev. Lett.*, vol. 110, no. 2, 2013.
 - [47] D. T. Morelli and G. P. Meisner, “Transport properties of pure and doped mnisn (m=Zr, Hf),” *Phys. Rev. B Condens. Matter*, vol. 59, no. 13, pp. 8615–8621, 1999.
 - [48] X. Su, P. Wei, H. Li, W. Liu, Y. Yan, P. Li, C. Su, C. Xie, W. Zhao, P. Zhai, Q. Zhang, X. Tang, and C. Uher, “Multi-Scale Microstructural Thermoelectric Materials: Transport Behavior, Non-Equilibrium Preparation, and Applications,” *Adv. Mater.*, vol. 29, no. 20, pp. 1–13, 2017.
 - [49] A. A. Balandin, “Thermal properties of graphene and nanostructured carbon materials,” jul 2011.
 - [50] M. Asheghi, Y. K. Leung, S. S. Wong, and K. E. Goodson, “Phonon-boundary scattering in thin silicon layers,” *Appl. Phys. Lett.*, vol. 71, pp. 1798–1800, sep 1997.
 - [51] O. Caballero-Calero and M. Martín-González, “Thermoelectric nanowires: A brief prospective,” *Scr. Mater.*, vol. 111, no. April, pp. 54–57, 2016.
 - [52] E. K. Lee, L. Yin, Y. Lee, J. W. Lee, S. J. Lee, J. Lee, S. N. Cha, D. Whang, G. S. Hwang, K. Hippalgaonkar, A. Majumdar, C. Yu, B. L. Choi, J. M. Kim, and K. Kim, “Large thermoelectric figure-of-merits from SiGe nanowires by simultaneously measuring electrical and thermal transport properties,” *Nano Lett.*, vol. 12, pp. 2918–2923, jun 2012.

- [53] Z. Wang and N. Mingo, "Diameter dependence of SiGe nanowire thermal conductivity," *Appl. Phys. Lett.*, vol. 97, p. 101903, sep 2010.
- [54] M. Thesberg, H. Kosina, and N. Neophytou, "On the effectiveness of the thermoelectric energy filtering mechanism in low-dimensional superlattices and nanocomposites," *J. Appl. Phys.*, vol. 120, no. 23, pp. 1–27, 2016.
- [55] H. Geng and H. Zhang, "Effects of phase separation on the thermoelectric properties of (Ti, Zr, Hf)NiSn half-Heusler alloys," *J. Appl. Phys.*, vol. 116, p. 033708, jul 2014.
- [56] P. Priyadarshi, A. Sharma, S. Mukherjee, and B. Muralidharan, "Superlattice design for optimal thermoelectric generator performance," *J. Phys. D: Appl. Phys.*, 2018.
- [57] H. Böttner and G. Chen, "Aspects of Thin-Film Superlattice Thermoelectric Devices, and Applications," *Mater. Sci. Eng. R Reports*, vol. 31, no. March, pp. 211–217, 2006.
- [58] C. Dames and G. Chen, "Theoretical phonon thermal conductivity of Si/Ge superlattice nanowires," *J. Appl. Phys.*, vol. 95, no. 2, pp. 682–693, 2004.
- [59] M. Maldovan, "Phonon wave interference and thermal bandgap materials," *Nat. Mater.*, vol. 14, no. 7, pp. 667–674, 2015.
- [60] M. Trigo, A. Fainstein, B. Jusserand, and V. Thierry-Mieg, "Finite-size effects on acoustic phonons in GaAs/AlAs superlattices," *Phys. Rev. B Condens. Matter*, vol. 66, pp. 1253111–1253117, sep 2002.
- [61] A. Giri, J. P. Niemelä, C. J. Szwejkowski, M. Karppinen, and P. E. Hopkins, "Reduction in thermal conductivity and tunable heat capacity of inorganic/organic hybrid superlattices," *Phys. Rev. B Condens. Matter*, vol. 93, no. 2, pp. 1–7, 2016.
- [62] S. T. Huxtable, A. R. Abramson, C. L. Tien, A. Majumdar, C. Labounty, X. Fan, G. Zeng, J. E. Bowers, A. Shakouri, and E. T. Croke, "Thermal conductivity of Si/SiGe and SiGe/SiGe superlattices," *Appl. Phys. Lett.*, vol. 80, no. 10, pp. 1737–1739, 2002.
- [63] B. Yang, J. Liu, K. Wang, and G. Chen, "Characterization of Cross-Plane Thermoelectric Properties of Si/Ge Superlattices," *Proc. ICT2001. 20 Int. Conf. Thermoelectr. (Cat. No.01TH8589)*, pp. 344–347, 2001.
- [64] M. N. Luckyanova, J. Garg, K. Esfarjani, A. Jandl, M. T. Bulsara, A. J. Schmidt, A. J. Minnich, S. Chen, M. S. Dresselhaus, Z. Ren, E. A. Fitzgerald, and G. Chen, "Coherent phonon heat conduction in superlattices," *Science (80-.)*, vol. 338, pp. 936–939, nov 2012.
- [65] M. N. Luckyanova, J. Mendoza, H. Lu, B. Song, S. Huang, J. Zhou, M. Li, Y. Dong, H. Zhou, J. Garlow, L. Wu, B. J. Kirby, A. J. Grutter, A. A. Puretzky, Y. Zhu, M. S. Dresselhaus, A. Gossard, and G. Chen, "Phonon localization in heat conduction," *Sci. Adv.*, vol. 4, no. 12, 2018.

- [66] M. Maldovan, “Specular reflection leads to maximum reduction in cross-plane thermal conductivity,” *J. Appl. Phys.*, vol. 125, no. 22, 2019.
- [67] B. Latour, S. Volz, and Y. Chalopin, “Microscopic description of thermal-phonon coherence: From coherent transport to diffuse interface scattering in superlattices,” *Phys. Rev. B Condens. Matter*, vol. 90, no. 1, p. 014307, 2014.
- [68] M. V. Simkin and G. D. Mahan, “Minimum Thermal Conductivity of Superlattices,” *Phys. Rev. Lett.*, vol. 84, no. 5, pp. 927–930, 2000.
- [69] A. Bartels, T. Dekorsy, H. Kurz, and K. Köhler, “Coherent control of acoustic phonons in semiconductor superlattices,” *Appl. Phys. Lett.*, vol. 72, no. 22, pp. 2844–2846, 1998.
- [70] F. He, W. Wu, and Y. Wang, “Direct measurement of coherent thermal phonons in Bi₂Te₃/Sb₂Te₃ superlattice,” *Appl. Phys. A Mater. Sci. Process.*, vol. 122, no. 8, pp. 1–5, 2016.
- [71] G. Chen, “Thermal Conductivity and Ballistic Phonon Transport in Cross-Plane Direction of Superlattices,” *Phys. Rev. B Condens. Matter*, vol. 57, no. 23, pp. 14958–14973, 1998.
- [72] R. Peierls, “Zur kinetischen Theorie der Wärmeleitung in Kristallen,” *Ann. Phys.*, vol. 395, pp. 1055–1101, jan 1929.
- [73] E. S. Landry and A. J. H. McGaughey, “Effect of interfacial species mixing on phonon transport in semiconductor superlattices,” *Phys. Rev. B Condens. Matter*, vol. 79, no. 7, pp. 29–34, 2009.
- [74] J. M. Ziman, *Electrons and phonons: the theory of transport phenomena in solids*. Clarendon Press, 2001.
- [75] E. T. Swartz and R. O. Pohl, “Thermal boundary resistance,” *Rev. Mod. Phys.*, vol. 61, no. 3, pp. 605–668, 1989.
- [76] A. Singha and B. Muralidharan, “Incoherent scattering can favorably influence energy filtering in nanostructured thermoelectrics,” *Sci. Rep.*, vol. 7, pp. 1–11, dec 2017.
- [77] T. S. English, J. C. Duda, J. L. Smoyer, D. A. Jordan, P. M. Norris, and L. V. Zhigilei, “Enhancing and tuning phonon transport at vibrationally mismatched solid-solid interfaces,” *Phys. Rev. B Condens. Matter*, vol. 85, no. 3, pp. 1–14, 2012.
- [78] M. Hu, X. Zhang, D. Poulikakos, and C. P. Grigoropoulos, “Large “near junction” thermal resistance reduction in electronics by interface nanoengineering,” *Int. J. Heat Mass Transf.*, vol. 54, pp. 5183–5191, dec 2011.
- [79] B. Yang and G. Chen, “Partially coherent phonon heat conduction in superlattices,” *Phys. Rev. B Condens. Matter*, vol. 67, no. 19, pp. 1–4, 2003.

- [80] R. E. Peterson and A. C. Anderson, “The Kapitza thermal boundary resistance,” *J. Low Temp. Phys.*, vol. 11, pp. 639–665, jun 1973.
- [81] C. Huygens, *Traité de la lumière : Où sont expliquées les causes de ce qui lui arrive dans la reflexion, et dans la refraction et particulièrement dans l'étrange réfraction du cristal d'Islande*. Chez Pierre vander Aa, marchand libraire, feb 1690.
- [82] D. G. Cahill, W. K. Ford, K. E. Goodson, G. D. Mahan, A. Majumdar, H. J. Maris, R. Merlin, and S. R. Phillpot, “Nanoscale thermal transport,” *J. Appl. Phys.*, vol. 93, no. 2, pp. 793–818, 2003.
- [83] F. X. Alvarez, J. Alvarez-Quintana, D. Jou, and J. R. Viejo, “Analytical expression for thermal conductivity of superlattices,” *J. Appl. Phys.*, vol. 107, no. 8, 2010.
- [84] B. Qiu, G. Chen, and Z. Tian, “Effects of Aperiodicity and Roughness on Coherent Heat Conduction in Superlattices,” *Nanoscale Microscale Thermophys. Eng.*, vol. 19, pp. 272–278, oct 2015.
- [85] X. Yang and W. Li, “Optimizing phonon scattering by tuning surface-interdiffusion-driven intermixing to break the random-alloy limit of thermal conductivity,” *Phys. Rev. Mater.*, vol. 2, no. 1, p. 015401, 2018.
- [86] P. Chakraborty, L. Cao, and Y. Wang, “Ultralow Lattice Thermal Conductivity of the Random Multilayer Structure with Lattice Imperfections,” *Sci. Rep.*, vol. 7, no. 1, pp. 1–8, 2017.
- [87] P. Drude, “Zur Elektronentheorie der Metalle,” *Ann. Phys.*, vol. 306, pp. 566–613, jan 1900.
- [88] A. M. James and M. P. Lord, *Macmillan's chemical and physical data*. London: Macmillan, 1992.
- [89] N. W. Ashcroft and N. D. Mermin, “Solid State Physics,” 1976.
- [90] A. Yildiz, N. Serin, T. Serin, and M. Kasap, “Crossover from nearest-neighbor hopping conduction to Efros-Shklovskii variable-range hopping conduction in hydrogenated amorphous silicon films,” *Jpn. J. Appl. Phys.*, vol. 48, no. 11, 2009.
- [91] N. F. Mott and E. A. Davis, *Electronic Processes in Non-Crystalline Materials*. Oxford Classic Texts in the Physical Sciences, OUP Oxford, 2012.
- [92] B. I. Shklovskii and A. L. Efros, *Electronic Properties of Doped Semiconductors*, vol. 45 of *Springer Series in Solid-State Sciences*. Berlin, Heidelberg: Springer Berlin Heidelberg, 1984.
- [93] S. Swann, “Magnetron sputtering,” *Phys. Technol.*, vol. 19, no. 2, pp. 67–75, 1988.
- [94] Y. V. Martynenko, A. V. Rogov, and V. I. Shul'ga, “Angular distribution of atoms during the magnetron sputtering of polycrystalline targets,” *Tech. Phys.*, vol. 57, pp. 439–444, apr 2012.

- [95] K. J. Lesker Company, "Practical Process Tips - Sputtering," *Lesker Tech*, vol. 7, pp. 1–4, 2010.
- [96] J. A. Thornton, "Influence of Apparatus Geometry and Deposition Conditions on the Structure and Topography of Thick Sputtered Coatings," *J. Vac. Sci. Technol.*, vol. 11, no. 4, pp. 666–670, 1974.
- [97] E. Alfonso, J. Olaya, and G. Cubillos, "Thin Film Growth Through Sputtering Technique and Its Applications," *Cryst. - Sci. Technol.*, 2012.
- [98] E. Kusano, "Structure-Zone Modeling of Sputter-Deposited Thin Films: A Brief Review," *Appl. Sci. Conver. Technol.*, vol. 28, no. 6, pp. 179–185, 2019.
- [99] P. Andersson and G. Bäckström, "Thermal conductivity of solids under pressure by the transient hot wire method," *Rev. Sci. Instrum.*, vol. 47, pp. 205–209, feb 1976.
- [100] D. G. Cahill, "Thermal conductivity measurement from 30 to 750 K: The 3ω method," *Rev. Sci. Instrum.*, vol. 61, no. 2, pp. 802–808, 1990.
- [101] D. G. Cahill, "Erratum: Thermal conductivity measurement from 30 to 750 K. The 3ω method (Review of Scientific Instruments (1990) 61 (802))," oct 2002.
- [102] T. Borca-Tasciuc, A. R. Kumar, and G. Chen, "Data reduction in 3ω method for thin-film thermal conductivity determination," *Rev. Sci. Instrum.*, vol. 72, no. 4, pp. 2139–2147, 2001.
- [103] Y. Y. S. Ju, K. Kurabayashi, and K. E. K. Goodson, "Thermal characterization of anisotropic thin dielectric films using harmonic Joule heating," *Thin Solid Films*, vol. 339, no. 1-2, pp. 160–164, 1999.
- [104] A. Jacquot, B. Lenoir, A. Dauscher, M. Stölzer, and J. Meusel, "Numerical simulation of the 3ω method for measuring the thermal conductivity," *J. Appl. Phys.*, vol. 91, pp. 4733–4738, apr 2002.
- [105] C. Dames, "Measuring the Thermal Conductivity of Thin Films: 3 Omega and Related Electrothermal Methods," *Annu. Rev. Heat Transf.*, vol. 16, no. 1, pp. 7–49, 2013.
- [106] H. S. Carslaw and J. C. Jaeger, *Conduction of Heat in Solids*. Oxford University Press, 1959.
- [107] M. Bogner, G. Benstetter, and Y. Q. Fu, "Cross- and in-plane thermal conductivity of AlN thin films measured using differential 3-omega method," *Surf. Coatings Technol.*, vol. 320, pp. 91–96, 2017.
- [108] J. M. Gregoire, M. B. Lobovsky, M. F. Heinz, F. J. Disalvo, and R. B. Van Dover, "Resputtering phenomena and determination of composition in codeposited films," *Phys. Rev. B - Condens. Matter Mater. Phys.*, vol. 76, p. 195437, nov 2007.

- [109] A. Bogaerts, J. Naylor, M. Hatcher, W. J. Jones, and R. Mason, “Influence of sticking coefficients on the behavior of sputtered atoms in an argon glow discharge: Modeling and comparison with experiment,” *J. Vac. Sci. Technol. A Vacuum, Surfaces, Film.*, vol. 16, pp. 2400–2410, jul 1998.
- [110] M. N. Guzik, C. Echevarria-Bonet, M. D. Riktor, P. A. Carvalho, A. E. Gunnæs, M. H. Sørby, and B. C. Hauback, “Half-Heusler phase formation and Ni atom distribution in M-Ni-Sn (M = Hf, Ti, Zr) systems,” *Acta Mater.*, vol. 148, pp. 216–224, 2018.
- [111] W. H. Bragg and W. L. Bragg, “The reflection of X-rays by crystals,” *Proc. R. Soc. London. Ser. A, Contain. Pap. a Math. Phys. Character*, vol. 88, pp. 428–438, jul 1913.
- [112] P. Scherrer, “Bestimmung der Größe und der inneren Struktur von Kolloidteilchen mittels Röntgenstrahlen,” *Nachrichten von der Gesellschaft der Wissenschaften zu Göttingen, Math. Klasse*, vol. 1918, pp. 98–100, 1918.
- [113] A. L. Patterson, “The scherrer formula for X-ray particle size determination,” *Phys. Rev.*, vol. 56, no. 10, pp. 978–982, 1939.
- [114] Y. Chen, D. M. Bagnall, H. J. Koh, K. T. Park, K. Hiraga, Z. Zhu, and T. Yao, “Plasma assisted molecular beam epitaxy of ZnO on c-plane sapphire: Growth and characterization,” *J. Appl. Phys.*, vol. 84, pp. 3912–3918, oct 1998.
- [115] E. E. Fullerton, I. K. Schuller, H. Vanderstraeten, and Y. Bruynseraede, “Structural refinement of superlattices from x-ray diffraction,” *Phys. Rev. B Condens. Matter*, vol. 45, no. 16, pp. 9292–9310, 1992.
- [116] T. Jaeger, C. Mix, M. Schwall, X. Kozina, J. Barth, B. Balke, M. Finsterbusch, Y. U. Idzerda, C. Felser, and G. Jakob, “Epitaxial growth and thermoelectric properties of TiNiSn and Zr_{0.5}Hf_{0.5}NiSn thin films,” *Thin Solid Films*, vol. 520, pp. 1010–1014, nov 2011.
- [117] S. Sakurada and N. Shutoh, “Effect of Ti substitution on the thermoelectric properties of (Zr,Hf)NiSn half-Heusler compounds,” *Appl. Phys. Lett.*, vol. 86, p. 082105, feb 2005.
- [118] S. R. Culp, J. W. Simonson, S. J. Poon, V. Ponnambalam, J. Edwards, and T. M. Tritt, “(Zr,Hf)Co(Sb,Sn) half-Heusler phases as high-temperature (>700 °C) p-type thermoelectric materials,” *Appl. Phys. Lett.*, vol. 93, no. 2, pp. 0–3, 2008.
- [119] E. Rausch, B. Balke, J. M. Stahlhofen, S. Ouardi, U. Burkhardt, and C. Felser, “Fine tuning of thermoelectric performance in phase-separated half-Heusler compounds,” *J. Mater. Chem. C*, vol. 3, no. 40, pp. 10409–10414, 2015.
- [120] J. P. Makongo, D. K. Misra, X. Zhou, A. Pant, M. R. Shabetai, X. Su, C. Uher, K. L. Stokes, and P. F. Poudeu, “Simultaneous large enhancements in thermopower and electrical conductivity of bulk nanostructured half-Heusler alloys,” *J. Am. Chem. Soc.*, vol. 133, no. 46, pp. 18843–18852, 2011.

- [121] L. Huang, Q. Zhang, B. Yuan, X. Lai, X. Yan, and Z. Ren, “Recent progress in half-Heusler thermoelectric materials,” *Mater. Res. Bull.*, vol. 76, pp. 107–112, apr 2016.
- [122] E. Rausch, *Thermoelectric performance of p -type TiCoSb half-Heusler compounds – Intrinsic phase separation and charge carrier concentration optimization as key to high efficiency*. PhD thesis, Johannes Gutenberg-University Mainz, 2015.
- [123] D. P, “CRC Handbook of Chemistry and Physics,” *J. Mol. Struct.*, vol. 268, p. 320, apr 1992.
- [124] T. Jaeger, *Thermoelectric properties of TiNiSn and Zr 0.5 Hf 0.5 NiSn thin films and superlattices with reduced thermal conductivities*. PhD thesis, Johannes Gutenberg University Mainz, 2013.
- [125] G. H. Fecher, E. Rausch, B. Balke, A. Weidenkaff, and C. Felser, “Half-Heusler materials as model systems for phase-separated thermoelectrics,” *Phys. Status Solidi Appl. Mater. Sci.*, vol. 213, no. 3, pp. 716–731, 2016.
- [126] T. Sekimoto, K. Kurosaki, H. Muta, and S. Yamanaka, “Thermoelectric and Thermophysical Properties of TiCoSb-ZrCoSb-HfCoSb Pseudo Ternary System Prepared by Spark Plasma Sintering,” *Mater. Trans.*, vol. 47, no. 6, pp. 1445–1448, 2006.
- [127] F. Aliev, N. Brandt, V. Kozyr’kov, V. Moshchalkov, R. Skolozdra, Y. Stadnyk, and V. Pecharski, “Metal-insulator transition of RNiSn (R = Zr, Hf, Ti) intermetallic vacancy systems,” *Sov. J. Exp. Theor. Phys. Lett.*, vol. 45, p. 684, 1987.
- [128] V. Romaka, P. Rogl, L. Romaka, Y. Stadnyk, A. Grytsiv, O. Lakh, and V. Krayovskii, “Peculiarities of structural disorder in Zr- and Hf-containing Heusler and half-Heusler stannides,” *Intermetallics*, vol. 35, pp. 45–52, apr 2013.
- [129] J.-H. Bahk and A. Shakouri, “Minority carrier blocking to enhance the thermoelectric figure of merit in narrow-band-gap semiconductors,” *Phys. Rev. B Condens. Matter*, vol. 93, p. 165209, apr 2016.
- [130] L. H. Liang and B. Li, “Size-dependent thermal conductivity of nanoscale semiconducting systems,” *Phys. Rev. B - Condens. Matter Mater. Phys.*, vol. 73, no. 15, pp. 1–4, 2006.
- [131] G. Lebon, “Heat conduction at micro and nanoscales: A review through the prism of Extended Irreversible Thermodynamics,” *J. Non-Equilibrium Thermodyn.*, vol. 39, no. 1, pp. 35–59, 2014.
- [132] F. X. Alvarez and D. Jou, “Memory and nonlocal effects in heat transport: From diffusive to ballistic regimes,” *Appl. Phys. Lett.*, vol. 90, no. 8, pp. 2005–2008, 2007.
- [133] G. Fiedler, *Thermoelektrische Eigenschaften von nanostrukturierten Halbleitern: Si/Ge-Quantenpunktkristalle und ZrCoBi/ZrNiSn Halb-Heusler Schichtstrukturen*. PhD thesis, University Duisburg-Essen, nov 2015.

- [134] A. A. Musari, B. I. Adetunji, P. O. Adebambo, and G. A. Adebayo, "Lattice dynamics and thermodynamic investigation of MNiSn (M= Hf, Ti and Zr) Half-Heusler compounds: Density functional theory approach," *Mater. Today Commun.*, vol. 22, p. 100671, mar 2020.
- [135] F. X. Alvarez and D. Jou, "Size and frequency dependence of effective thermal conductivity in nanosystems," *J. Appl. Phys.*, vol. 103, p. 094321, may 2008.
- [136] S. A. Barczak, J. Buckman, R. I. Smith, A. R. Baker, E. Don, I. Forbes, and J. W. G. Bos, "Impact of interstitial Ni on the thermoelectric properties of the half-Heusler TiNiSn," *Materials (Basel)*, vol. 11, no. 4, pp. 1–13, 2018.
- [137] J. Callaway, "Model for lattice thermal conductivity at low temperatures," *Phys. Rev.*, vol. 113, pp. 1046–1051, feb 1959.
- [138] P. Holuj, C. Euler, B. Balke, U. Kolb, G. Fiedler, M. M. Müller, T. Jaeger, E. Chávez Angel, P. Kratzer, and G. Jakob, "Reduced thermal conductivity of TiNiSn/HfNiSn superlattices," *Phys. Rev. B Condens. Matter*, vol. 92, no. 12, pp. 1–5, 2015.
- [139] Y. Ikumura, Y. Sugawara, I. Tanaka, and P. Pirouz, "Atomic and Electronic Structure of V/MgO Interface," *Interface Sci.*, vol. 5, no. 1, pp. 5–16, 1997.
- [140] R. Pretorius, J. M. Harris, and M. A. Nicolet, "Reaction of thin metal films with SiO₂ substrates," *Solid State Electron.*, vol. 21, pp. 667–675, apr 1978.
- [141] P. Komar and G. Jakob, "CADEM: Calculate X-ray diffraction of epitaxial multilayers," *J. Appl. Crystallogr.*, vol. 50, no. 1, pp. 288–292, 2017.
- [142] P. Komar, *Nanostructured half-Heusler superlattices as a model system for thermoelectrics*. PhD thesis, Johannes Gutenberg University Maint, 2017.
- [143] M. Wang, H. S. Liu, G. M. Cai, and Z. P. Jin, "Measurement of phase equilibria in Ti-Ni-Sn system," *Trans. Nonferrous Met. Soc. China (English Ed.)*, vol. 28, no. 4, pp. 819–828, 2018.
- [144] A. Lis, C. Kenel, and C. Leinenbach, "Characteristics of Reactive Ni₃Sn₄ Formation and Growth in Ni-Sn Interlayer Systems," *Metall. Mater. Trans. A*, vol. 47, pp. 2596–2608, jun 2016.
- [145] T. Jaeger, P. Holuj, C. Mix, C. Euler, M. H. Aguirre, S. Populoh, A. Weidenkaff, and G. Jakob, "Thermal conductivity of half-Heusler superlattices," *Semicond. Sci. Technol.*, vol. 29, no. 12, pp. 1–6, 2014.
- [146] S. Heinz, E. C. Angel, M. Trapp, H.-J. Kleebe, and G. Jakob, "Phonon Bridge Effect in Superlattices of Thermoelectric TiNiSn/HfNiSn With Controlled Interface Intermixing," *Nanomaterials*, vol. 10, p. 1239, jun 2020.

List of (co-)authored Publications

- 1) **Heinz, Sven**, Emigdio Chavez Angel, Maximilian Trapp, Hans-Joachim Kleebe, and Gerhard Jakob. 2020.
“Phonon Bridge Effect in Superlattices of Thermoelectric TiNiSn/HfNiSn With Controlled Interface Intermixing.”
Nanomaterials 10 (6): 1239.
- 2) **Heinz, Sven**, Benjamin Balke, and Gerhard Jakob. 2019.
“Hole Localization in Thermoelectric Half-Heusler (Zr_{0.5}Hf_{0.5})Co(Sb_{1-x}Sn_x) Thin Films.”
Thin Solid Films 692 (December): 137581.
- 3) Becker, Sven, **Sven Heinz**, Mehran Vafaei, Mathias Kläui, and Gerhard Jakob. 2020.
“The Challenge in Realizing an Exchange Coupled BiFeO₃-Double Perovskite Bilayer.” *Journal of Magnetism and Magnetic Materials* 506 (July): 166766.
- 4) Chavez-Angel, E., N. Reuter, P. Komar, **S. Heinz**, U. Kolb, H. J. Kleebe, and G. Jakob. 2019.
“Subamorphous Thermal Conductivity of Crystalline Half-Heusler Superlattices.”
Nanoscale and Microscale Thermophysical Engineering 23 (1): 1-9.

Curriculum Vitae

Sven Heinz

Date of birth: 01.04.1989

Place of birth: Simmern (Hunsrück)

Oct. 2016 - current

PhD-studies

Institute of Physics

Johannes Gutenberg-University Mainz

Jun. 2015 - Aug. 2016

Work and Travel

Sep. 2012 - May 2015

Master of Science, Physics

Institute of Physics

Johann Wolfgang Goethe-University Frankfurt

Apr. 2009 - Aug. 2012

Bachelor of Science, Physics

Institute of Physics

Johann Wolfgang Goethe-University Frankfurt

Apr. 2009 - Aug. 2012

Compulsory civilian service

Paritätisches Seniorenheim Beltheim

Aug. 1999 - Mar. 2008

Abitur

Integrierte Gesamtschule Kastellaun

Acknowledgements

Dear esteemed colleagues,

I feel very fortunate to have been part of this group. I work best when I enjoy what I am doing and you have been a significant reason why I enjoyed the last few years. Especially in tough times, when my experiments did not go well, I was glad to have you around to lift my day up. This is why I feel that I owe a significant part of the results in this thesis to all your support, in small things and big. I learned to appreciate this even more during the last months of involuntary home-office.

I want to especially point something out which seems obvious. When you are new to a group and are trying to find your way, small signs of appreciation are meaningful. I was fortunate enough in my first, most difficult months, to have people around me, showing me this kind of appreciation.

I want to thank everyone, who started the traditions that I have come to love: The social thursdays (thanks XXXXX*), Oktoberfest (also XXXXX*), the bar crawls (thanks XXXXX*), Fast-nacht (thanks Mainz) and the Wagen tours (thanks to all the generations of PhD-students before us).

I thank Gerhard for being a Professor that is extraordinarily approachable by his students. His expertise and persistence solved many difficult problems, without which this thesis would not have been possible.

I also want to thank XXXXX* for providing a productive environment and framework.

Zu guter letzt. Vielen Dank an meine Familie.

Ich danke meinen Geschwistern dafür, dass sie mich früh geprägt haben: wer von klein an von positiven Personen umgeben ist, wächst auf als jemand, der das Gute in seinen Mitmenschen sieht und deswegen offen auf sie zugeht. Diese Prägung ist eine meiner wichtigsten Eigenschaften, eine entscheidende Voraussetzung für diese Arbeit und ein bedeutender Teil meines Lebens.

Meine Eltern haben viele Opfer erbracht, um mir Möglichkeiten zu geben, die sie selbst nie hatten. Ich erkenne an, dass das einerseits nicht selbstverständlich ist und andererseits die Grundlage für alles, was ich bisher erreichen konnte. Deswegen noch einmal ausdrücklich: Vielen Dank.

* Aus Datenschutzgründen entfernt.